

Chapter 1. Introduction

1.1 Background of microfluidics

Microfluidics has been developed over the last 30 years in parallel with the advancement of microelectromechanical systems (MEMS) technology. Many different devices are under development, ranging from single components such as flow sensors, to complex microfluid handling systems for chemical analysis, consisting of pumps, mixer valves, flow sensors, separation capillaries etc.

The field of microfluidics is expanding rapidly with emerging products such as biological and medical platforms and micro-cooling devices that rely on micropumps as the core of their function. Micropumps are utilized in many applications including biological, chemical, and sensor network systems. Small volumes of fluids in these microsystems are often pumped, mixed, controlled or otherwise manipulated during operation. For example, biological samples must be moved through the components of miniature assay systems and react with reagents or biomarkers for detection and identification [1,2].

In 2002, the microfluidics market was estimated at \$3-4.5 billion and is increasing 25-35% annually [3]. A new field of research and products called a micro total analysis system (μ TAS) is emerging that relies on micropumps for lab-on-chip devices [4]. There are several reasons that make microfluidic devices important.

- (1) Miniaturized components and processes use small volumes of fluids, thus leading to reduced consumption of reagents and samples. This decreases costs and permits small quantities of precious samples to be utilised. Quantities of waste products

are also reduced.

- (2) The small scale of microfluidic devices improves the efficiency and accuracy of biodetection. Reduced measurement times, improved sensitivity are also attainable.
- (3) Many microfluidic technologies permit the construction of devices containing multiple components with different functionalities. A single integrated chip could perform a series of biological or chemical processes from beginning to end, for example, fluid transportation, mixing, sensing and measurement. Performing all fluidic handling operations within a single chip also reduces risk of sample loss and cross-contamination.

However, microfluidic applications are currently in limited use due to lack of research and development, and the high cost of production [5]. The most important components of microfluidics are the micromixer and the micropumps. The types of micropumps vary widely in design and applications, but can be categorized into two main groups: mechanical and non-mechanical pumps. Mechanical micropumps usually represent smaller versions of macro-sized pumps and include reciprocating, diaphragm, piston, and rotary designs. Mechanical micropumps have limited applications due to their high cost and difficulty of fabrication and are not detailed in this review. Non-mechanical pumps are unique to microfluidics because unlike most macro-scale pumps they have no moving parts involved. Non-mechanical micropumps can also be divided into two categories: continuous flow micropumps and digital micropumps. Continuous flow pumps include electrohydrodynamic (EHD), electro-osmotic (EO) and magnetohydrodynamic (MHD) micropumps. The latter includes electrowetting or dielectric (EW), optical electrowetting and electrostatic micropumps mostly relying on the alteration of surface tension. Recently there has emerged a new type of moving-part-free micropump utilizing a surface acoustic wave (SAW) as an actuation force. The research detailed in the thesis is to develop SAW-based micropumps and micromixers for lab-on-a-chip application, and the in the

next section review will highlight the relevant technology development.

1.2 Piezoelectric interactions

Piezoelectric crystals play a dominant role in the communications and electronics industry, in which they are commonly used as filters, precision timers or for frequency control in oscillator circuits. Some materials, such as quartz, are naturally occurring piezoelectrics. Others, however, need to be polarized in order to make them piezoelectric. Polarization involves elevating the temperature while concomitantly applying an electric field across the sample, then cooling it down to room temperature with the electric field still applied [6]. The material then displays classical piezoelectric behavior.

Piezoelectricity is a coupling between a material's mechanical and electrical behaviour. The direct piezoelectric effect is present when a mechanical deformation of the piezoelectric material produces a change in the electric polarization of that material, with the change being proportional to the magnitude of the deformation. In other words, an electric charge appears on certain opposite faces of the piezoelectric material when it is mechanically loaded. The converse piezoelectric effect is the phenomenon whereby a mechanical stress that is proportional to an acting external electric field is induced in the piezoelectric material; the material is deformed when an electric voltage is applied [7, 8].

The piezoelectric effect can be demonstrated by applying either a compressive or tensile stress to the opposite faces of a piezoelectric crystal. Figure 3.2 shows that the resulting deformation of the crystal lattice produces a separation of the positive and negative charges.

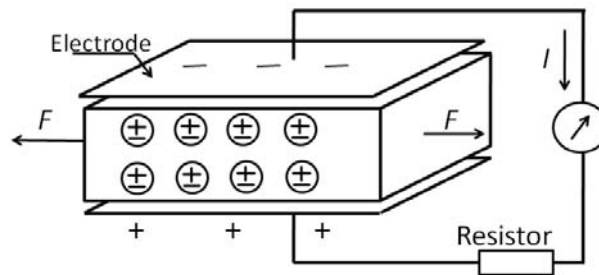


Figure 1.1 Transformation of mechanical energy into electrical energy

This effect results in electrical charge appearing on the surface of the electrodes. When the force is removed, the strain within the crystal lattice is released, causing charge to flow, thus re-establishing a zero potential difference between the electrodes. If a sinusoidal stress alternating between the tensile and compressive forces is applied to the opposite crystal faces, a sinusoidal piezoelectric voltage will appear across the electrodes. In this case, electrical energy is produced from mechanical energy. This process of crystal deformation can be reversed. When an external voltage is applied to the electrodes, the crystal lattice will deform by an amount proportional to the applied voltage. In this case, electrical energy is transformed into mechanical energy.

An ideal coupling mechanism between the electric circuit and the mechanical properties of the crystal ensures that the frequency of the mechanical acoustic wave is identical to the electric frequency. In other words, a distortion-free interface has extremely low dissipation.

1.3 Historical background of SAWs

Surface acoustic waves can be generated on the free surface of an elastic solid. This phenomenon has been exploited in electronic analog signal processing over the past 30 years, with the development of a host of devices and systems for consumer, commercial and military applications running at a multi-million-dollar annual rate. Although this is a comparatively new electronic technology, the scientific findings date back over the past 100 years. A mathematical discussion on the propagation of surface acoustic waves at the free surface of a homogeneous isotropic elastic solid

was first reported by Lord Rayleigh in an address to the London Mathematical Society on 12 November 1855 [9]. He also discovered the phenomenon now called Rayleigh scattering, and predicted the existence of the surface waves now known as Rayleigh waves. Lord Rayleigh reported the surface acoustic wave mode of propagation, and in his classic paper, he predicted the properties of these waves. Named after their discoverer, Rayleigh waves have a longitudinal and a transverse shear component that can couple with a medium in contact with the device's surface. The coupling strongly affects the amplitude and velocity of the waves, allowing SAW sensors to sense mass and mechanical properties directly.

SAWs are mechanical (acoustic) rather than electromagnetic wave. The SAW travels along the surface of a material having some elasticity, with an amplitude that typically decays exponentially with the depth of the substrate. Much of an earthquake's destructive force is carried by this type of wave. SAWs achieved little recognition for their application in RF until three decades ago. It was not until 1965 that the phenomenon of surface acoustic wave propagation was first exploited for its applications to electronic devices with the invention of the interdigital transducer (IDT) by White and Volymer at the University of California [10]. It is the most efficient technique for the generation and detection of surface acoustic waves on a piezoelectric surface. The advent of the IDT made analog electrical filters operate at selected frequencies in the range from 10 MHz to 1 GHz or above.

SAW devices are an important class of piezoelectric devices, providing frequency control, frequency selection, and signal processing capabilities as filters, oscillators and transformers [11, 12]. SAW filters have enjoyed successful applications in the booming cellular telephone market and provided significant advantages in performance, cost, and size over other filter technologies.

Merits of SAW devices

SAW-based devices and systems have several excellent features. These include:

- (1) With superimposed thin-film input and output interdigital transducers, SAW devices on a piezoelectric substrate can generally be designed to provide quite complex signal processing functions.
- (2) SAW devices can be mass-produced using microelectronics fabrication techniques. As a result, they can be made to be cost-competitive in mass-volume applications.
- (3) SAW devices can have outstanding reproducibility in performance.
- (4) There are no moving parts that may suffer from wearing out during operation.
- (5) SAW devices can be made to operate very efficiently at high-harmonic modes [13].

As a result, gigahertz-frequency devices can be fabricated using relatively inexpensive photolithographic techniques, rather than the significantly more expensive process involving electron-beam (E-beam) lithography.

1.4 Outline of SAW microfluidics

The signal processing and frequency response characteristics of a SAW device on a piezoelectric substrate are governed by the geometry of the metal-film IDTs deposited on the substrate. An IDT includes electrode bus bars and electrode fingers, extending from each electrode bus bar in an interdigitated configuration. The input and output transducers typically include interdigital electrodes formed on the top surface of the substrate. The shape and spacing of the electrodes determine the center frequency and the band shape of the acoustic waves produced by the input transducer. The amplitude of the surface acoustic waves at a particular frequency is determined by the constructive interference of the acoustic waves generated by the transducers. The geometry of the interdigital transducers (beam width, pitch, and number of fingers) on the piezoelectric substrate plays a significant role in the signal processing and frequency response characteristics of a SAW device.

Two IDTs are required in a basic SAW device configuration as depicted in Fig. 1.1. One of these acts as the device input and converts signal voltage variations into mechanical surface acoustic waves (utilizing the reverse piezoelectric effect). The other IDT is employed as an output electrode, the receiver, to convert mechanical vibrations back into output voltages (direct mode). Such energy conversions require the IDTs to be used in conjunction with elastic surfaces that are also piezoelectric.

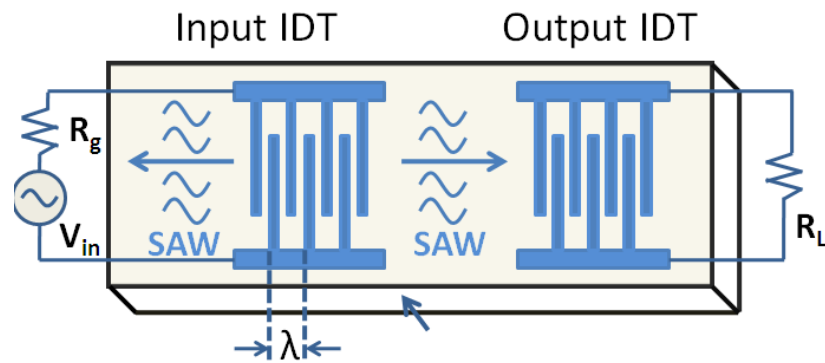


Figure 1.2 Basic SAW delay line fabricated on a piezoelectric substrate

1.5 Objectives of the research

Major electrical engineering product designs have been generated due to the development of the SAW. Currently, the largest markets for SAW applications are as filters in cell phones and in sensor applications. Recently, the extent of SAW device applications has rapidly expanded, including SAW-based microfluidics and SAW biochemical sensors. Most of the applications using SAW devices made from bulk substrates such as LiNbO_3 and LiTaO_3 and quartz which are expensive and fragile, and most importantly they cannot be integrated with electronics for control and signal process. This research focuses on the development of SAW-based microfluidics and their potential applications in biodetection, and clarifies the mechanism of acoustic pressure and interaction between the acoustic wave and liquids.

The primary intentions of this research are to develop a low-cost piezoelectric thin film based SAW technology, and to use this technology to develop SAW-based microfluidics and sensors, with the final target to develop SAW single-mechanism

driven lab-on-a-chip with integrated microfluidics and sensors for biological and medical applications.

The thesis consists of 9 chapters. After a brief introduction in this chapter, Chapter 2 will focus on a review of microfluidics technologies, particularly the non-mechanical micropumps, and then goes on to surface acoustic wave based microfluidics.

Chapters 3 and 4 then detail the basic properties of the surface acoustic wave and an outline of the stress and strain relationships in piezoelectric solids is given in order to relate the material aspects of the SAW devices. The wave equation on the bulk substrate and layer structure of the SAW will be theoretically investigated. In chapter 5, different parameters of SAW device layout are proposed, and the subsequent section details the mask design and fabrication process flow.

Next in chapter 6, the wave mode on the LiNbO_3 substrate and a ZnO/Si layer structure will be investigated. Both designs have fundamental and higher modes; the higher mode wave is of great interest, since the higher operating frequency can be realized without high-resolution fabrication techniques. The higher modes of these two designs have completely different performance. Both the fundamental and higher modes exhibit the ability to stream within droplets, and is discussed in detail in Chapter 7.

Lastly, the report investigates the micropump that induces movement in a small droplet. For successful micropump applications, an hydrophobic coating is important to reduce the voltage needed to move the droplet. In chapter 8, the main focus is on the optimisation of the hydrophobic coating, which has a low surface energy and is bio-compatible and non-reactive. An experimental set-up was designed to test the force needed to move a droplet on differently-coated substrates with different surface treatments. Also, the mechanical wave of the SAW device causes a large increase in

surface temperature which can quickly heat small liquid droplets and cause their evaporation; temperature-voltage curves are experimentally recorded and solutions are given to minimize this problem.

And finally the concluded work is in chapter 9, and highlights problems, shortages and possible future development.

Reference

- ¹ M. T. Taylor, P. Nguyen, J. Ching and K. E. Petersen. "Simulation of microfluidic pumping in a genomic DNA blood-processing cassette". *J. Micromech. Microeng.* 13 (2003) 201.
- ² A. T. Woolley, D. Hadley, P. Landre, A. J. Demello, R. A. Mathies and M. A. Northrup. "Functional integration of PCR amplification and capillary electrophoresis in a microfabricated DNA analysis device". *Anal. Chem.* 68 (1996) 4081.
- ³ N.-T. Nguyen, X. Huang and T. K. Chuan. "MEMS - Micropumps: A Review". *J. Fluids Eng.* 124 (2002) 384.
- ⁴ P. Woias. "Micropumps - past, progress and future prospects". *Sensors and Actuators B.*105(2005) 28.
- ⁵ N. T. Nguyen and Z. Wu. "Micromixers – a review". *J. Micromech. Microeng.* 15 (2005) pp. R1.
- ⁶ N. M. White and G. R. Leach. "Fabrication of a thick film sensor employing an ultrasonicoscillator". *IEE Proc. Sci. Meas. Technol.* Vol. 142 (No.3) (1995) 249.
- ⁷ D. Damjanovic. "Stress and frequency dependence of the direct piezoelectric effect in ferroelectric ceramics". *J. Appl. Phys.* 82(Issue.4) (1997) 1788.
- ⁸ N. W. Hagood, W. H. Chung and A. V. Flotow. "Modelling of piezoelectric actuator dynamics for active structural control". *J. Intell. Mater. Syst. Struct.* Vol. 1(No. 3) (1990) 327.
- ⁹ Lord Rayleigh. "On waves propagating along the plane surface of an elastic solid". *Proc. London Math. Soc.* Vol.7 (1885) 4.
- ¹⁰ R.M. White and F.W.Voltmer. "Direct piezoelectric coupling to surface elastic waves," *Appl. Phys. Lett.*, Vol.17,pp.314-316,1965.
- ¹¹ V.K. Varadan, W. D. Suh, P.B. Xavier, K.A.Jose and V. V. Varadan. "Design and development of a MEMS-IDT gyroscope". *Smart. Mater. Struct.* 9 (2000) 898.
- ¹² D. T. Bell and C. M. Li. "Surface acoustic wave resonators". *Proc. IEEE* 64 (1976) 711.
- ¹³ R.C.Williamson. "Case studies of successful surface-acoustic-wave devices". *Proc.*

1977 IEEE Ultrasonic Symposium, Oct.26-28,1977,Phoenix, AZ, IEEE Cat. No. 77CH1264-1SU (1977) 460.

Chapter 2. Introduction of Microfluidics

2.1 Microfluidics

Microfluidic systems have gained great attention in recent years in various fields. Microfluidics has the potential of revolutionary impact on chemical analysis and synthesis, biological analysis and detection, and life science and medical diagnosis as miniaturizing fluid handling systems is becoming even more pronounced in chemistry and biotechnology [1, 2, 3]. Microfluidic applications cover micro arrays, DNA sequencing, sample preparation and analysis, cell separation and detection. The use of microfluidics in these applications attracts interest because of its possible advantages: the need for small amounts of samples and reagents, short reaction times and low cost. The number of archival journal papers on microfluidics has been increasing almost exponentially in the past few years.

Microfluidic devices may consist of microchamber, channels, valves, mixers, pumps and heat exchangers etc. These components allow dilution, flow switching, separation, mixing, pumping, reaction of materials and reagents dispensing or injection. Of all the microfluidic component devices, the micromixer and micropump are the most essential ones as the control of fluid transport at the microscale is the most crucial task.

Due to the efforts of many researchers in the fast developing field of MEMS, many different types of micromixers and micropumps have been designed to handle small, precise volumes of liquid samples and reagents. The fabrication of microfluidics is normally based on MEMS technology. The basic substrate materials are silicon and

glass. Recently, arising from the need for low cost, polymers have been extensively used. In the following section, various types of micromixers and micropumps will be discussed.

2.2 Micromixers and micropumps

Miniaturization is the recent trend in biological and chemical analysis [4]. From biology and medicine to microelectronics cooling, fluid volumes are on the order of a milliliter to nanolitres or below [5]. The number of archival journal papers on microfluidics has been increasing almost exponentially. Kakuta *et al.* gave an early review on micromixers [6]. A section in the book of Oosterbroek was dedicated to a few types of micromixers. Auroux *et al.* [7], Vilkner *et al.* [8] and Erbacher *et al.* [9] also dealt with micromixers. Rapid mixing is essential in many of the microfluidic systems used in biochemistry analysis, drug delivery and sequencing or synthesis of nucleic acids. Mixing is also necessary in lab-on-a-chip platforms for complex reactions. Besides micromixers, micropumps are other important components in a microfluidic system. Micropumps normally involve dispensing reagent or transporting fluids [10,11,12]. Although fluids (typically liquids) might be introduced or transported during operation externally, micropumps are only found in very new generation microanalysis systems. Liquid transport is often accomplished through manual pipetting. The limited use of the micropump may be partly due to the lack of available micropumps with the necessary combination of cost and performance.

In general, micromixers can be categorized as passive micromixers and active micromixers. Passive micromixers do not require external energy to operate, having no moving part. Initially the passive mixer relies mainly on molecular diffusion. Increasing the contact surface between different fluids and decreasing the diffusion path between them could improve diffusion. However diffusion at the microscale without external turbulence is an extremely slow process due to low Reynold's number. Two fluids entering into a channel from different sections often remain

totally separated which is not a desirable situation for microreaction. Complete mixing is still a problem for microfluidic systems.

The other types are the active micromixers, which use the disturbance generated by an external field for the mixing process. Thus, active mixers can be categorized by the types of external disturbance effects such as pressure, electrohydrodynamics, electrokinetics and acoustics. Deshmukh *et al.* [13] reported a mixer with pressure disturbance, which is fabricated in silicon using Deep Reactive Ion Etch (DRIE). The structure of the micromixer with electrohydrodynamic disturbance [14] is similar. Instead of pressure sources, electrodes are placed along the mixing channel. Acoustic actuators have also been used to stir fluids in micromixers. Zhu and Kim [15] demonstrated an acoustic micromixer using a zinc oxide membrane located at the bottom of mixer.

Micropumps may be also categorized as either mechanical pumps or nonmechanical pumps. Nonmechanical pumps add momentum to the fluid by converting another nonmechanical energy form into kinetic energy. A number of principles such as electrohydrodynamic (EHD), electrokinetic, ultrasonic micropumps are reported. Bart *et al.* reported an EHD micropump using an EHD induction effect [16], and Richter *et al.* made an EHD pump using an EHD injection effect [17].

In mechanical pumps, energy is periodically or continuously added. These forces then result in a direct increase in pressure difference up to the value required to drive the fluid. Generating high pressure and flow rate are the major advantages of these micropumps.

2.3 Surface acoustic wave based mixing and micropump

As mentioned above, there are various types of microfluidics. In this study, a surface acoustic wave (SAW) has been utilized to actuate droplets on a planar surface. SAW

devices have been widely used in RF signal processing and band pass filter applications, and have thus become the basis of a huge industry in mobile communications [18]. Moreover recently published work has demonstrated the use of surface acoustic waves in microfluidic systems. Specifically, Katsumi Chono *et al.* have used SAWs in an atomization system [19], while, Strobl *et al.* have worked on a mixing system and a fluidic actuator based on SAWs [20, 21]. SAWs can also be used for the localisation of liquid droplets on a substrate [22]. Alzuaga *et al.* have developed a large scale X–Y positioning and localisation system for liquid droplets using a SAW on a LiNbO₃ substrate [22].

2.3.1 Wave mode propagating in the SAW devices

The Rayleigh waves cause an acoustic radiation pressure from retrograde elliptic motion. This wave format is created through the piezoelectric material on the surface expanding and contracting in a defined location and frequency, resulting in wave motion on the substrate surface. SAW devices have an IDT on the piezoelectric material that acts as the excitation agent. In most materials, the wave motion quickly dampens out beyond the IDT [23, 24].

SAWs on bulk substrates, such as LiNbO₃ and LiTaO₃, are widely used, due to their strong piezoelectricity. Elastically homogeneous single-crystal substrates are required for high-performance devices, due to the characteristics of SAWs propagating on the substrate surfaces [25, 26, 27]. The Rayleigh wave propagates at the Rayleigh velocity of the substrate material. By designing the parameters of the IDT, the SAW can be operated at the selected frequency.

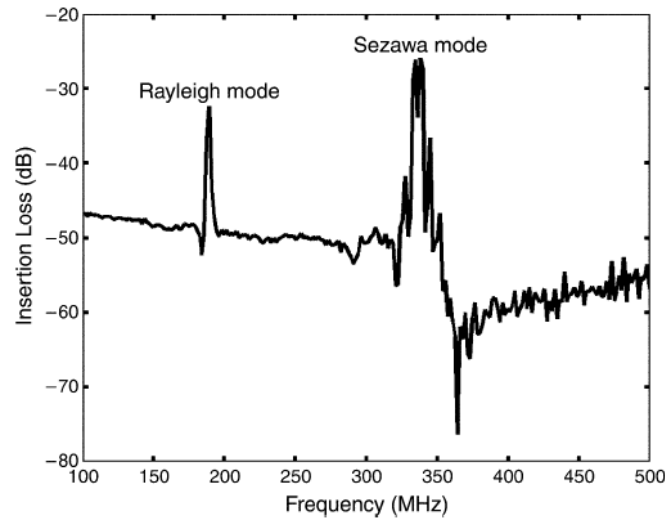


Figure 2.1 Rayleigh and Sezawa modes in the frequency response of the delay line

In addition to the SAW based on bulk piezoelectric materials, SAWs based on piezoelectric thin films deposited on wafers have also been fabricated. Gallium nitride (GaN) and Zinc oxide (ZnO) piezoelectric films are of the greatest technological interest, and much theoretical as well as technological work has been carried out on GaN and ZnO layers deposited on dielectric and semiconducting substrates. Petroni *et al.* [28] fabricated and characterized GaN-based SAW filters on sapphire (Al_2O_3). Figure 2.1 shows Rayleigh and the higher order Sezawa modes in the GaN/ Al_2O_3 substrates.

By changing the ratio of the thickness of the GaN thin film to the wavelength, the velocities of the Rayleigh and the Sezawa mode can be varied. Shown below is a table of the acoustic velocity trend on a 2 μm thick GaN layer for four different frequencies.

Table 2.1 Rayleigh and Sezawa acoustic wave velocities

Wavelength (μm)	Acoustic wave velocity (m/s) Rayleigh 0th	Acoustic wave velocity (m/s) Sezawa
8	4523	
16	5022	8500
24	5226	9250
28	5299	9490

Unlike the wave generated by the bulk piezoelectric substrate, the propagation velocity of the wave is a constant. The SAW velocity of the GaN/sapphire SAW increases with the increase of wavelength. This is ascribed to a deeper penetration of the SAW in the sapphire substrates. The wave velocity approaches the sapphire acoustic speed when the GaN piezoelectric layer thickness is reduced with respect to the wavelength.

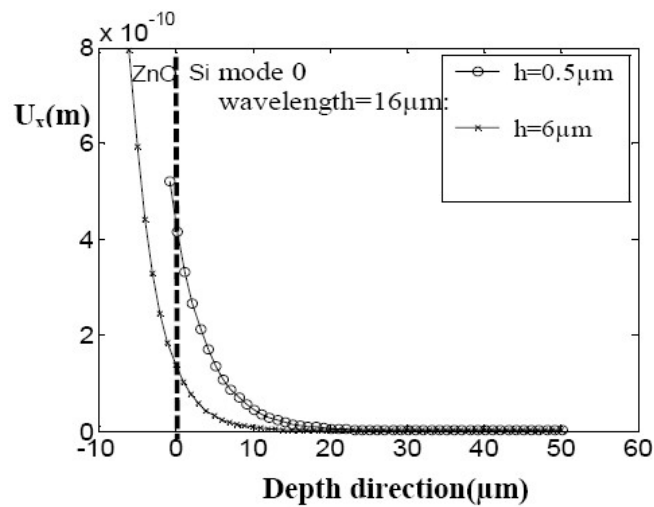


Figure 2.2 Dependence of particle displacement with respect to the penetration depth into the ZnO film on Si(100) for mode 0 [29]

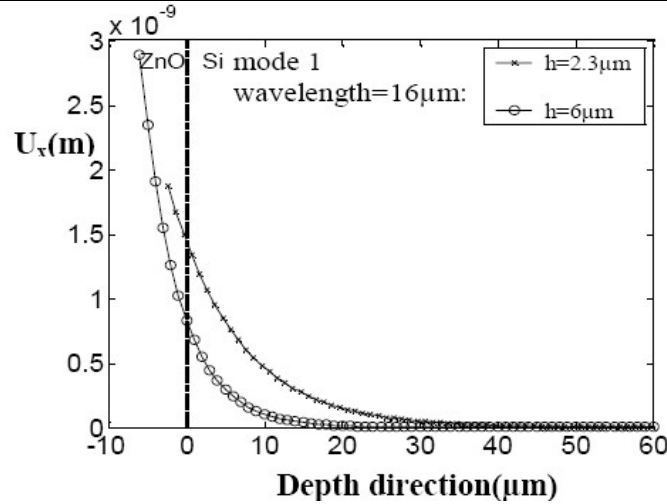


Figure 2.3 Dependence of particle displacement for second Rayleigh mode (Sezawa mode, mode 1)

For SAW device waves, the longitudinal wave length is in the micron range, while the amplitude on the surface wave is only a few nanometres [30]. Talbi *et al.* investigated the displacement of the particles as a function of the ratio of the thickness of the piezoelectric (h/λ) ZnO layer to the wavelength, shown in Fig. 2.2 & 2.3.

The mechanism of the SAW on a GaN layer on a sapphire substrate is the same as that of the ZnO layer deposited on the silicon wafer. In these cases, the substrate material exhibits a higher acoustic velocity than the piezoelectric film. The velocity of the waves is not constant, but varies with the thickness of the piezoelectric layer at a fixed wavelength. This variation is ascribed to the increasing depth of SAW waves into the high-velocity substrate as the wavelength gets larger than the piezoelectric thickness.

For the 16 μm wavelength, $h=0.5 \mu\text{m}$, $2.3 \mu\text{m}$ and $6 \mu\text{m}$ correspond to the ratio h/λ 0.031, 0.144 and 0.375. In Fig.2.2 & 2.3, if the film thickness is much smaller than the wavelength ($h/\lambda=0.031$, 0.144), the SAWs are localized in the immediate vicinity of the surface, and the wave is cut off by the interface between the film and substrate. Thinner films can lead to the wave's deeper penetration into the substrate.

2.3.2 Micromixers

The acoustic waves travel from the input interdigital transducer to the output interdigital transducer. This nanometer displacement of the surface creates the forces that transfer energy into the material or liquid on top of the substrate. When the surface is hydrophilic and the acoustic force is small not sufficient to move the droplet, the acoustic energy from the vibration causes internal acoustic streaming within the liquids, that can then be utilized as a micromixer, i.e. a SAW-based micromixer. From the Rayleigh wave, a diffraction angle corresponding to the calculated Rayleigh diffraction angle can be found [23]:

$$\theta_R = \text{Arc sin} \left(\frac{V_{liq}}{V_{sub}} \right) \quad (2.1)$$

The sound velocity of the liquid, V_{liq} , is approximately 1500 m/s and the velocity of the acoustic wave in the substrate, V_{sub} , is ~ 3500 m/s.

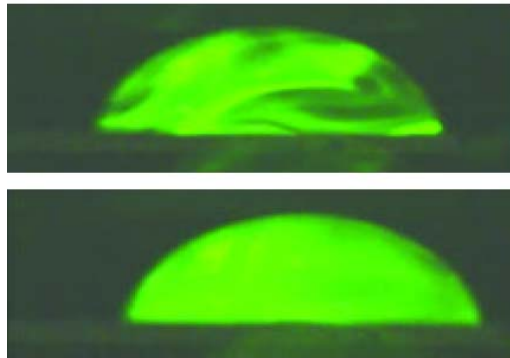


Figure 2.4 SAW induced internal streaming in a small water droplet (side view)

Wixforth *et al.* [26] demonstrated that the acoustic force can be used to stream within the droplet. A dried fluorescent dye on the surface of the chip is dissolved by the SAW agitation, and rapidly fills the whole droplet volume. The acoustic force is excited at the Rayleigh angle.

Depending on the position of the applied SAW relative to the droplet, the induced streaming will have different patterns. Figure 2.5 shows how the flow pattern within glycerol/water droplets change with the position of the applied SAW by Ito *et al.* [31].

Ito *et al.* also found that 40s after the application of the SAW, the temperature of the droplet increased from 25°C to 40°C. Both of these phenomena have important consequences on microfluidics or lab-on-a-chip: firstly the application of SAW to a SAW-based microfluidic system needs to be controlled so that the acoustic heating of the droplet can be minimized so that it does not cause evaporation or damage the contents of the droplet. Secondly, the dynamics of the droplet motion is dependent on the position of the applied SAW, so that it can be designed for different applications.

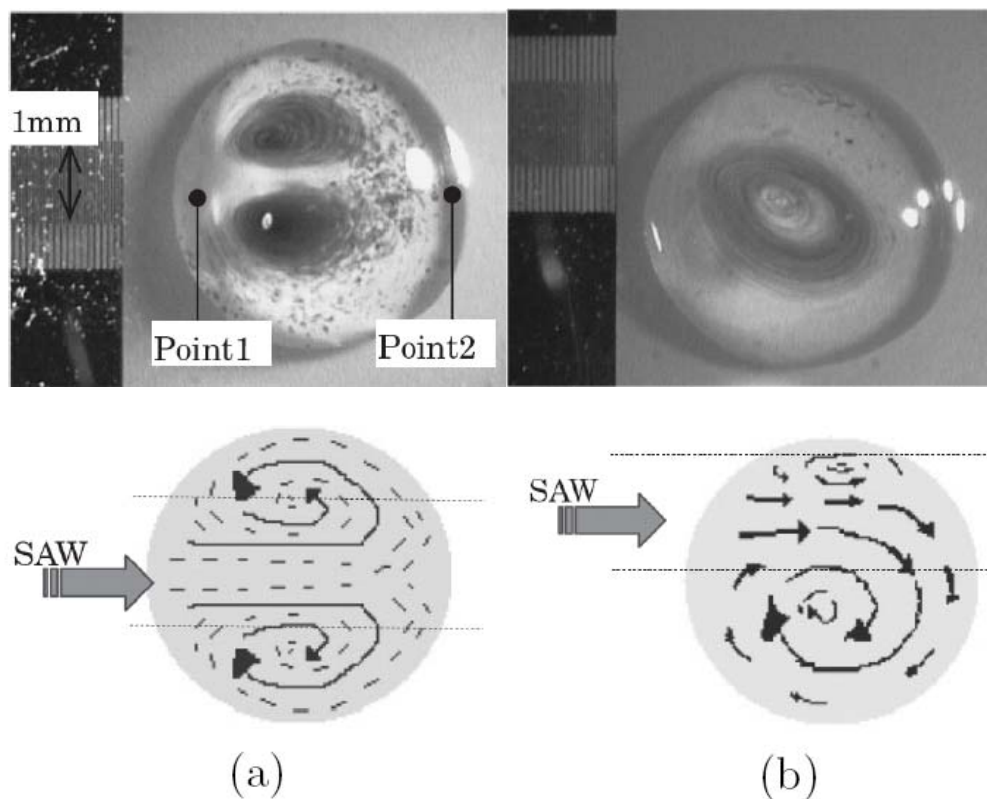


Figure 2.5 Photographs and illustrations of a SAW applied to (a) the center and (b) the side of a glycerol/water droplet [32]

Researchers from the National Cheng Kung University in Taiwan have shown highly effective mixing using SAWs [32]. The disadvantage of the increased voltage is an increase in temperature of the liquid, which may be critical for any temperature-sensitive bio-samples. An almost linear relationship between the rise in temperature and the signal voltage has been found in Fig.2.6 [33].

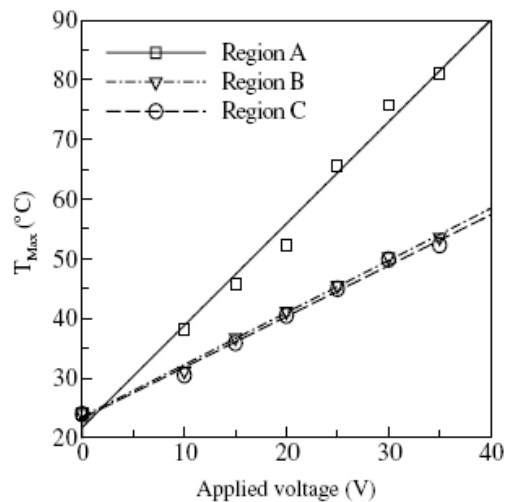


Figure 2.6 Temperature vs applied voltage for the SAW mixer [33]

2.3.3 Micropumps

By increasing the power applied to the SAW device, the SAW generated in the liquid will cause the droplet to deform and move along the surface. Renaudin's group compared the acoustic actuation power and the hydrophobicity of the surface. They showed that, a high power of 32 dBm is needed for a 2 μ l droplet transportation on a bare hydrophilic surface [31]. However, once the substrate is coated with a thin hydrophobic octadecyltrichloro-silane (OTS) hydrophobic layer, the power required to transport the droplet of the same size dropped to 27 dBm. Figure 2.7 shows the droplet motion on the OTS treated surface.

Wixforth *et al.* showed, by utilizing hydrophilic areas on the mostly hydrophobic surface, that virtual channels and reservoirs can be formed by standard optical photolithograph techniques [24]. Within the channels and reservoirs, droplets of different samples or different concentrations can be effectively mixed or separated into smaller droplets. They showed that separation of droplets down to 50 pl size was possible.

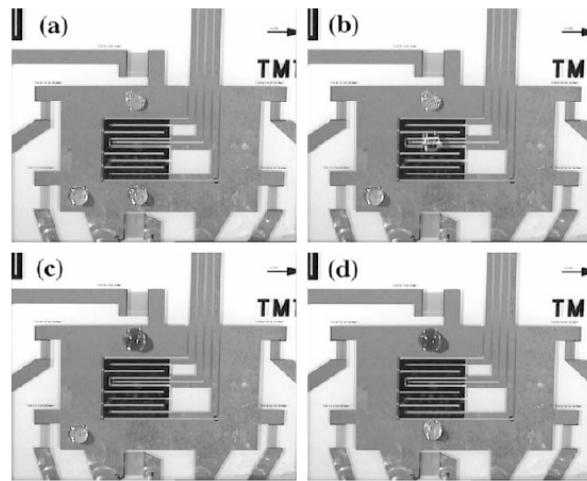


Figure 2.7 Independent droplet movement and droplet mixing [31]

In their flow profiling of SAW nanopumps, Guttenberg *et al.* studied the relationship between the RF power applied to the IDT electrode and the fluid velocity and distance transported from the IDT fingers [33]. Using a small capillary gap between the device and a slide, flow rates were measured using a Na-Fluorescein solution with images obtained by a video microscope. The continuous flow experiment produced a low Reynolds number (>1) and hence laminar flow. The results showed a clear one to one relationship between the flow velocity and the RF power applied as shown in Fig.2.8. It was found that as the liquid droplet moved 1 mm away from the IDT electrode, the force decreased by three orders of magnitude and the flow rate decreased by the inverse third power.

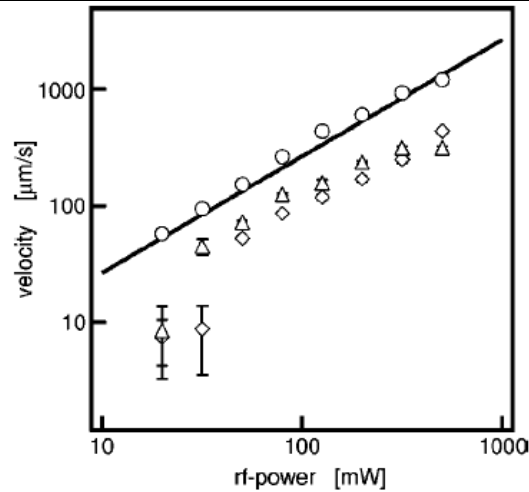


Figure 2.8 Comparison of flow velocity vs RF-power [34]

Studies carried out by Beysen *et al.* showed that the motion of a droplet driven by an applied surface acoustic wave consists of a periodic motion. Fig. 2.9(b) shows how the height and diameter of the droplet change with time, the frequency of the $2\ \mu\text{m}$ droplet motion is 120Hz. They found that for each distortion cycle, the droplet moved a distance between $100\text{-}150\ \mu\text{m}$.

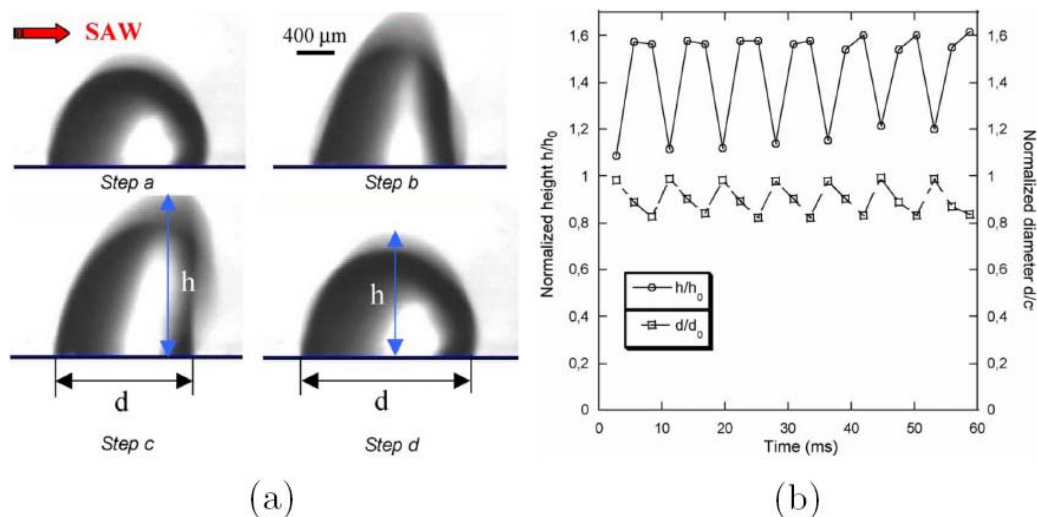


Figure 2.9 (a) periodic distortion of droplet and normalised height and diameter of droplet with time

Figure 2.9 shows the periodic distortion of the droplet. Before the SAW is generated, the droplet has a spherical shape, and then the droplet stands up due to being hit by

the SAW. The droplet then bends, advances and adopts a spherical shape again. Figure 2.9(b) shows the normalised height and diameter of the droplet with time [34].

2.4 Conclusions

The Rayleigh waves cause an acoustic radiation pressure from retrograde elliptic motion. This wave format is created from piezoelectric material on the surface expanding and contracting in a defined location and frequency resulting in wave motion on the substrate surface.

For SAW devices waves, the longitudinal wave length is in the micron range while an amplitude of the surface wave of a few nanometres range created forces from amplification of the surface, which transfer energy into the surface and any material/liquid on top of the substrate. The energy from the vibration causes internal acoustic streaming in liquids. By utilizing hydrophobic coating on the device surface, the droplets can overcome the surface adhesion and can be effectively moved.

Reference

- ¹ N. T. Nhuyen and S. Wereley. *Fundamental and applications of microfluidics*. 2002 Boston: Artech House.
- ² O. Geschke, H. Klank and P. Telleman. "Microsystem engineering of lab-on-a-chip devices". 2004 2nd edn. New York: Wiley.
- ³ N. T. Nguyen, X. Y. Huang and K. Toh. "MEMS-micropumps: a review". *ASME Trans. J. Fluids Eng.* 124 (2002) 384.
- ⁴ N. T. Nguyen and Z. Wu. "Micromixers- a review". *J.Micromech. Microeng.* 15 (2005) R1.
- ⁵ D. J. Laser and J. G. Santigo. "A revire of micropumps". *J. Micromech. Microeng.* 14 (2004) R35.
- ⁶ R. E. Oosterbroek and Van den Berg. "Lab-on-a-chip: Miniaturized system for bio(Chemical) analysis and synthesis". 2003 Amsterdam: Elsevier.
- ⁷ P. A. Auroux, D. Iossifidism, D. R. Reyes and A. Manz. "Micro total analysis systems: 2. Analytical standard operations and applications". *Anal. Chem.* 74 (2002) 2637.
- ⁸ T. Vilkner, D. Janasek and A. Manz. "Micro total analysis systems. Recent developments". *Anal. Chem.* 96 (2004) 3373.
- ⁹ C. Erbacher, F. G. Bessoth, M. Busch, E. Verproorte and A. Manza. "Towards integrated continuous-flow chemical reactors". *Mikrochim. Acta.* 131 (1999) 19.
- ¹⁰ T. T. Veenstra, T. S. J. Lammerink, M. C. Elwenspoek and A. van den berg. "Characterization method for a new diffusion mixer applicable in micro flow injection analysis system". *J. Micromech. Microeng.* 9 (1999) 199.
- ¹¹ R. J. Jackmsn, T. M. Floyd, R. Ghodssi, M. A. Schmidt and K. F. Jensen. "Microfluidic system with on-line UV detection fabricated in photodefineable epoxy". *J. Micromech. Microeng.* 11 (2001) 263
- ¹² I. Kanno, S. Kawano, S. Yakushiji and H. Kotera. "Characterization of piezoelectric micropump driven by traveling waves". *Proc. uTAS 2003* 997.

- ¹³ A. A. Deshmukh, D. Liepmann and A. P. Pisano. "Continuous micromixer with pulsatile micropumps". Technical digest of the IEEE solid state sensor and actuator workshop (Hilton Head Island, SC) (2000) 73.
- ¹⁴ A. O. El Moctar, N. Aubry and J. Batton. "Electrohydrodynamic micro-fluidic mixer". Lab on a chip. 3 (2003) 273.
- ¹⁵ X. Zhu and E.S.Kim. "Acoustic-wave liquid mixer". MEMS American society of Mechanical Engineers, Dynamic Systems and Control Division (Publication) DSC 62 (1997) 35.
- ¹⁶ S. F. Bart. "Microfabricated electrohydrodynamic pumps". Sensors and Actuators A. 193 (1990) 21.
- ¹⁷ G. Fuhr, T. Schnelle and B. Wagner. "Travelling wave-drive microfabricated electrohydrodynamic pumps for liquids". J. of Micromech. Microeng. 4 (1994) 217.
- ¹⁸ C.K. Campbell. Editor. Surface Acoustic Wave Devices for Mobile and Wireless Communications. Academic Press (1998).
- ¹⁹ K. Chono, N. Shimizu and Y. Matsui. "Development of novel atomization system based on SAW streaming". Jpn J. Appl. Phys. 43(5b) (2004) 2987.
- ²⁰ C.J. Strobl, A. Rathgeber and A. Wixforth. "Planar microfluidic processors". Planar microfluidic processors, IEEE Ultrason. Symp. 1 (2002) 255.
- ²¹ S. Alzuagua, W. Daniau, J.F. Manceau, S. Ballandras and F. Bastien. "Displacement of droplets on a surface using ultrasonic vibration". World Congress on Ultrasonics, September 7 Paris, France (2003).
- ²² S. Alzuaga, S. Ballandras, F. Bastien, W. Daniau, B. Gauthier-Manuel and J.F. Manceau. "A large scale X-Y positioning and localisation system of liquid droplet using SAW on LiNbO₃". 2003 IEEE.
- ²³ A. Renaudin, P. Tabourier, V. Zhang, J.C. Camart and C. Druon. "SAW nanopump for handling droplets in view of biological applications". Sensors and Actuators B. 113 (2006) 389.
- ²⁴ A. Wixforth, C. Strobl, C. Gauer, A. Toegl, J. Scriba, and Z. v. Guttenberg. "Acoustic manipulation of small droplets". Anal. Bioanal. Chem. 379 (2004) 982.

- ²⁵ K. Yamada, T. Omi, S. Matsumura and T. Nishimura. “Characterization of 4-inch LiTaO₃ single crystals for SAW device application”. IEEE Ultrason Symp. Proc. (1984) 243.
- ²⁶ K. Yamada, H. Takemura, Y. Inoue, T. Omi and S. Matsumura. “Effect of Li/Nb ratio on the SAW velocity of 128° Y-X LiNbO₃ wafer”. Jpn. J. Appl. Phys. 26 (Suppl.26-2) (1987) 219.
- ²⁷ M. Sato, A. Iwama, J. Yamada, M. Hikita and Y. Furukawa. “SAW velocity variation of LiTaO₃ substrates”. Jpn. J. Appl. Phys. 28 (Suppl.28-1) (1989) 111.
- ²⁸ S. Petroni, G. Tripolia, C. Combia, B. Vignaa, M. De Vittoriob, M.T. Todarob, G. Epifanib, R. Cingolanib and A. Passaseob. “GaN-based surface acoustic wave filters for wireless communications”. Superlattices and Microstructures”. 36 (Issues 4-6) (2004) 825.
- ²⁹ A. Talbi, F. Sarry, L. L. Brizoual, O. Elmaria and P. Alnot. “Sezawa mode SAW pressure sensors based on ZnO/Si structure”. IEEE Transactions on Ultrasonics, Ferroelectrics and Frequency Control. Vol. 51(No. 11) (2004) 1421.
- ³⁰ S. V. Biryukov, Y. V. Gulyaev, V. V. Krylov and V. P. Plessky. “Surface acoustic waves in inhomogeneous media”. (Berlin: Springer) 1995 chapter 1.2
- ³¹ S. Ito, M. Sugimoto, Y. Matsui and J. Kondoh. “Study of surface acoustic wave streaming phenomenon based on temperature measurement and observation of streaming in liquids”. Jpn. J. Appl. Phys. Part 1 46(7B) (2007) 4718.
- ³² W.K. Tseng, J.L. Lin, W.C. Sung, S.H. Chen and G.B. Lee. “Active micro-mixers using surface acoustic waves on Y-cut 128° LiNbO₃”. J. Micromech. Microeng. 16, (2006) 539.
- ³³ Z. Guttenberg, A. Rathgeber, S. Keller, J. O. Rädler, A. Wixforth, M. Kostur, M. Schindler and P. Talkner. “Flow profiling of a surface-acoustic-wave nanopumps”. Physical Review E. 70 (2004) pp. 056311.
- ³⁴ D. Beyssen, L. Le. Brizoual, O. Elmazria and P. Alnot. “Microfluidic device based on surface acoustic wave”. Sensors and Actuators. B: Chemical 118(1-2) (2006) 380.

Chapter 3. Basics of Acoustic Waves and Piezoelectricity

This chapter highlights the basic properties of surface acoustic waves (SAW) and their generation (or detection) by an interdigital transducer (IDT) located on the free surface of a piezoelectric substrate.

In an unbounded isotropic solid, elastic waves can propagate with the material displacement polarized in the direction of propagation or transverse to it, each mode having a characteristic velocity dependent on the elastic properties of the material, but typically between 10^3 and 10^4 m/sec. When a boundary and interfaces are introduced, other modes become possible. Of central interest here is the so-called Rayleigh wave, where these waves are modes of propagation of elastic energy along the free surface of an infinite half-space. The displacement amplitude of the propagation waves decays at an exponential rate with depth beneath the surface, so that essentially all the associated energy density is concentrated within a distance of the order of a wavelength below the free surface [1, 2, 3]. The particle motion on the surface and at each depth is elliptical.

3.1 Mechanical motion of surface acoustic wave

The propagation of a surface acoustic wave on an unbounded elastic surface is associated mechanically with a time-dependent elliptical displacement of the surface structure. One component of this physical displacement is parallel to the SAW propagation axis, while the other is normal to the surface. This is depicted in Fig. 3.1,

where x relates to the SAW propagation axis, while y is a surface normal axis in a Cartesian coordinate system [4, 5, 6]. Surface particle motion is then predominantly in the y - x -plane in Fig.3.1. The two wave motions are 90° out of phase with one another in the time domain, so that when one displacement component is maximum at a given instant the other will be zero. In addition, the amplitude of the surface displacement along the y -axis is larger than that along the SAW propagation axis x . This can be appreciated intuitively, since it is “easier” for the crystal structure to vibrate in the unbounded direction than in the bounded one. The amplitude of both SAW displacement components become negligible when the penetration depth into the solid (y) is greater than the sum of a few acoustic wavelengths (λ).

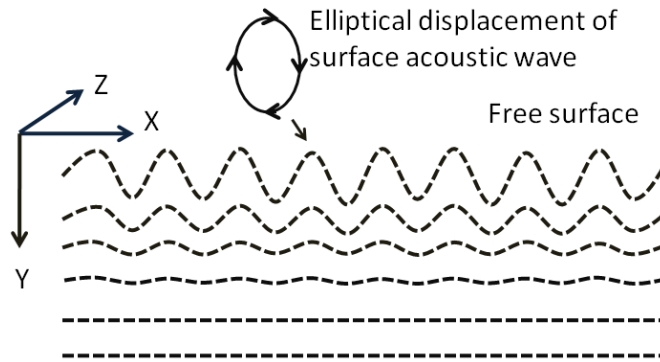


Figure 3.1 Pictorial representation (not to scale) of surface acoustic wave motion on the surface of an elastic solid

3.2 Stress and strain in a non-piezoelectric elastic solid

The relationship between mechanical stress T and strain S for small static deformations of a non-piezoelectric elastic solid is first considered. Stress is the force F applied per unit area A of the solid. Moreover, stress, force and area can all be represented as vector quantities so that $T=F/A$ [7, 8]. The units of T are N/m^2 when force F is expressed in Newtons (N). In addition, the strain parameter S , which represents the fractional deformation due to force F , can be defined as $S=\Delta/L$ (dimensionless), where Δ is the fractional deformation of the solid with length L .

Stresses and strains exerted within an elastic solid can exist in compressive or shear form. For example, with compressive stresses, the applied force F is normal to the surface area A . In either case, they can be related proportionally by Hooke's Law for elastic deformations. As the stresses and strains associated with elastic waves in solids are small, well below the elastic limits, for the compressive stress and strain along the same axes, this can be written as [9]:

$$T = cS \quad (3.1)$$

where c is the elastic stiffness coefficient, also known as Young's modulus (N/m^2).

3.4 The electromechanical coupling coefficient, K^2

The wave itself contains both kinetic and potential energy, which will vary depending on the wave amplitude and wave speed. For an ideal device, the total energy of the wave is equivalent to the total electrical energy supplied to the IDT. However, in the real world, the wave energy will always be less than the total energy supplied. Among the main causes of energy dissipation is the low electromechanical coupling between the IDT and the piezoelectric material.

The electromechanical coupling coefficient K^2 is a measure of the efficiency of a given piezoelectric materials in converting an applied electrical signal into mechanical energy associated with a surface acoustic wave. K^2 and SAW velocities v represent the two most important practical material parameters used in SAW design. Since K^2 values are small, they are usually expressed as percentages. Values for some typical piezoelectric substrates are given in Table 3.1 [10].

Table 3.1 The parameters of different bulk piezoelectric substrates

Material	Crystal Cut	SAW Axis	Velocity (m/s)	K^2 (%)	Applications
Quartz	ST	X	3158	0.11	Oscillators, filter
LiNbO ₃	Y	Z	3488	4.5	wideband filter
LiNbO ₃	128°	X	3992	5.3	wideband filter
LiTaO ₃	Y	Z	3230	0.72	Oscillators

Piezoelectric substrates typically employed in SAW design are listed in Table 3.1. With reference to this table, YZ-lithium niobate (LiNbO₃) substrates (Y-axis crystal cut, z-axis propagation) have relatively high values of K^2 and velocity.

For SAW wave propagation in piezoelectrics, it may be shown that the electromechanical coupling coefficient K^2 can be defined in terms of the piezoelectric coefficient e , elastic constant c and dielectric permittivity [16],

$$K^2 = \frac{e^2}{c\epsilon} \quad (3.2)$$

K^2 depends on both the crystal cut and the propagation direction of the surface acoustic wave. Additionally, the parameter K^2 in Eq.(3.3) can be derived experimentally [11].

$$K^2 = -\frac{2\Delta V}{V} \quad (3.3)$$

where $|\Delta V|$ is the magnitude of the SAW velocity change that occurs when the free surface of the piezoelectric is short-circuited by a thin, highly-conducting metal film, and V is the unperturbed SAW velocity. The time-varying electric field associated with SAW propagation will cause the metal surface film to accumulate charge, as shown in Fig. 3.3.

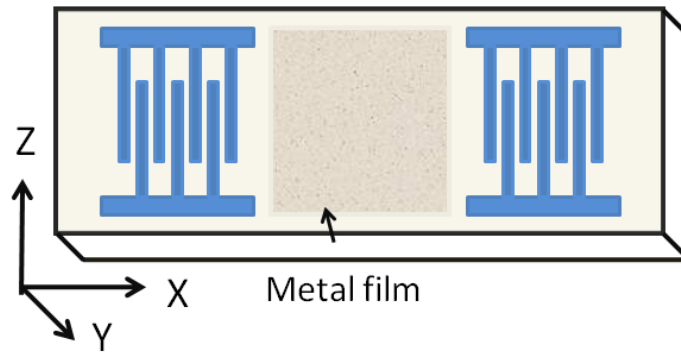


Figure 3.3 Schematic diagram of the metal film deposited at the delay line

The electromechanical coupling coefficient can be measured by observing the SAW propagation time between two IDTs, before and after a highly-conducting metal film is deposited on the surface of the piezoelectric.

3.5 SAW structure

The acoustic wave propagating along the surface of a piezoelectric material provides a means of implementing a variety of signal-processing devices at frequencies ranging from several MHz to a few GHz. The function of the IDT is to convert electrical energy into mechanical energy, and vice versa, for the generation and detection of the SAW. An IDT consists of two metal-comb-shaped electrodes placed on a piezoelectric substrate; it is a two-terminal device with alternate electrodes interconnected. An electric field created by a voltage applied to the electrodes induces dynamic strains in the piezoelectric substrate, which launch elastic waves. The waves travel perpendicularly to the electrodes, with velocity V_R . When an RF voltage is applied across the electrodes, the stress wave induced by the finger pair travels along the surface of the crystal in both directions. To ensure constructive interference and in-phase stress, the distance d between two neighbouring fingers should be equal to a quarter of the elastic wavelength λ , $d=\lambda/4$. The associated frequency is known as the resonant frequency f_r , and is given by $f_r = V_R/\lambda$ [12, 13, 14].

The velocity V_R is a function of the nature of the acoustic wave (i.e. Rayleigh, Lamb,

bulk wave, etc.) and also of the material properties of the piezoelectric film and substrate. At this frequency, the transducer efficiency in converting electrical energy to acoustical energy, or vice versa, is maximized.

A disadvantage of using transducer design is the inability to control the directionality of the wave generated. The basic IDT is bi-directional, because of the presence of backward-traveling waves. The backward-traveling wave is the result of the symmetrical IDT configuration for standard SAW devices. At the launch transducer, the wave also travels in the reverse direction and is reflected off the back edge of the substrate. No adverse effects related to interference between the transmitted and reflected waves have been experienced. The reflected wave is attenuated by approximately 50 dB by the time it returns to the launch transducer [11].

Consequently, two different types of IDTs in addition to the reflector were proposed to counter the effects of backward-traveling waves. The designs were adapted from *Elastic Waves in Solids II* (1999) [15, 16]. Illustrations for both designs can be found in Figures 3.4 (a) and (b).

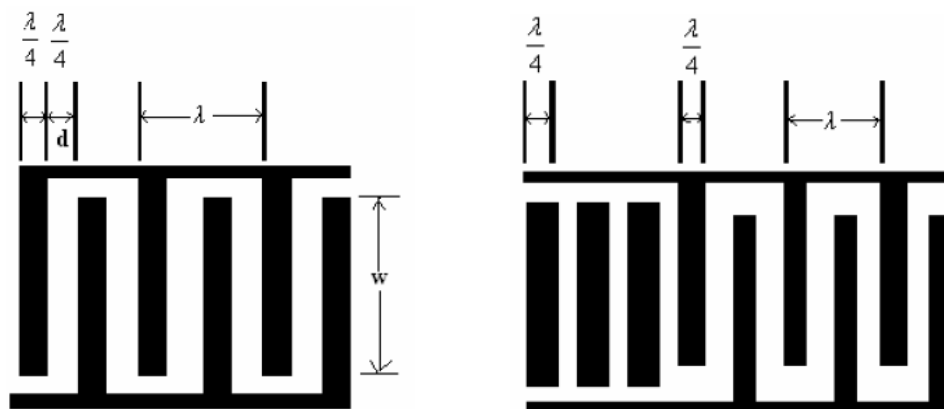


Figure 3.4 (a) Standard single-electrode IDT

(b) Reflector design

The reflected waves will have a shift of 2π and hence constructive interference will occur. Another design utilizes reflectors at one end of the basic IDT. The purpose of the reflectors is to reflect the backward-traveling wave and also to act as barriers that

dampen backward-traveling waves. The reflectors are not connected to the power supply and hence do not contribute to generated waves. This design is effective at suppressing backward-traveling waves. Efficiency could be further improved if the backward-traveling wave could be reflected and made to contribute constructively to the forward-traveling waves.

The metallization ratio $\eta=0.5$ considered here corresponds to a finger width of $\lambda/4$ at center frequency. Likewise, all of the other metal fingers in the receiving IDT will be in phase at the center frequency, so that the reflected SAW signal components will be additive, as sketched in Fig.3.5.

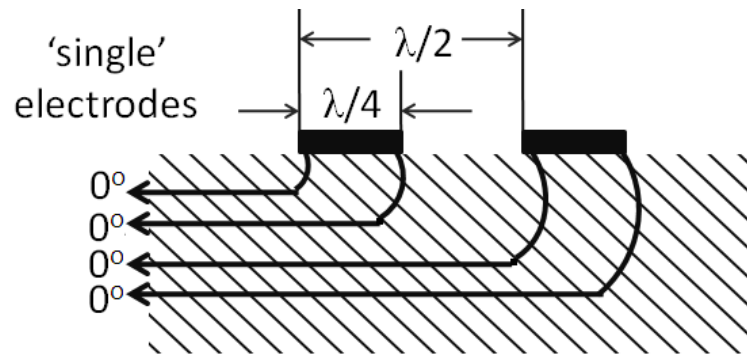


Figure 3.5 Reflection from the fingers of IDTs with “single” electrodes

SAW device theoretical model

A simple uniform IDT SAW device can be modeled using the cross-field model [17, 18, 19]. In this model the SAW IDT structure is represented by a three-port network with one electrical port and two acoustic ports. The cross-field model assumes that the electrical field distribution beneath the electrodes is normal to the surface. An alternative model that is based on the assumption that the electric field distribution beneath the electrode is parallel to the electrodes is the in-line model, but it has been found that the cross-field model is in better agreement with experimental results for high- K^2 piezoelectric substrates such as LiNbO_3 [26].

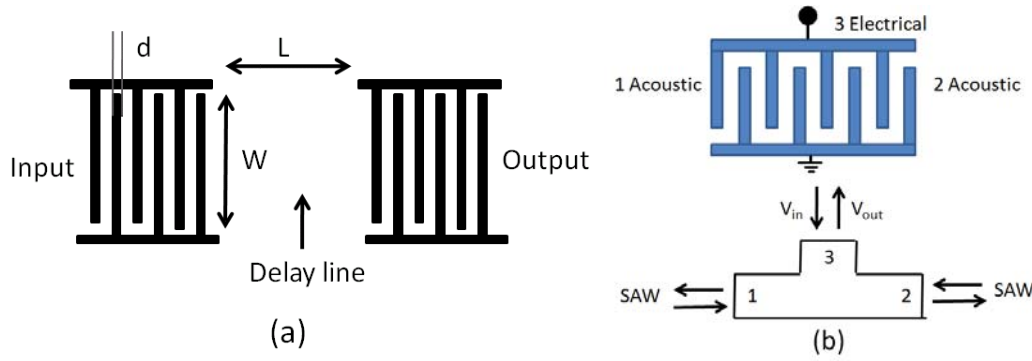


Figure 3.6(a) Basic SAW with IDTs with N finger pairs, aperture W and delay line length L (b) Equivalent 3-port network of a SAW IDT using the cross-field model [27]

By converting the acoustic ports of the three-port network to equivalent electrical ports and analyzing an N electrode pair IDT structure using matrix equivalents of the Kirchhoff voltage and current laws, the cross-field equivalent circuit of the IDT structure can be derived, as shown in Fig. 3.6. The total capacitance C_T and radiation conductance $G_a(f)$ is given by Eq. (3.4) [20, 21]:

$$G_a(f_o) \approx 8K^2 f_r C_1 N^2 w \left| \frac{\sin x}{x} \right|^2 \text{ (ohm)} \quad (3.4)$$

where N is the number of finger pairs in the IDT and W is the aperture. C_1 is the capacitance per finger pair per length and f_r is the resonant frequency. K^2 is the electromechanical coupling coefficient. f is the applied frequency and $x = N\pi(f - f_r)/f_r$. Radiation conductance represents the amount of acoustic power that is generated by the IDT. C_1 can be numerically analysed based on [25]:

$$C_1 = 2(6.5\eta^2 + 1.08\eta + 2.37) \left(\frac{\epsilon}{\epsilon_o} + 1 \right) \quad (3.5)$$

where η is the IDT metallization ratio (the ratio of finger width to interdigital distance) and ϵ/ϵ_o is the dielectric constant. C_1 is highly dependent on the effective permittivity of the piezoelectric substrates as well as the permittivity of free space.

This model neglects the acoustic reflections from IDT discontinuities, and is therefore only valid if the electrode film thickness ratio h/λ is much less than 1% (h is the thickness of the thin film and λ is the wavelength of the SAW).

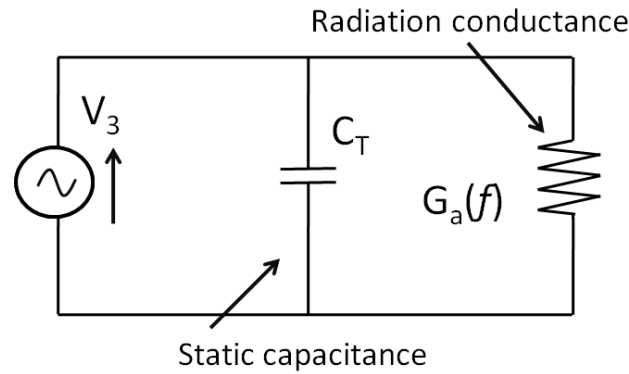


Figure 3.7 Cross-field equivalent circuit for single IDT where C_T is the total capacitance of the structure and $G_a(f)$ is the radiation conductance

3.6 Conclusions

The basic properties of the SAWs, such as wave propagation and their generation and detection by IDT are introduced. Some important parameters of different piezoelectric materials are detailed, such as electromechanical coupling coefficient K^2 and Rayleigh velocities. As K^2 is small, it is usually expressed as percentages, and the Rayleigh velocities are typically at the range of several 10^3 m/s. The SAW structures adopted in the experiment are standard single-electrode and reflector design with metallization ratio of 0.5.

Reference

- ¹ S. W. Lee, J. W. Rhim, S. W. Park and S. S. Yang. "A micro rate gyroscope based on the SAW gyroscopic effect". *J. Micromech. Microeng.* 17 (2007) 22729.
- ² M. K. Tan, J. R. Friend, and L. Y. Yeo. "Surface acoustic wave driven microchannel flow". 16th Australasian Fluid Mechanics Conference. 2-7 (2007)790.
- ³ A. A. Gubaidullin and O. Y. Kuchugurina. "Rayleigh waves in porous media saturated with liquid". *Solid Mechanics and Its Applications.* 87 (2001) 179.
- ⁴ J. Kondoh, N. Shimizu, Y. Matsui, M. Sugimoto, and S. Shiokawa. "Temperature-control system for small droplet using surface acoustic wave device". *Sensors.* 2005 IEEE. Vol1 (2005) 727.
- ⁵ M. Alvarez, J. Friend, L. Yeo and D. Arifin. "Microaerosol and nanoparticle synthesis for drug delivery via surface acoustic wave atomization". 16th Australasian Fluid Mechanics Conference. 2-7 (2007) 621.
- ⁶ D. W. Dissanayake, S. F. Al-Sarawi and D. Abbott. "Electrostatic microactuator design using surface acoustic wave devices". *Smart Sensors and Sensing Technology.* 20 (2008) 139.
- ⁷ J. F. Calzada and M. Peleg. "Mechanical interpretation of compressive stress-strain relationships of solid foods". *J. of Food Science.* 43(Issue. 4) (2006) 1087.
- ⁸ I. Mirsky and W. Parmley. "Assessment of passive elastic stiffness for isolated heart muscle and the intact heart". *Circulation Research.* Vol. XXXII (1973) 233.
- ⁹ A. Suleman and V. B. Venkayya. "A simple finite element formulation for a laminated composite plate with piezoelectric layers". *J. Intell. Mater. Syst. Struct.* 6(No.6) (1995) 776.
- ¹⁰ C. Campbell. *Surface Acoustic Wave Devices and Their Signal Processing Applications.* San Diego: Academic Press, Inc. (1989).
- ¹¹ C. K. Campbell. *Surface Acoustic Wave Devices for Mobile and Wireless Communications.* San Diego: Academic Press, Inc. (1998).
- ¹² T. T. Wu, Z. C. Hsu and Z. G. Huang. "Band gaps and the electromechanical

coupling coefficient of a surface acoustic wave in a two-dimensional piezoelectric phononic crystal”. *Phys. Rev. B.* 71 (2005) 064303.

¹³ M. S. Lee, F. C. Chang, S. Wu and L. Wu. “The characterization of surface acoustic wave modes on rotated Y-Cut quartz (ST-X Quartz) with different AlN film thickness”. *Jpn. J. Appl. Phys.* 40 (2001) 4590.

¹⁴ M. B. Assouar, O. Elmazria, P. Kirsch, P. Alnot, V. Mortet and C. Tiusan. “High-frequency surface acoustic wave devices based on AlN/diamond layered structure realized using e-beam lithography”. *J. Appl. Phys.* 101 (2007) 114507.

¹⁵ E. Dieulesaint and D. Royer, *Elastic Waves in Solids I* (Wiley. New York 1980)

¹⁶ E. Dieulesaint and D. Royer, *Elastic Waves in Solids II* (Wiley. New York 1980)

¹⁷ R. F. Milson and M. Redwood. “Interdigital piezoelectric Rayleigh wave transducer: An improved equivalent circuit”. *Electron. Lett.* 7 (1977) 217.

¹⁸ T. Aoki and K. A. Ingebrigtsen. “Equivalent circuit parameters of interdigital transducers derived from dispersion relations for surface acoustic waves in periodic metal gratings”. *IEEE Trans. Sonics Ultrason.* 24 (1977) 167.

¹⁹ V. Laude, A. Khelif, T. Pastureauud and S. Ballandras. “Generally polarized acoustic waves trapped by high aspect ratio electrode gratings at the surface of a piezoelectric material”. *J. Appl. Phys.* 90 (2001) 2492.

²⁰ G. Bu, D. Ciplys and M. Shur. “Electromechanical coupling coefficient for SAW in single-crystal bulk AlN”. *Appl. Phys. Lett.* 84 (2004) 4611.

²¹ H. Nakahata, A. Hachigo, K. Higaki, S. Fujii, S. Shikata and N. Fujimori. “Theoretical study on SAW characteristics of layered structures including a diamond layer”. *IEEE Transactions on Ultrasonics. Ferroelectrics and Frequency Control.* 42 (No. 2) (1995) 362.

Chapter 4. Elastic Wave Propagation in Thin Layers

Most SAW devices so far have been made from bulk piezoelectric materials, such as LiNbO_3 and quartz [1, 2]. These bulk piezoelectric materials are expensive, and cannot be integrated with control electronics, preventing them from widespread application in microfluidics.

Recently, SAW devices using piezoelectric thin films such as ZnO have been developed. ZnO has good piezoelectric properties, a high electro-mechanical coupling coefficient, and high sensitivity and reliability [3]. It can be grown in thin-film form by many thin-film deposition methods such as RF magnetron sputtering and laser-assisted deposition on a variety of substrates, including silicon, making it a most promising material for integration with electronic control circuitry [4, 5]. Such integration is the prerequisite for a fully automated and digitized microsystem with low cost, high speed, reduced reagent requirement and precision control of liquid quantity and position.

The layers of interest are thin, usually with a thickness less than the wavelength of the surface wave. Moreover, it is common to have many different independent modes of propagation all confined to the surface region. This chapter formulates the equations governing the propagation of the Rayleigh wave in a medium consisting of a piezoelectric solid layer on a solid substrate, and the mechanism of the layer structure's effect on the wave mode propagation.

4.1 Elastic wave in an infinite half-space

A well-known mode of elastic energy propagation is the Rayleigh wave, which can exist on the free surface of a solid of infinite depth [6]. For simple isotropic materials the mechanical displacements in a Rayleigh wave are elliptical, lie in a plane containing the propagation direction normal to the surface, and decay in an exponential fashion to negligible values within a few wavelengths of the surface.

4.1.1 Wave equation

In the absence of forces and piezoelectric effects, the wave equation for the displacement in a perfectly elastic, homogeneous, anisotropic medium can be written as [7, 8]:

$$\rho \frac{\partial^2 u_j}{\partial t^2} = c_{ijkl} \frac{\partial^2 u_k}{\partial x_i \partial x_l} \quad (i, j, k, l = 1, 2, 3) \quad (4.1)$$

where u_j are the displacement components measured along the Cartesian axes x_j to which the elastic stiffness c_{ijkl} is referred, and the density of the medium is ρ .

If the medium is infinite in all directions, then the simplest solutions of the wave equation are plane waves, given by [9]:

$$u = A \exp[ik(l_i x_i - vt)] \quad (4.2)$$

with $A = i_i a_i$, where i_i is a unit vector along the x_i axis. The phase velocity v of the wave is measured along the propagation vector k , whose direction cosines are given by l_i .

The solution for the velocity and the displacement in the infinite-medium can be determined explicitly by substituting Eq. (4.2) into wave Eq. (4.1).

4.1.2 Surface wave

The coordinate system for the surface-wave is illustrated in Fig. 4.1, with x_3 as the outward normal to the traction-free surface of the medium which occupies the half-space $x_3 < 0$.

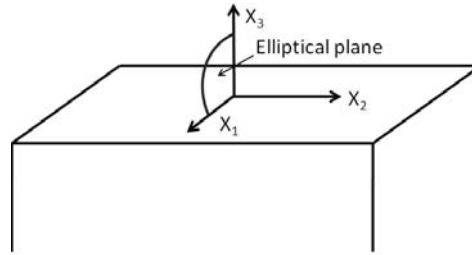


Figure 4.1 Coordinate system for the surface wave

Solutions of the equation show that the wave decays with the depth below the surface. The elliptical plane is the plane perpendicular to the free surface and contains the propagation vector (which is defined by its magnitude k). The solution must be such that the amplitudes of all the displacement components vanish as $x_3 \rightarrow -\infty$. Conceptually, the x_3 -dependence is regarded as part of the ‘amplitude’ of the term.

The displacements satisfy the wave equation consisting of a longitudinal component and a vertical component. The particle displacement at any depth is elliptical. The shape of the ellipse changes with depth because the relative magnitudes of u_3 and u_1 change with depth. The displacement of u_3 and u_1 are given in the expression below [10]:

$$u_1 = \bar{u}_1 \cos k(x_1 - vt) \quad u_3 = \bar{u}_3 \sin k(x_1 - vt) \quad (4.3)$$

Where \bar{u}_1 and \bar{u}_3 are the amplitudes of the longitudinal and vertical displacements in the expressions of the form of Eq.(4.3). There is a phase angle of 90° between the two displacement components. The variation with depth of \bar{u}_1 and \bar{u}_3 for a typical

isotropic material is shown in Fig. 4.2, which shows the decay of displacement amplitudes to negligible values a few wavelengths below the surface.

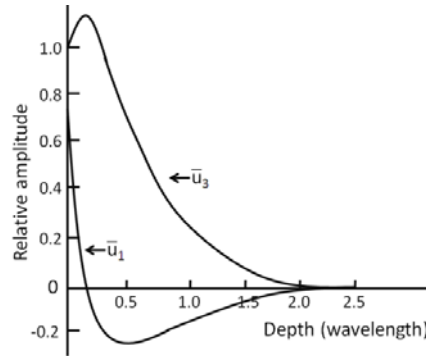


Figure 4.2 Typical SAW particle displacements in horizontal and vertical directions for waves propagating horizontally in an isotropic medium [6]

The coordinate system to be used throughout the discussion is illustrated in Fig. 4.3. It can be seen that the $z=0$ plane is the interface between the layer and the substrate, while the plane $z=h$ is the free surface. It is assumed that there is no variation of any of the displacement components in a direction parallel to the free surface and perpendicular to the direction of propagation. This direction of propagation defined by k ($|k| = 2\pi/\lambda$) will be taken as the x direction in Fig.4.1; thus the disturbance has a constant phase and amplitude for each component measured parallel to the y axis.

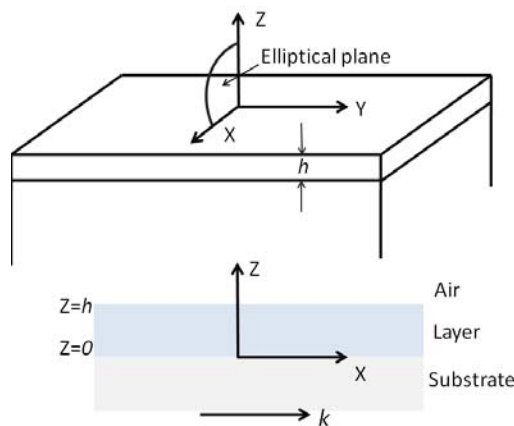


Figure 4.3 Coordinate system for propagation in thin layers

As mentioned above, the waves will decay with depth into the substrate and in general become of negligible amplitude a few wavelengths below the interface eventually. These waves must satisfy the appropriate wave equation in the layer and the substrate, as well as in the boundary conditions imposed by the interface and the free surface.

The elastic wave equations for the displacement are intercoupled to the potential Φ by the piezoelectric tensor e_{ijk} . Thus the particle displacements and the potential must satisfy in each medium the following equations [11, 12]

$$\begin{aligned} \rho \frac{\partial^2 u_j}{\partial t^2} - c_{ijkl} \frac{\partial^2 u_k}{\partial x_i \partial x_l} - e_{ijk} \frac{\partial^2 \phi}{\partial x_i \partial x_k} &= 0 \\ e_{ikl} \frac{\partial^2 u_k}{\partial x_i \partial x_l} - \varepsilon_{ijk} \frac{\partial^2 \phi}{\partial x_i \partial x_k} &= 0 \quad i, j, k, l = 1, 2, 3 \end{aligned} \quad (4.4)$$

in which ε_{ijk} is the dielectric permittivity tensor measured at constant strain. Each of the tensors in Eq. (4.4) refers to the coordinate system in Fig. 4.3.

4.2 Boundary conditions

In practice, any solid must have finite dimensions. The solutions of the above equations must satisfy boundary conditions that relate the mechanical and electrical variables at the boundary between two materials.

If the two materials are solids rigidly bounded to each other, there is no possibility of one sliding over the other; hence the material displacement is continuous at all points on the boundary [13].

The traction components of stress (T_{13} , T_{23} and T_{33}) must be continuous across the interface because of the intimate nature of the contact assumed between two materials. Since the surface is assumed to be mechanically stress-free, the three traction components of stress must vanish on it. The electrical boundary conditions for the

problem are provided by the continuity of the potential and of the normal component of electric displacement across both the interface and the free surface [14].

It is convenient to group these boundary conditions into three categories: the mechanical boundary conditions involving transverse displacements and facial stresses, the remaining electrical boundary conditions, and the elliptical plane mechanical boundary conditions. With the choice of coordinates of Fig. 4.3, the elliptical plane is any plane $y=\text{constant}$. Thus the twelve boundary conditions on the solutions will be ordered as follows:

(a) *Mechanical Transverse*

- (1) Continuity of the transverse displacement at the interface

$$u_2 = \tilde{u}_2 \quad \text{at } x_3 = 0$$

- (2) Continuity of the transverse shear stress at the interface

$$T_{32} = \tilde{T}_{32} \quad \text{at } x_3 = 0$$

- (3) Vanishing of the transverse shear stress at the free interface

$$\tilde{T}_{32} = 0 \quad \text{at } x_3 = 0$$

(b) *Electrical*

- (4) Continuity of the normal component of the electrical displacement at the interface

$$D_3 = \tilde{D}_3 \quad \text{at } x_3 = 0$$

- (5) Continuity of the potential at the interface

$$\phi = \tilde{\phi} \quad \text{at } x_3 = 0$$

- (6) Continuity of the normal component of the electrical displacement at the free surface

(c) *Mechanical Sagittal*

- (7) Continuity of the longitudinal particle displacement at the interface

$$u_1 = \tilde{u}_1 \quad \text{at } x_3 = 0$$

(8) Continuity of the vertical particle displacement at the interface

$$u_3 = \tilde{u}_3 \quad \text{at } x_3 = 0$$

(9) Continuity of the elliptical shear stress at the interface

$$T_{31} = \tilde{T}_{31} \quad \text{at } x_3 = 0$$

(10) Continuity of the vertical compressive stress at the interface

$$T_{33} = \tilde{T}_{33} \quad \text{at } x_3 = 0$$

(11) Vanishing of the elliptical shear stress at the free interface

$$T_{31} = 0 \quad \text{at } x_3 = h$$

(12) Vanishing of the vertical compressive stress at the free interface

$$T_{33} = 0 \quad \text{at } x_3 = h$$

The wave equations and the boundary conditions give two independent types of solutions; the solutions with transverse displacements only are called “Love mode”, whereas the solutions with elliptical displacements only will be called “Rayleigh modes”.

For these modes, in the isotropic case the elliptical mechanical displacements involved collapse the twelve general boundary condition equations to a simple set of six equations, which can be regarded as a six matrix.

4.3 Dispersion relations of the Rayleigh mode

For the layer-substrate combinations, the Rayleigh velocities of the substrate and layer have great influence on the Rayleigh mode that appears. The layer is said to “stiffen” the substrate if the presence of the layer increases the surface-wave velocity above that of the Rayleigh velocity on the substrate, whereas the layer is said to “load” the

substrate if the velocity of the free-surface Rayleigh mode on the substrate material is decreased by the presence of the layer [15, 16]

4.3.1 Rayleigh mode: $v_t > \tilde{v}_t$

A representative structure of materials that satisfy the “stiffening” conditions would consist of a polycrystalline layer of silicon on a substrate of polycrystalline zinc oxide. The parameters of silicon and ZnO are given in Table 4.1 [17].

Table 4.1 Material parameters for silicon and ZnO

	$C_{11} \times 10^{11}$ (N ² /m)	$C_{12} \times 10^{11}$ (N ² /m)	V_l (m/sec)	V_t (m/sec)	V_R (m/sec)
Silicon	1.865	0.535	8945	5341	4890
ZnO	2.043	1.113	6000	2831	2649

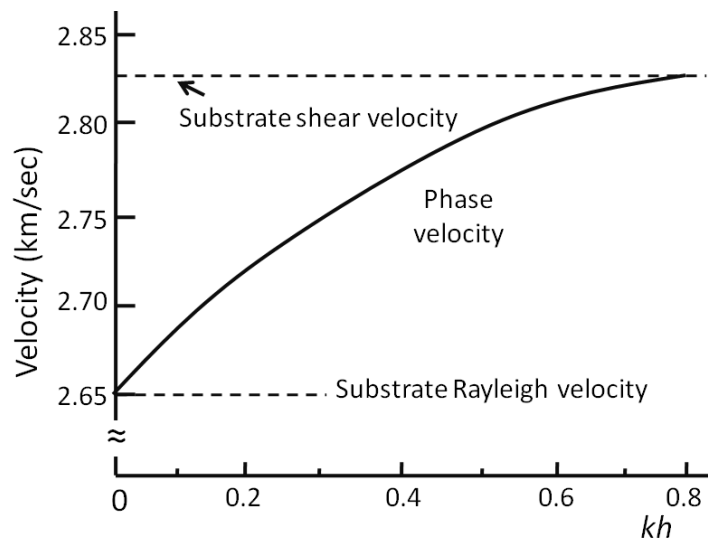


Figure 4.4 Rayleigh velocity for a silicon layer on a ZnO substrate [18]

The slope of the dispersion curve is positive for small values of kh , as shown in Fig. 4.4, and the velocity increases with kh . The dispersion curve for the structure starts for $kh=0$ at the substrate’s Rayleigh velocity and increases until the substrate shear velocity is reached at a particular value of kh . It should be noted that for the substrate

where $v_t > \tilde{v}_t$, only the Rayleigh mode can propagate, and only for a limited range of kh . The minimum velocity of this mode is the substrate Rayleigh velocity, and the maximum velocity is the substrate shear velocity. The velocity does not have a very wide range [20].

For $kh=0$ the solution is a Rayleigh wave on the free surface of the substrate and the displacements are of the form shown previously in Fig. 4.2. With the increase in kh , the displacement amplitudes in the substrate decay in the same form as for a free-surface case on the same material. Throughout the range of existence of this mode, the displacement amplitude varies monotonically over the layer thickness.

4.3.2 Rayleigh mode: $v_t < \tilde{v}_t$

Most applications are based on this structure – a piezoelectric thin film deposited on a substrate with higher velocity. It has been reported that ZnO on different substrates is a promising material system for applications in gas sensors and biosensors [19, 20, 21]. ZnO has been shown to have the potential to operate at high frequencies, and operation in the frequency range of GHz for ZnO SAW devices has been reported for ZnO grown on a diamond substrate [22]. The propagation velocity of the ZnO/diamond SAW devices can reach values of over 10,000 m/s thanks to the high Rayleigh velocity of the diamond substrate [24]. This section will explain how the substrate material with high velocity can enhance the velocity of the SAW device to values much higher than the that of the piezoelectric thin film.

Figure 4.5 shows the Rayleigh velocity of the ZnO deposited on the Si substrate. The ZnO layer loads the Si substrate and the velocity of the Rayleigh mode decreases with increasing kh . The dispersion curve for the first Rayleigh mode starts with negative slope at the Rayleigh velocity of the substrate – silicon, in this case – for $kh=0$. As kh increases, the velocity continues to decrease until, for layer thicknesses that are much

larger compared to the wavelength, $kh \gg 1$. It becomes asymptotic to the Rayleigh velocity \tilde{v}_R which is appropriate to a free surface of the layer material.

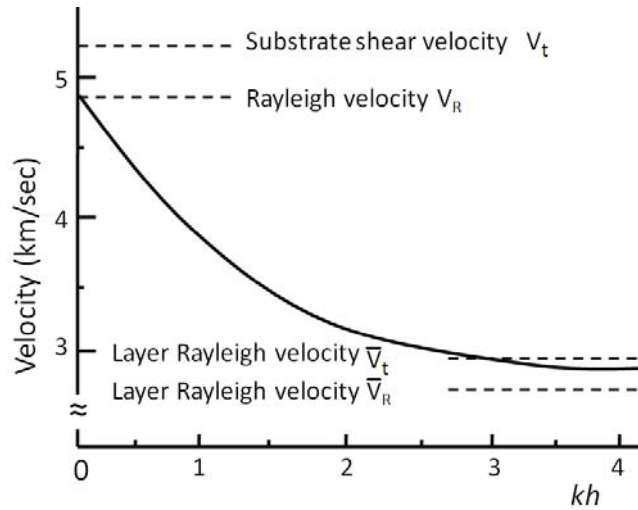


Figure 4.5 Velocity of the fundamental Rayleigh mode; ZnO on Silicon [20]

The significant feature of the case in which the layer substantially loads the substrate is the existence of an unlimited number of high-order modes of the Rayleigh waves, as illustrated in Fig.4.6. The higher-order Rayleigh modes all have a high-frequency asymptote equal to the layer shear velocity \tilde{v}_t , in contrast to the first mode, which has an asymptote equal to the Rayleigh velocity \tilde{v}_R of the layer material. Assuming that there is zero attenuation in the direction of propagation, each of the higher Rayleigh modes has a low-frequency cut off at which the velocity is equal to the substrate shear velocity [23].

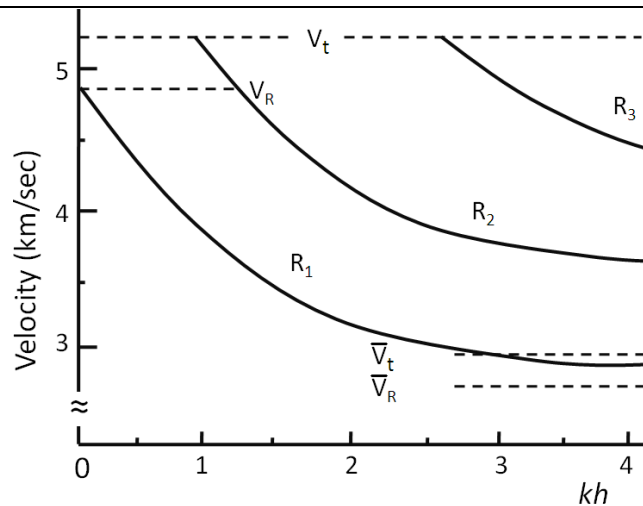


Figure 4.6 Velocity for the first three Rayleigh modes; ZnO layer on silicon

4.4 Conclusions

In summary, the Rayleigh waves in the layer-substrate combination have the following properties:

- There is a 90° phase difference between the horizontal and transverse displacements at each depth in both the layer and the substrate.
- The displacements in the substrate are of the same form as obtained for Rayleigh waves on a free surface.
- For the first Rayleigh mode at zero layer thickness, the case is the same as the one in which Rayleigh waves are on a free-surface. But for a non-zero layer thickness, the Rayleigh and higher modes have different numerical values of the displacement vs. depth curves for the substrate compared with a free surface of the same material. This is because the decay factors are affected by changing the frequency and layer thickness.
- By increasing layer thickness, more of the decay takes place within the layer materials.

- The second Rayleigh mode wave, the so-called Sezawa mode, requires a minimum layer thickness to propagate; that is, for a given layer thickness, there is a cut-off frequency below which the mode cannot propagate.

References

- ¹ J. G. Gualtieri, J. A. Kosinski and A. Ballato. "Piezoelectric material for SAW application". Ultrasonics Symposium, 1992. Proceedings. IEEE 1992 403.
- ² C. Ruppel and T. Fjeldly. "Advances in surface acoustic wave technology, systems and applications (Vol 1&2)". World Scientific publishing co. Pte. Ltd. 2000.
- ³ S.J. Pearton, D.P. Norton, K.Ip, Y.W. Heo and T. Steiner. "Recent progress in processing and properties of ZnO". Progress in Mater. Sci. 50 (2005) 293.
- ⁴ W. Water and S.Y. Chu. "Physical and structural properties of ZnO sputtered films". Mater. Lett. 55 (2002) 67.
- ⁵ H.W. Kim and N.H. Kim. "Influence of the substrate on the structural properties of sputter-deposited ZnO films". Phys. Stat. Sol.(a). 201 (2004) 235.
- ⁶ N. Tarasenko, P. Bohac, L. Jastrabik, D. Chvostova and A. Tarasenko. "Effect of roughness on the phase velocity of Rayleigh waves in GaAs crystals". Thin Solid Films. 491 (2005) 184.
- ⁷ H. M. Ledbetter and R. D. Kriz. "Elastic-wave surface in solids". Phys. Stat. Solid. (b) 114 (2) (2006) 475.
- ⁸ E. Urba and R. Miskinis. "Surface acoustic wave existence in anisotropic media - a review". Ultradarsas, Nr.4(37) 2000 29.
- ⁹ G. W. Farnell. "A review of propagation and electroacoustic coupling in layered structures". 1977 Ultrasonics Symposium Proceeding. IEEE 803.
- ¹⁰ S.M. Sze. Semiconductor Sensor. Wiley-interscience. New York. 1994.
- ¹¹ Y. Nakagawa, M. Yawara and S. Kakio. "Enhancement of photoelasticity assisted by surface acoustic wave and its application to the optical modulator". Electronics and Communicatiosn in Japan. Part 2 Vol. 84 (No. 5) (2001) 749.
- ¹² V. R. Velasco. "Study of interface and surface elastic wave in piezoelectric materials by using the surface green function matching (SGFM) method". Surface Science 128 (1983) 117.

- ¹³ S. Mikio, F. Shoji and N. Tooru. "Effects of boundary conditions on the characteristics of surface acoustic waves propagating along layered structures". IEIC Technical Report. 99 (318) (1999) 63.
- ¹⁴ W.P. Mason and R. N. Thurston. *Physical Acoustics. Principles and Methods*. Academic press. New York and London. 1970.
- ¹⁵ Z. Hadjoub, I. Beldi and A. Doghmane. "Origin and quantification of anomalous behaviour in velocity dispersion curves of stiffening layer/substrate configurations". *C. R. Ohysique* 8 (2007) 948.
- ¹⁶ J. A. Groetsch and R. E. Dessy. "A surface acoustic wave (SAW) probe for the thermomechanical characterization of selected polymer". *Journal of Applied Polymer Science*. 28 Issue 1 (1982) 161.
- ¹⁷ C. Campbell. *Surface acoustic wave devices and their signal processing applications*. Academic press, INC.
- ¹⁸ J. David and N. Cheeke. "Fundamental and applications of ultrasonic waves". CRC Press LLC. 2002
- ¹⁹ C. Pandis, N. Brilis, E. Bourithis, D. Tsamakis, H. Ali and S. Krishnamoorthy. "Low temperature hydrogen sensors based on Au nanoclusters and Schottky contacts on ZnO films deposited by pulsed laser deposition on Si and SiO₂ substrates". *IEEE Sens. J* 7(3) (2007) 448.
- ²⁰ D. Cui, H. Xu, X. Liu, M. Li and M. Jiang. "A noval method for improving the performance of ZnO gas sensors". *Sens Actuators B (Chem)* 114(1) (2006) 301.
- ²¹ Z. Liu, Y. Liu, H. Yang, Y. Yang, G. Shen and R. Yu. "A mediator-free tyrosinase biosensor based on ZnO sol-gel matrix". *Electroanalysis* 17(12) (2005) 1065.
- ²² H. Nakahata, S. Fujii, K. Higaki, A. Hachigo, H. Kitabayashi, S. Shikata and N. Fujimori. "Diamond-based surface acoustic wave devices". *Semicond Sci Technol*. 18(3) (2003) S96.

²³ S. Petroni, G. Tripoli, C. Combi, B. Vigna, M.D.Vittotio, M.T. Todaro, G. Epifani, R. Cingolani and A. Passaseo. “GaN-based surface acoustic wave filters for wireless communications”. *Superlattices and Microstructures*. 36 (2004) 825.

Chapter 5. Growth of Zinc Oxide Thin films

5.1 Introduction

The most common bulk piezoelectric materials that can be used for acoustic wave devices and associated sensors are *ST*-cut quartz (42.75° rotated *y* cut) and lithium niobate (LiNbO₃) which exhibit excellent temperature stability and a reasonably high electromechanical coupling coefficient, respectively. In addition, these materials also exhibit low acoustic transmission losses. However, these bulk piezoelectric materials are incompatible with conventional semiconductor materials used for microelectronics. Therefore, they cannot be integrated with electronics for control and signal processing. Furthermore, they have relatively slow surface acoustic wave propagation velocities (~4000m/s) [1]. Other potential materials for SAW applications are zinc oxide (ZnO) and aluminum nitride (AlN). ZnO and AlN thin films can be easily deposited on non-piezoelectric substrates such as silicon, with a potential for the integration with electronics for control and signal processing.

In this work, thin film ZnO is chosen as the piezoelectric material to develop thin film SAW devices and SAW-based microfluidics. ZnO has a high piezoelectric coefficient [2, 3], an excellent bonding on various substrate materials (such as silicon, silicon nitride and silicon dioxide) and it can be easily integrated into microelectromechanical (MEMS) devices. For comparison, LiNbO₃ bulk material is also used for fabricate SAW devices and SAW-based microfluidics.

A ZnO film has a hexagonal wurtzite structure and exhibits piezoelectric properties when its c-axis is perpendicular to the substrate [4, 5]. C-axis-oriented ZnO crystals are required to produce a SAW with displacement normal to the surface. In general, these films can be deposited by various methods such as spray pyrolysis [6, 7], the sol-gel process [8, 9], chemical vapour deposition [10], molecular beam deposition and RF magnetron sputtering [11, 12]. According to the literature, reactive sputtering is the most commonly used and preferred technique. Its advantages include easy control of film uniformity with preferred orientation, epitaxial growth at relatively low temperature, high deposition rate and good interfacial adhesion to the substrate [13, 14].

5.2 Sputtering

Zinc oxide thin films used in this study were deposited by RF magnetron sputtering. The process of sputtering involves the acceleration of ions of an inert gas, typically argon (Ar), through a potential gradient to the target material. The ions possess sufficient kinetic energy which exceeds the binding energy of the atoms on the target, and the atoms near the surface of the target are subsequently released into vacuum in vapour form. The atoms are deposited on the substrate and condense, resulting in film formation. The atoms then diffuse at the substrate surface.

This process is highly dependent on the deposition conditions. Specific sputtering processes can be characterized by the sputter yield, deposition rate, and secondary electron bombardment. The number of the target atoms released is referred to as the sputter yield. It is dependent on the binding energy of the atoms material as well as the mass of the ions used to bombard the target. The sputtering offers reasonable deposition rates for ZnO film deposition. The advantages of RF sputtering also include low pressure and low temperature.

5.2.1 Growth of the ZnO film

A 4-inch diameter zinc oxide target (99.99%) was used in a reactive plasma (argon and oxygen mixed). The ratio of argon (99.999% purity) and oxygen (99.999% purity) was controlled by electronic mass flow controllers. P-type silicon wafers were used as substrates. The substrates were ultrasonically cleaned in acetone and ethanol for 10 min, followed by rinsing in deionized (DI) water. They were dried with nitrogen gas before being introduced into the sputtering system.

The sputtering system was pumped down to a pressure of 2×10^{-6} mbar before a mixture of argon (30 sccm) and oxygen (10 sccm) was introduced into the chamber and RF power of 200 W at 13.56 MHz applied to the target. The Zn target was then pre-sputtered for 10 min to remove any contaminant from the target surface and stabilize the oxidation state of the target surface before the deposition process. The target-to-substrate distance was kept at 10 cm. The thickness, structural property and surface morphology were characterized by SEM and AFM respectively.

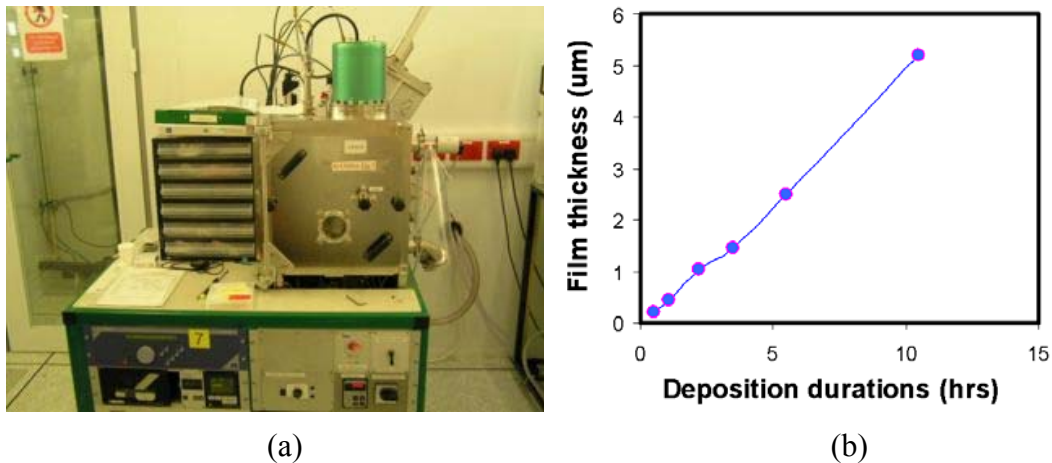


Figure 5.1(a) The photo of the sputtering system in the CAPE (b) The ZnO film thickness vs the duration of deposition time

5.2.2 Post-deposition annealing

Post-deposition rapid thermal annealing was carried out at 400°C for 10 min in different gas environments. The temperature of 400°C was sufficient for the annealing, and higher temperatures are unlikely to have any significantly improved effects. Post-deposition annealing has been proven to eliminate compressive film stress and improved crystallinity. The compressive film stress is attributed to a high atomic packing density and crystallographic defects on the grains and boundaries of the film. The crystalline phase contains less free energy than the defects and boundaries. Post-deposition annealing gives the thermal activation energy that is necessary for crystallites to increase in size, thus minimizing energy.

The ZnO/Si samples prepared by RF sputtering were first annealed for 10 min at 400°C in a nitrogen (N₂) gas environment. As most changes occur within the first 10 min of annealing, a short annealing period is sufficient to induce significant structural changes. During this period, the grain recovery took place.



Figure 5.2 The annealing machine in the clean room

5.3 Characterization of ZnO film

High-quality c-axis-oriented ZnO thin films were grown on Si substrates with thicknesses between 0.08 μm and 6.6 μm. Figure 5.2 shows the cross-sectional SEM images of different ZnO film thickness. Columnar grains of ZnO are shown which are perpendicular to the surface. This is because ZnO crystals typically grow as long

hexagonal rods along the c-axis, which results in columnar grain structures [15, 16]. C-axis ZnO structures are the preferred structures for SAW devices used for microfluidics, which normally require a wave displacement perpendicular to the surface.

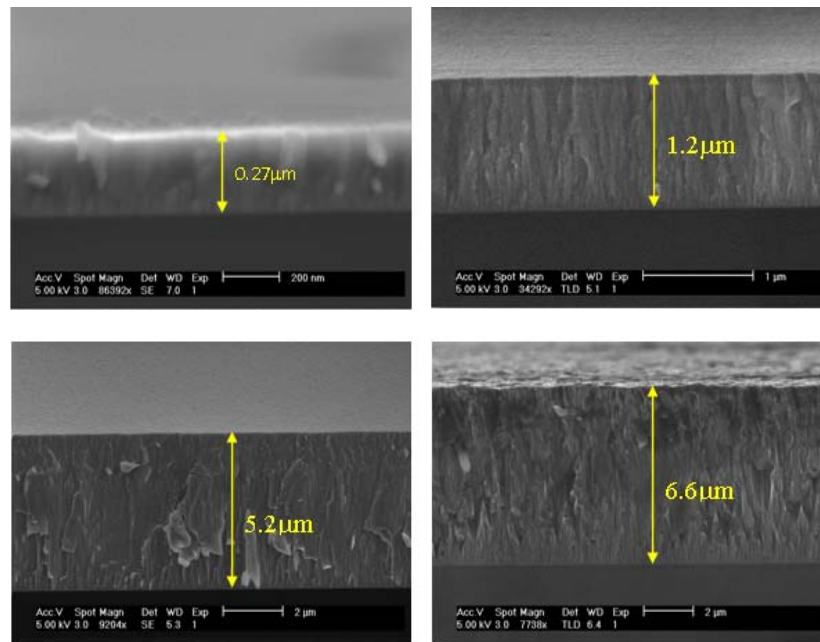


Figure 5.3 SEM images of the cross section of ZnO films of different thickness

There are numerous techniques that may be used to characterise the properties of ZnO films. These includes: various types of spectroscopy, x-ray diffraction, atomic force microscopy, and scanning electron microscopy, profilometry.

5.3.1 Crystallinity of the films

In order for ZnO films to be applied in SAW devices, the films must exhibit c-axis orientation. XRD, as a common technique that is used to study the crystallographic and structural properties of materials, was employed here. X-rays are passed through the sample and deflected in various directions due to the interactions with the electrons in the material. At certain incident angles, which are specific to individual material, the deflection is in phase and a strong signal is produced. As a result,

materials can be identified using this method.

All the deposited ZnO films exhibit the preferred c-axis orientation [17, 18]. Figure 5.4 shows the XRD spectrum of ZnO films of different thickness. All the films show a single peak at 34.2° which corresponds to the diffraction from the (002) plane of the ZnO. The full-width at half maximum values decreases with increasing thickness.

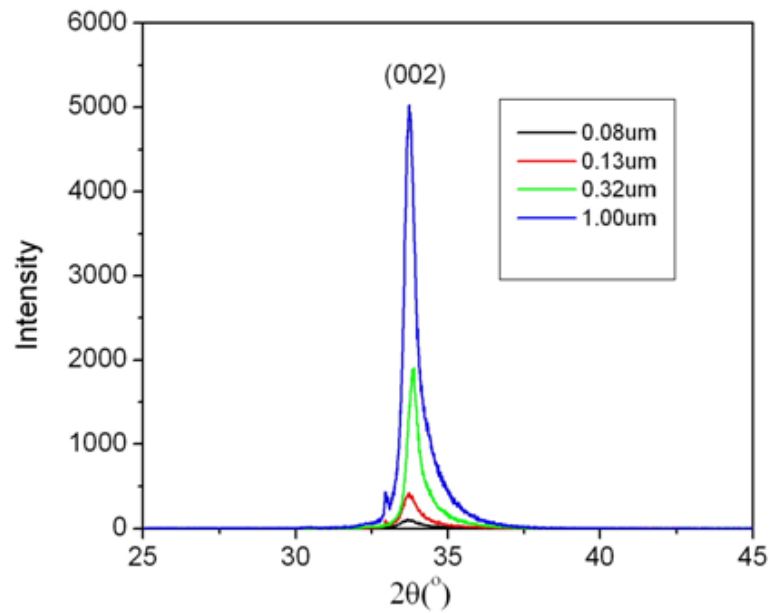


Figure 5.4 XRD spectrum of ZnO films of different thickness deposited at 200W with 25% of oxygen plasma

The Debye-Scherrer formula was used to calculate the crystallite sizes of the films, and it was found that they varied from 12 to 35 nanometers, depending on the deposition parameters. The average crystallite size can be estimated by the Debye-Scherrer formula [19, 20]:

$$D = \frac{K\lambda}{\beta \cos \theta} \quad (5.1)$$

where K is the shape factor of the average crystallite (expected to be 0.94), λ is the X-ray wavelength ($\lambda = 0.15406$ nm for a Cu target), β is the full width at half-maximum in radians, θ is the Bragg angle, and D is the mean crystallite

dimension normal to diffracting planes [21]. Nevertheless, this method is less accurate for determining crystallite sizes than the use of high resolution transmission electron microscopy.

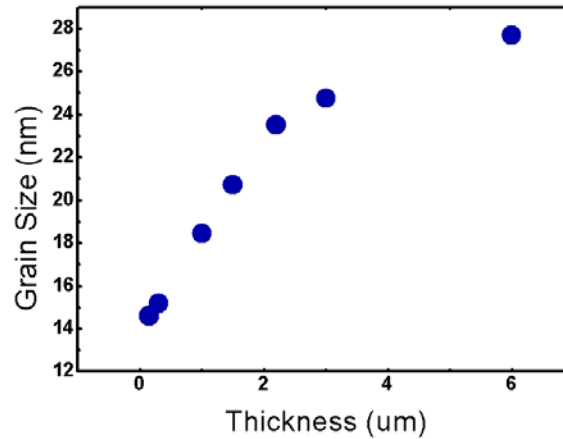


Figure 5.5 Grain size vs ZnO film thickness

5.3.2 Factors affecting the surface morphologies

When zinc oxide is used for SAW devices application, fine uniform grains and smooth surfaces are strongly desirable. This is because surface roughness hinders wave transmission and therefore increases the propagation loss [22, 23]. AFM characterization was carried out using a Veeco Explorer Scanning Probe Microscope in tapping mode to study the surface morphologies of the films grown [24, 25]. AFM is a high resolution version of scanning probe microscopy. The AFM uses a cantilever with a sharp micromachined tip located on one end to scan the surface of the samples. The cantilevers used were 110-140 μm long and oscillated at a frequency between 230 and 400 kHz. The advantages of AFM over SEM includes: small feature sizes down to one nanometer can be viewed, and they do not need to be operated in a high vacuum environment. Full three-dimensional surface profiles can also be produced or are also capable of being produced. This allows surface topological characteristics such as morphology and roughness to be studied. The disadvantages are that only small sample areas can be scanned and scan times are longer compared to SEM.

AFM was used to examine the surface morphology and surface roughness of the films. Three-dimensional AFM images of samples grown under different conditions are shown in Fig.5.6. It can be observed that the surface roughness values for these films were approximately in the order of tens of nanometers, indicating that the films were reasonably smooth. It is also observed that both grain sizes and roughness increase with thickness.

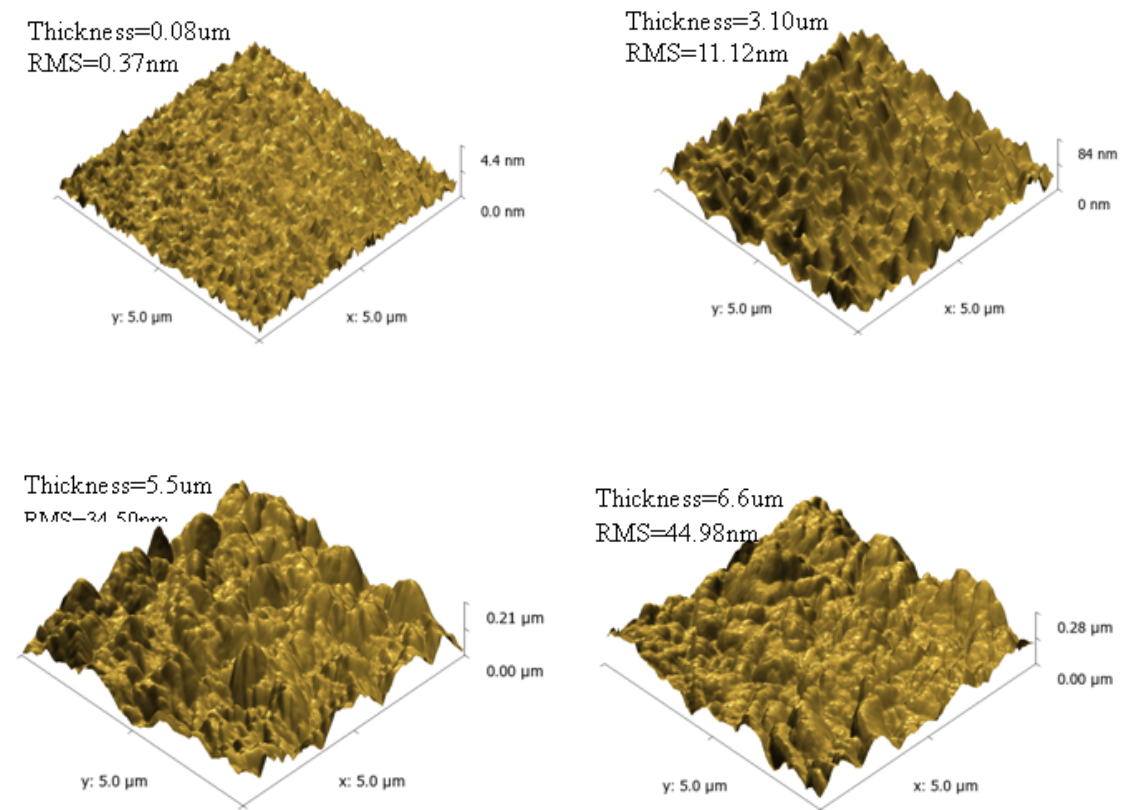


Figure 5.6 AFM images of surface morphologies for different thicknesses

AFM images were also used to estimate the size of the top-level crystal, which can be used to examine the variation in crystallite sizes.

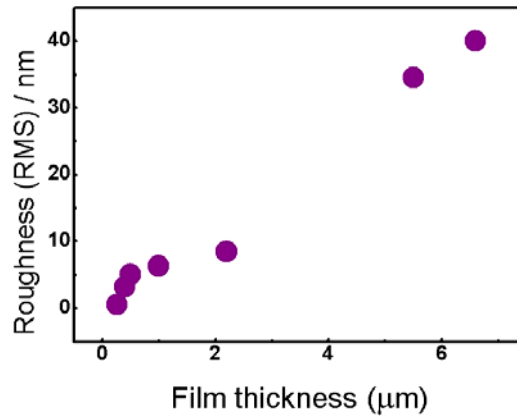


Figure 5.7 Surface roughness vs ZnO film thickness

5.3.3 Film stress

After the deposition, the films show significant compressive stress. Stress in ZnO films presents a major challenge to the SAW devices. It is also preferred that the film has small internal stress. Large internal stress is detrimental to the piezoelectric response of the film. The phase velocity of propagating waves is significantly affected when the substrate exhibits stress [26]. The travelling waves are dampened by film stress, and hence reduce the efficiency of the SAW devices. High stresses also cause the thin film to peel-off the substrate surface.

Stress in ZnO thin films is made up of both the intrinsic and thermal components. The thermal stress refers to the difference between deposition temperature and temperature of devices. The thermal stress is considered negligible in this study as the samples were sputtered at room temperature. The main cause of internal stress in ZnO film is compressive and is significantly greater than the thermal stress, values on the order of 1 GPa. The internal stress is compressive, which is the consequence of high energy ion bombardment on the film surface.

Sputtering-induced stress is calculated from the change in curvature of the substrate before and after sputtering. A Dektak profilometer tip applying a constant force of 15mg was used to scan the surface over 10 μm for substrate curvature measurements.

Thin films deposition on Si induces stress that causes the substrate to bend. Measuring the change in curvature of the center of the substrates before and after the deposition allows us to calculate sputtering-induced stress, based on Stoney's equation

$$\sigma = \frac{Et_s^2}{6t_f(1-\zeta)} \left(\frac{1}{R_f} - \frac{1}{R_o} \right) \quad (5.2)$$

where σ is the internal stress, ζ is Poisson's constant of Silicon ($\zeta_{Si}=0.25$), E is Young's Modulus ($E_{Si}=167\text{GPa}$), R_f and R_o are the radii for the final and initial curvature respectively, t_f is the film thickness and t_s is the substrate thickness (500 μm for a 4 inch Si wafer).

Annealing had major effects on the stress evolution of the films. All the deposited films exhibited significant compressive stresses on the order of a few GPa, whereas after post-deposition annealing, the stress is decreased significantly. This can be attributed to the fact that annealing reduces the number of defects by providing the thermal activation energy required for the defects states to move to a lower energy crystalline phase.

The effect of post-deposition annealing on film stress is also listed in Table 5.1. Compressive stresses are taken to be positive, while tensile stresses correspond to negative values. It is observed that the post annealing has little to no effect on the surface roughness.

Table 5.1 The internal stress before and after the annealing

ZnO film thickness	Post-deposition stress	Post-annealing stress
0.8 μm	1.18GPa	-0.257GPa
1.8 μm	1.34GPa	-0.412GPa
2.2 μm	1.31GPa	-0.475GPa
4 μm	1.53GPa	-0.79GPa
6.6 μm	2.29GPa	-0.91GPa

5.4 SAW device design

In addition, the spacing between IDTs is important, as the finger width determines the operation frequency of SAW devices. This section outlines the design of a variety of SAW devices based on LiNbO₃ and ZnO on Si substrates. For the single-electrode design, the finger width and spacing are set to be 1/4 wavelength λ of the surface wave for desired frequency. For devices with a spatial wavelength of 32 μm , the IDTs consist of 30 and 60 pairs of fingers, with an aperture of 4900 μm and a finger width of 8 μm . The delay line consists of a piezoelectric substrate on which two IDTs are implemented at a center to center distance of either 6720 μm (N=60 pairs of fingers) or 4160 μm (N=30 pairs of fingers) long.

The mask designed for 4-inch wafers was designed using *Autocad 2007* and then sent out for fabrication. The mask is a transparent plate with opaque regions that define the patterns to be transferred.

5.5 Fabrication of SAW devices

The fabrication of the SAW devices involved a standard photolithographic process. Photolithography, also known as optical lithography which refers to a process commonly used in semiconductor device fabrication to transfer a pattern from a mask. A photosensitive polymer known as photoresist is then deposited onto the substrate. Ultraviolet (UV) light is used to illuminate the sample. As a result, the exposed regions of photoresist undergo a physio-chemical change. A chemical developer then removes the portions of the photoresist that are exposed. Photolithography provides great control in accurate patterns in various shapes and sizes.

The photolithography process on the ZnO/Si and LiNbO₃ wafer are the same. However, the process on the ZnO/Si samples is more difficult, as the roughness of the ZnO/Si samples is much higher than that of the polished LiNbO₃ wafer. The greater

roughness makes the photoresist peel off easily. Therefore, special attention is paid when blowing the ZnO/Si samples by nitrogen (N₂).

5.5.1 Fabrication process flow outline

Cleaning procedures of substrates

Substrate cleaning is a basic step in any thin-film deposition process. In order to obtain high quality films, it is necessary to polish and clean the substrate thoroughly. In this study, we used 4-inch ZnO on Si (100) substrates or 128° Y-cut LiNbO₃ wafers. The main steps of substrate cleaning are as follows:

- (1) Ultrasonic oscillation in acetone for 3 min.
- (2) Clean with isopropyl alcohol and rinse in D.I. water.
- (3) Blow-dry with N₂ and a low-temperature dehydration bake at 80°C is done to remove the evaporator.

Photoresist patterned

- (1) Positive photoresist AZ5214 was spun (used in positive photoresist mode).
- (2) Speed of 600 RPMs for 6 seconds and then thinning spin at 4000 RPMs for 30 seconds.
- (3) The spin speeds result in a photoresist thickness of 1.2 – 1.5 μm.
- (4) Next, the wafer is placed on a hotplate and prebaked at 110° C for 5 minutes.
- (5) Using a dark field mask that exposes only the IDTs and contact pads, the wafer is exposed to ultraviolet (UV) light for 7 seconds on the contact aligner.
- (6) The sample is then soaked in AZ400K developer for approximately 20 seconds, then rinsed in DI water and N₂ dried.
- (7) Post-bake on hotplate at 120°C for 5 minutes.

Al Sputtering

- (1) Aluminium (Al) is deposited by sputtering on the surface using 90 watts (W) of forward power while minimizing the reflected power.
- (2) The standard cubic centimetres per minute (sccm) flow rate of Argon (Ar) is 20.
- (3) This sputter process results in a deposition rate of 1 nm/min while keeping the

surface from becoming overheated, leading to a 150 nm Al film.

- (4) This film thickness, h , is chosen because if the ratio of $h/\lambda < 1\%$ then the mass loading effects of the IDT are negligible.
- (5) The wavelengths, λ , used for this project were $32\ \mu\text{m}$ and $64\ \mu\text{m}$, so the ratio is clearly below the 1% threshold.
- (6) The wafer was subjected to ultrasound in a beaker of acetone for a few minutes until all of the photoresist was removed and the non-exposed area of Al was lifted off. Aluminium lift off using ultrasonic bath in acetone ultrasonic bath and rinse with isopropyl alcohol and D.I. water. Nitrogen-dry.
- (7) Bake on hotplate at 100°C for 60 seconds.

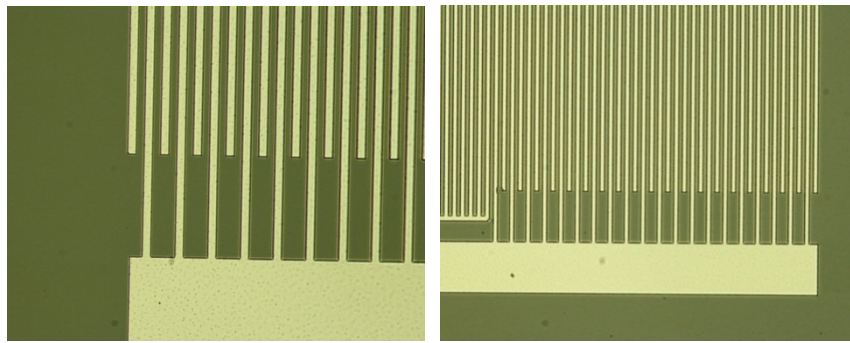


Figure 5.8 (a) The single-electrode IDT design with the finger width of $8\ \mu\text{m}$, $\lambda=32\ \mu\text{m}$
 (b) The IDT with reflectors, finger width of $16\ \mu\text{m}$, $\lambda=64\ \mu\text{m}$, $N=20$. Both on LiNbO_3

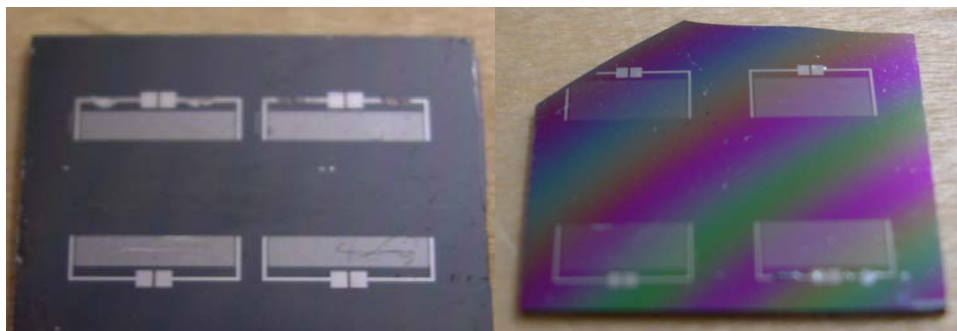


Figure 5.9 (a) SAW on $6.6\ \mu\text{m}$ ZnO, $\lambda=32\ \mu\text{m}$ $N=30$ (b) SAW on $1.2\ \mu\text{m}$ ZnO, $\lambda=64\ \mu\text{m}$
 $N=60$

5.6 Conclusions

This section contains details on fabrications of the SAW devices. Primarily, appropriate deposition parameters have been obtained to grow a good quality ZnO films for SAW device applications. ZnO films must have a c-axis-oriented crystalline structure and a smooth surface in order to be applied in the fabrication of SAW devices. Secondly, ZnO/Si devices of ZnO film thickness of 0.15 μm and 6.6 μm have been fabricated. The SAW devices with thin ZnO films have been proven to have lower surface roughness and poorer acoustic properties, while devices with large ZnO films will have better acoustic properties but higher surface roughness.

References

- ¹ C. Caliendo. "Acoustic method of investigating the material properties and humidity sensing behavior of polymer coated piezoelectric substrate". *J. Appl. Phys.* 100 (2006) 054508.
- ² G. Ferblantier, F. Maily, R. Al Asmar, A. Foucaran and F. Pascal-Delannoy. "Deposition of zinc oxide thin films for application in bulk acoustic wave resonator". *Sensors and Actuators A.* 122 (2005) 184.
- ³ H. Jaffe and D.A. Berlincourt. "Piezoelectric transducer materials". *Proceedings of the IEEE.* 53(10) (1965) 1372.
- ⁴ S.K. Kim, S. Y. Jeong and C. R. Cho. "Structural reconstruction of hexagonal to cubic ZnO films on Pt/Ti/SiO₂/Si substrate by annealing". *Appl. Phys. Lett.* 82(4) (2003) 562.
- ⁵ A. Cimpoiasu, N.M Van der pers, T. H. De Keyser, A. Venema and M. J. Vellekoop. "Stress control of piezoelectric ZnO films on silicon substrate". *Smart Material Structures.* 5 (1996) 744.
- ⁶ S. A. Studenikin, N. Golego and M. Cocivera. "Fabrication of green and orange photoluminescent, undoped ZnO films using spray pyrolysis". *J. Appl. Phys.* 84 (1998) 2287.
- ⁷ J. M. Bian, X. M. Li, X. D. Gao, W. D. Yu and L. D. Chen. "Deposition and electrical properties of N-In codoped p-type ZnO films by ultrasonic spray pyrolysis". *Appl. Phys. Lett.* 84 (2004) 541.
- ⁸ J. Zhai, L. Zhang and X. Yao. "The dielectric properties and optical propagation loss of c-axis oriented ZnO thin films deposited by sol-gel process". *Ceramics International.* 26 (Issue 8) (2000) 883.
- ⁹ Y. Natsume and H. Sakata. "Zinc oxide films prepared by sol-gel spin-coating". *Thin Solid Films*". 372 (Issue 1-2) (2000) 30.
- ¹⁰ C. R. Gorla, N. W. Emanetoglu, S. Liang, W. E. Mayo, Y. Lu, M. Wraback and H.

Shen. “Structural, optical, and surface acoustic wave properties of epitaxial ZnO films grown on (011-bar 2) sapphire by metalorganic chemical vapor deposition”. *J. Appl. Phys.* 85 (1999) 2959.

¹¹ P. F. Carcia, R. S. McLean, M. H. Reilly and G. Nunes. Jr. “Transparent ZnO thin-film transistor fabricated by RF magnetron sputtering”. *Appl. Phys. Lett.* 82 (Issue 7) (2003) 1117.

¹² K.B. Sundaram and A. Khan. “Characterization and optimization of zinc oxide films by RF magnetron sputtering”. *Thin Solid Films.* 295 (Issue 1-2) (1997) 87.

¹³ M.J. Vellekoop, G.W. Lubking, P.M. Sarro and A. Venema. “Integrated-circuit-compatible design and technology of acoustic-wave-based microsensors”. *Sens. Actuators A.* 44 (1994) 249.

¹⁴ S. Guha and N.A. Bojarczuk, “Multicolored light emitters on silicon substrates”. *Appl. Phys. Lett.* 73(1998) 1487.

¹⁵ K.B. Sundaram, and B.K. Garside. “Properties of ZnO films reactively RE sputtered using a Zn target”. *J. Phys. D: Appl. Phys.* 17 (1984) 147.

¹⁶ K.B. Sundaram, and A. Khan. “Characterization and optimization of zinc oxide films by r.f. magnetron sputtering”. *Thin Solid Films.* 295 (1997) 87.

¹⁷ C. Hou, K. Huang, Z. Gao and X. Li. “Structural and optical properties of ZnO films with different thicknesses grown on sapphire by MOCVD”. *Chem. Res. Chinese U.* 22(5) 2006 552.

¹⁸ T. T. Wu and W. S. Wang. “An experimental study on ZnO/sapphire layered surface acoustic wave device”. *J. Appl. Phys.* 96 (2004) 5249.

¹⁹ K. Bobzin, E. Lugscheider, M. Maes, P. Immich and S. Bolz. “Grain size evaluation of pulsed TiAlN nanocomposite coatings for cutting tools”. *Thin Solid Films* 515 (2007) 3681.

²⁰ T. T. Wu and W. S. Wang. “An experimental study on ZnO/sapphire layered surface acoustic wave device”. *J. Appl. Phys.* 96 (2004) 5249.

- ²¹ M.K. Puchert, P.Y. Timbrell and R.N. Lamb. "Thickness-dependent stress in sputtered carbon films". *J. Vac. Sci. Technol. A.* 14 (4), (1996) 2220.
- ²² K. Uehara, Y. Aota, S. Kameda, H. Nakase and K. Tsubouchi. "Low propagation loss of atomically-flat surface AlN low dislocation density for 5-GHz band SAW devices". *IEEE Ultrasonics Symposium 2005* 455.
- ²³ M. B. Assouar, M. El Hakiki, O. Elmazria, P. Alnot and C. Tiusan. "Synthesis and microstructural characterisation of reactive RF magnetron sputtering AlN films for surface acoustic wave filters". *Diamond and related materials.* 12 (2004) 1111.
- ²⁴ G. Binning and C. F. Quate. "Atomic force microscope". *Physical Review Letters.* 56(9) (1986) 930.
- ²⁵ S. R. Manalis, S. C. Minne and C. F. Quate. "Atomic force microscopy for high speed imaging using cantilever with an integrated actuator and sensor". *Appl. Phys. Lett.* 68 (5) (1996) 871.
- ²⁶ S. Sathisha, T. J. Morana, R. W. Martinb and R. Reibelb. "Residual stress measurement with focused acoustic waves and direct comparison with X-ray diffraction stress measurements". *Mater. Sci. and Engin. A.* 399 (Issue 1-2) (2005) 84.

Chapter 6. Signal Measurement on LiNbO₃ and ZnO/Si SAW

Devices based on SAWs, which allow transduction between electrical and acoustic energies, have been constructed in a number of configurations. The largest current markets for SAW applications are in cell phones as filters, and in sensor applications. As the global market for mobile phones grows, the demand on SAW devices becomes considerable [1]. Surface acoustic waves are used in electronics as transformers, oscillators, filters and sensor applications.

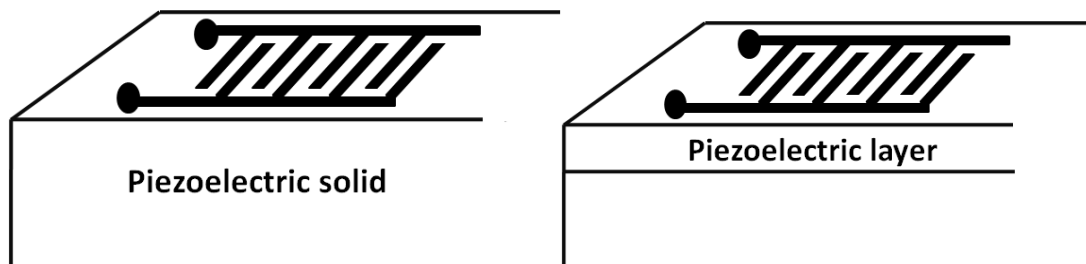


Figure 6.1 Surface waves in monocrystal or an isotropic solid, by means of an intermediate piezoelectric layer

Two types of SAW devices are discussed in this study, as illustrated in Fig. 6.1. The substrate of both devices is assumed to be a solid propagating medium. It may be homogeneous in conjunction with isotropic, or anisotropic, or it may be a layer structure such as a film on a substrate. In the case of crystals, the crystallographic cut is chosen according to the type of wave [2]. The velocity of the wave is constant, regardless of the frequency. For a layer medium, the frequency dependence of wave speeds is different for the film and substrate.

There are two general categories of SAW device: single port and two-port. In single-port devices, the port serves as both the input and output ports. In two-port devices, one port is used as the input port and the other as the output port, and they are typically interchangeable. The input signal generates a signal travelling to the output port. Delay lines are always used as two-port devices giving two IDTs deposited on a piezoelectric substrate.

The final dimensions of SAW devices are a function of the desired operating frequency. As previously discussed, the finger width and spacing required for a given f_r value can be calculated from the propagation velocity of the acoustic mode employed: $f_r = v/\lambda$. The wavelength λ is defined by the spatial periodicity of the device, the width d of the finger of the IDT and the distance between fingers.

The samples were mounted on a PCB board with double-sided tape, and contact pads were connected by wire with silver paste. The samples were initially attached to an Agilent Technologies E5061A ENA Series Network Analyzer. The network analyzer is used to sweep across a range of signals in the region of the oscillation frequency to find the exact resonant frequencies of the SAW devices.

6.1 SAW signal on LiNbO₃ substrates

As mentioned previously, a thin Al layer of 150 nm, which is less than 0.5% of the wavelength (λ) of the SAW, is used for the IDT. 20, 30, 40 and 60 pairs of fingers and an aperture of 4900 μm were fabricated on LiNbO₃ substrates for SAW devices. The spatial periodicities that define the operational wavelengths are 32 μm and 64 μm , respectively.

On a single-port SAW device, the signal is measured from the same port that creates the oscillating wave across the piezoelectric medium. As a result, we measure the

reflected signal, which refers to a signal input to one of the ports, and the signal is reflected and collected from the same input port. The parameters of all the LiNbO₃ samplers are listed in Table 6.1.

Table 6.1 Designed parameters of the devices

Sample	Wavelength λ	Finger pairs N	Metallization ratio η	Delay line L
A	32 μm	30	~ 0.5	
B	64 μm	20	~ 0.5	
C	32 μm	60	~ 0.5	
D	64 μm	40	~ 0.5	
E	32 μm	60	~ 0.47	4.8mm
F	32 μm	60	~ 0.49	20mm
G	32 μm	30	~ 0.43	3.2mm
H	64 μm	20	~ 0.45	4.8mm

Figure 6.2(a) and (b) show the reflection spectra of SAW devices A & B with $\lambda=32$ and 64 μm respectively. Both samples have single-electrode IDTs. The downward peak corresponds to the Rayleigh mode wave with resonant frequencies of 62.4 MHz and 124.86 MHz for devices with wavelength of 64 and 32 μm respectively. Both showed an acoustic velocity of 3993-3995 m/s, in great agreement with that of the LiNbO₃ substrate reported in Ref.[3, 4].

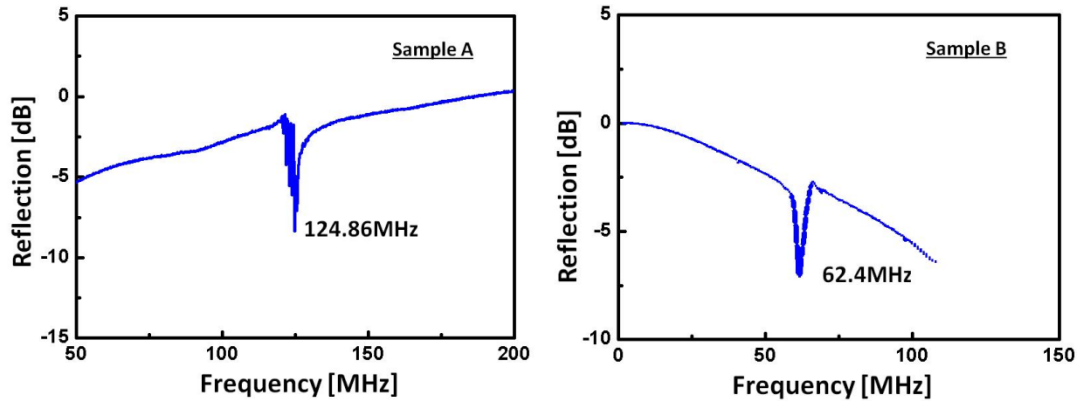


Figure 6.2(a) The reflection of the LiNbO₃ Sample A, $\lambda = 32\mu\text{m}$ and $N=30$. (b) The reflection of the LiNbO₃ Sample B, $\lambda = 64\mu\text{m}$ and $N=20$

On dual-port devices the signal is measured on the other end of the SAW element. Dual-port devices are commonly used in oscillator circuits, such as oscillator loops, propagation measurement set-ups and phase-locked loops. In two-port devices, the delay line consisting of two symmetric IDTs, one port is used as the input port and the other as the output port. The wave travels through the substrate and will reach the second IDT on the other side where a voltage can be measured. Since the two ports are typically interchangeable, the analysis of the scattering parameters on both configurations is: $S_{11}=S_{22}$ (reflection) and $S_{21}=S_{12}$ (transmission) [5]. The transmitted signal refers to output signal from the opposite IDT.

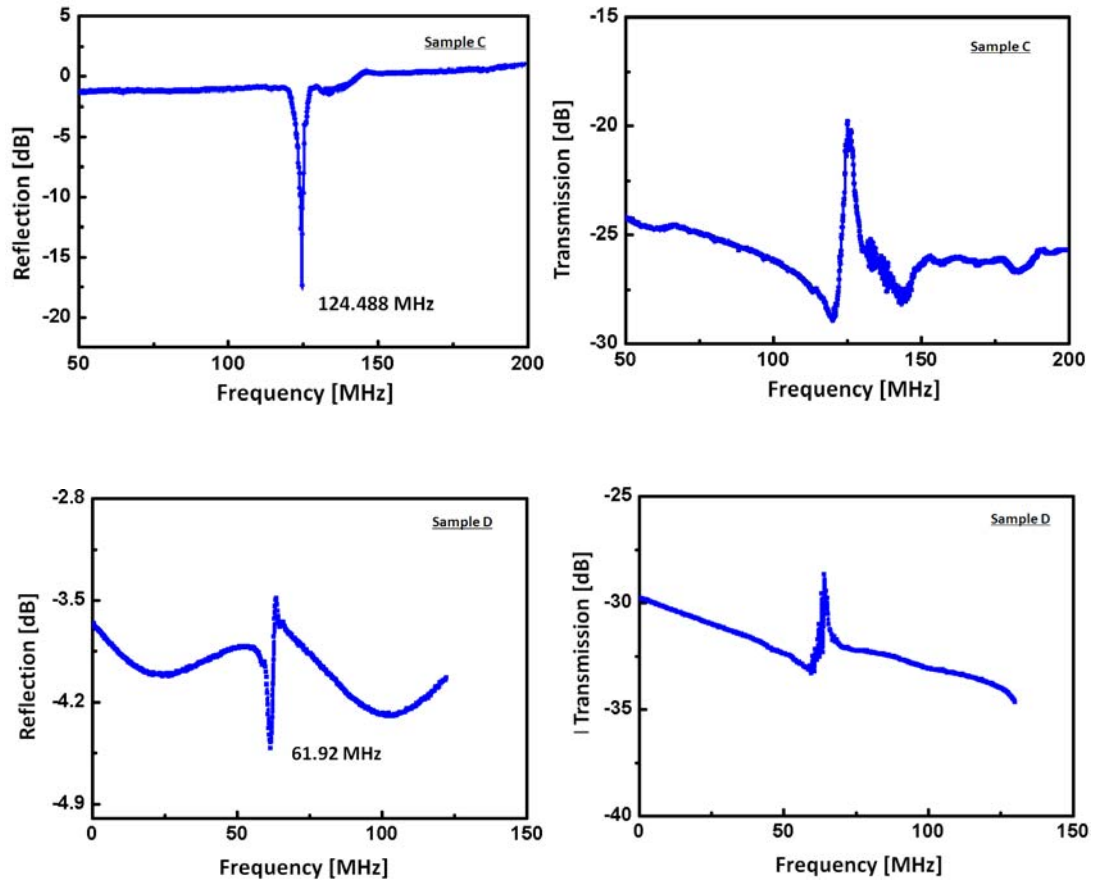


Figure 6.3(a) The reflection and transmission signal for LiNbO₃ Sample C
and (b) The reflection and transmission signal for LiNbO₃ Sample D

The figures above are the reflection and transmission signals measured by the network analyzer. The operational frequency of the Rayleigh wave is determined by the properties of the substrate materials and the periodicity of the metal fingers of the IDT, which is limited by photolithography. The velocity of the Rayleigh wave is constant, and can be calculated by the measured frequency and the designed wavelength.

6.1.2 Harmonic mode on LiNbO₃ substrates

Thus far, all the devices considered operated at their fundamental frequencies. This section will depart from this restriction and consider the operation of SAW transducers at harmonic frequencies.

SAW devices can be made to operate at harmonic frequencies. It has been demonstrated that they can be made to operate efficiently at least up to the eleventh harmonic. The use of harmonic waves is attractive for three reasons:

Firstly, there is a fabrication cost advantage, as it enables gigahertz SAW IDTs to be fabricated without submicron lithographic techniques or resorting to the use of costly electron-beam lithography.

Secondly, the use of harmonic techniques can be beneficial in situations where the performance of the SAW at its fundamental frequency is degraded by bulk wave interference.

Finally, as the sensitivity is directly proportional to the operating frequency, high-order harmonic waves are often utilized in high-frequency applications such as telecommunications and biosensors.

The Rayleigh wave travelling in the LiNbO₃ substrates reported above is also called the first-mode wave. In addition to the fundamental Rayleigh wave, higher-order harmonic waves, typically the odd mode harmonic waves are also generated by the IDT simultaneously in SAW devices.

Figure 6.4 shows the reflection spectra of SAW devices with $\lambda = 32$ and $64\mu\text{m}$, respectively. The first peak corresponds to the fundamental mode wave with the resonant frequencies of 62 MHz and 124 MHz for devices with wavelength of 64 and 32 μm respectively. A higher odd-mode harmonic wave also appears. It was observed that when the metallization is less than 0.6, the Rayleigh and third harmonic mode waves appear simultaneously, and the third mode wave disappears when η ($\eta = \text{metallised surface/total surface}$) shown in Fig.6.5 [6] > 0.6 . It is known that the appearance of high-mode harmonic waves in the SAW is determined by the

metallization ratio, η , which is in agreement with our observation. The resonant frequency (f_r) of a SAW device is determined by the phase velocity (v) of the acoustic wave in the substrate and the wavelength (λ): $v = f_r * \lambda$. The higher harmonic mode wave has the same phase velocity, and its resonant frequency f_n is determined by a similar equation: $v = f_n * \rho$, where $\rho = \lambda/n$, where ρ is the spatial wavelength of the harmonic wave and n is the order of the harmonic wave considered [7]. Generally, the high-order resonant frequency is simply correlated by $f_n = n * f_r$.

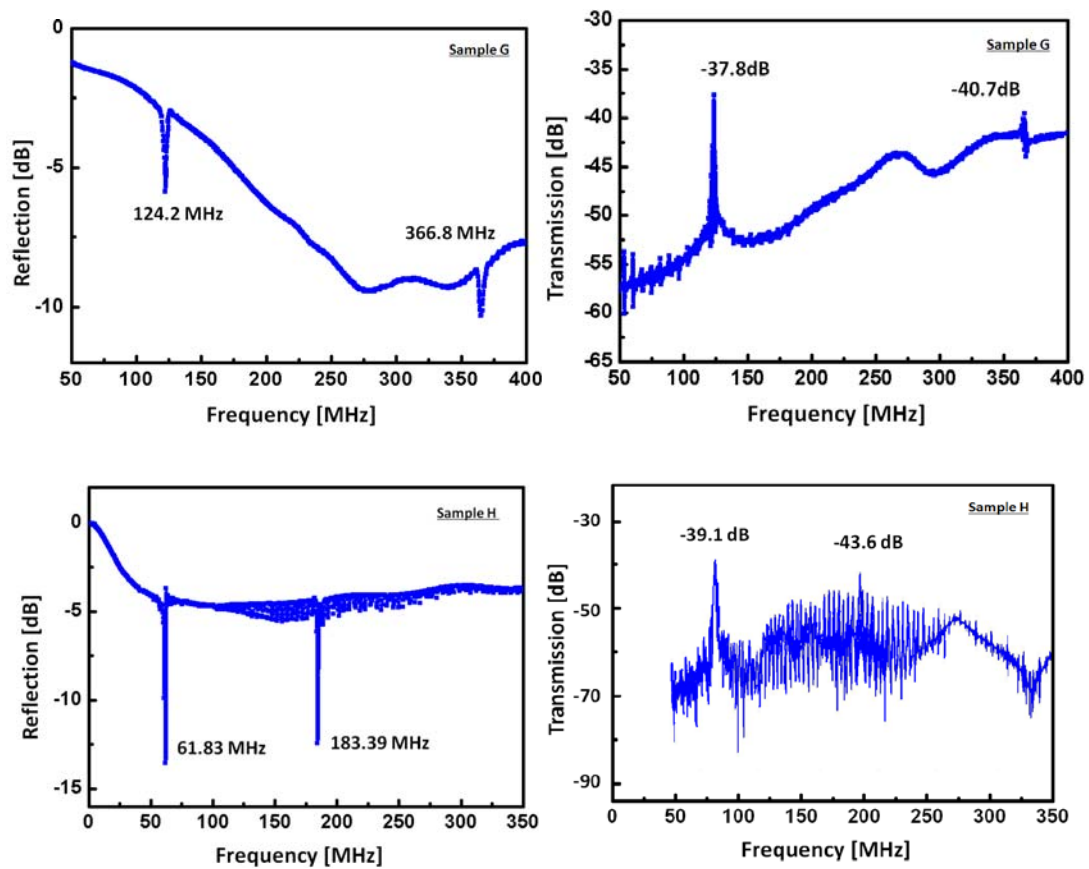


Figure 6.4(a) The reflection and transmission signal for LiNbO₃ Sample G and (b) The reflection and transmission signal for LiNbO₃ Sample H

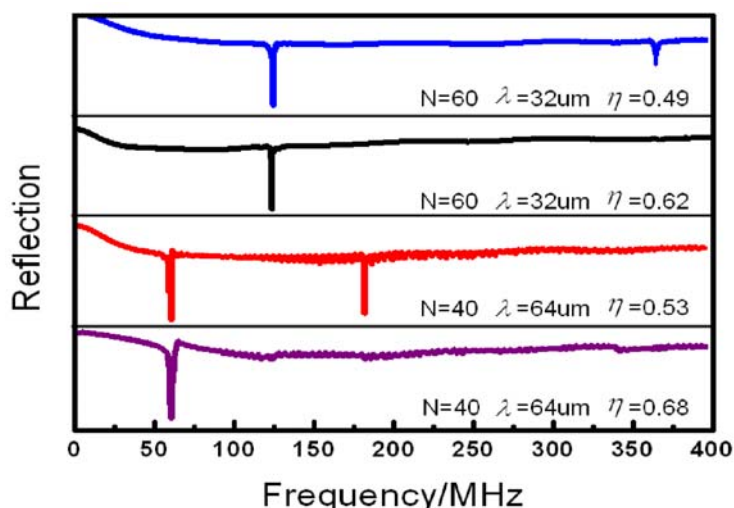


Figure 6.5 The reflection of SAW devices with various configurations with the fundamental and harmonic modes

It is clear from Fig.6.4 that the resonant frequencies of the third harmonic waves are three times those of the Rayleigh-mode wave for both devices ($\lambda=32$ and $64\mu\text{m}$). It is also clear that the Rayleigh wave is stronger in amplitude than the third-mode wave.

Insertion loss was measured between transducer pairs with different separations, and from these measurements, the SAW propagation loss could be determined as a function of frequency. In order to measure the propagation loss, SAW devices with different IDT distances were fabricated, one with $L=4800\ \mu\text{m}$, and the other with $L=20000\ \mu\text{m}$ (L is the length of delay line between two IDTs). The difference in travelling distance is $\Delta L=15200\ \mu\text{m}$, 475 times the fundamental wavelength λ . The attenuation of the acoustic wave in the LiNbO₃ substrate can be determined by measuring the maximum of the transmission signal S_{21} , (scattering parameters $S_{21}=S_{12}$) on delay lines using the following formula:

$$\alpha = \Delta S_{21} / \Delta L \quad (6.1)$$

The attenuation is often expressed as a function of wavelength α^λ in dB/ λ [8, 9], i.e. the propagation loss is referred to the operating wavelength. $\Delta S_{21}=7.3\text{dB}$ was obtained

from the experimental measurements for the fundamental mode shown in Fig.6.6. The propagation loss is $\alpha' = 1.54 \times 10^{-2}$ dB/ λ .

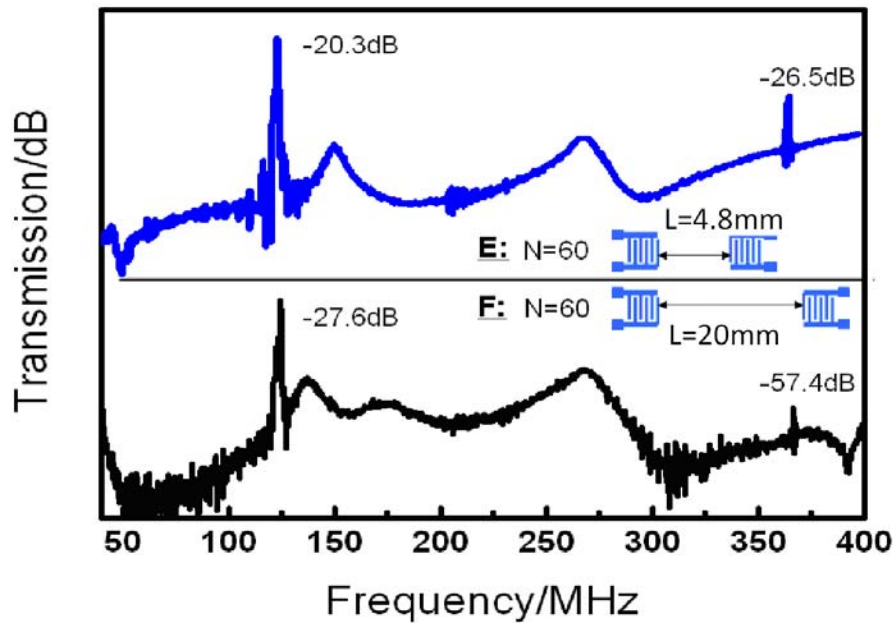


Figure 6.6 The transmission of SAW devices with different delay line, $\lambda=32\mu\text{m}$

The transmission of the 4.8mm and 20mm delay lines is shown in Fig.6.6. For the third harmonic mode, $\Delta S'_{21}=30.9$ dB is much higher than that found in the fundamental mode. The main reason behind this is that the spatial wavelength ρ is $\lambda/3$. Although the propagation path length is the same, ΔL is 1475 times the spatial wavelength of the third harmonic wave. Similarly, the propagation loss is calculated to be 2.2×10^{-2} dB/ ρ .

The above analysis has shown clearly that the propagation loss of the third-mode harmonic wave is higher than that of the fundamental-mode wave, and will be even higher for the 5th- and 7th-mode harmonics. SAW devices operating at higher frequencies through higher mode harmonics are attractive for high-frequency telecommunication and sensing applications. Nevertheless, their applications in these areas are restricted by their increased propagation loss.

The parameters of all the devices are listed in Table 6.1. All the devices use single-electrode IDT, with the same aperture of 4900 μm . The measured parameters are listed in Table 6.2.

Table 6.2 The performances of the sample A-H

Sample	Frequency f_o	Velocity	Reflection amplitude	Transmission
A	124.86MHz	3995.3m/s	6.7dB	
B	62.4MHz	3993.6m/s	4.7dB	
C	124.48MHz	3983.6m/s	16dB	-19.8dB
D	61.93MHz	3963.5m/s	7.5dB	-27.2dB
E	124.3MHz	3963.5m/s	9.8dB	-20.3dB
	367.3MHz	3917.9m/s	4.2dB	-26.5dB
F	124.33MHz	3978.6m/s	11.3dB	-27.6dB
	367.33MHz	3918.2m/s	3.0dB	-57.4dB
G	124.2MHz	3974.4m/s	4dB	-37.8dB
	366.8MHz	3912.5m/s	1.4dB	-40.7dB
H	61.83MHz	3957.1m/s	8.8dB	-39.1dB
	184.39MHz	3933.7m/s	7.8dB	-43.6dB

6.1.3 Temperature shift

Even relatively small temperature shifts could have dramatic effects on the behaviour and properties of a SAW device. Heat changes the density of material, and thus the velocity of a wave travelling in it. The sensitivity of resonator material to temperature shifts is known as the temperature coefficient of the material.

To determine the temperature coefficient near room temperature and identify the influence of the temperature on the measurement results, the sample holder was put on a hot plate and the samples were measured at room temperature, 40°, 50°, 60° and

70°. Measurements are taken at least several minutes after the temperature has reached and then remain stable. We assume that room temperature is 23°C for all samples.

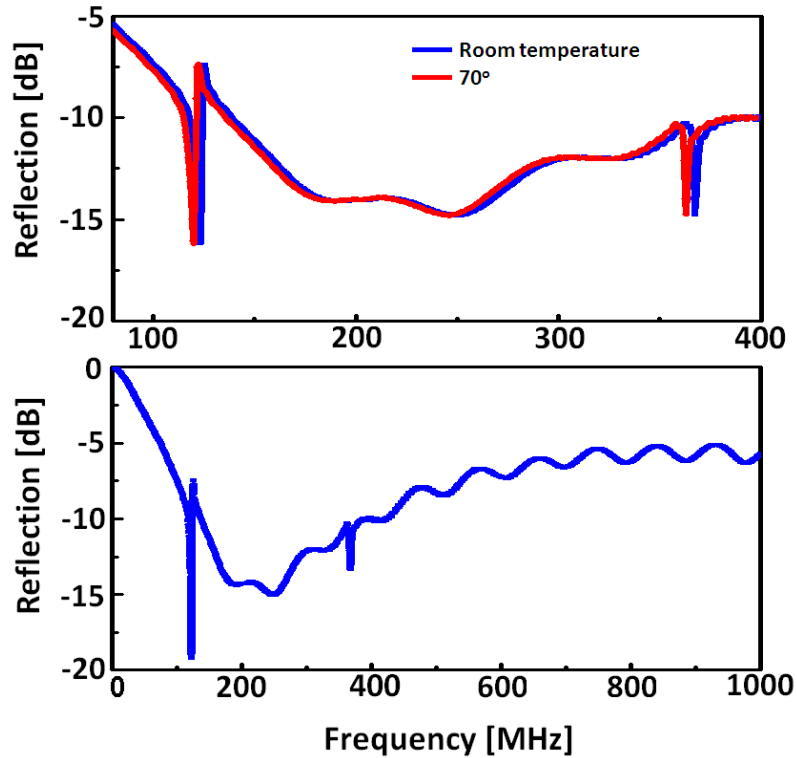


Figure 6.7 Frequency shift with increasing temperature and the reflection response up to 1000MHz

Figure 6.7 shows the reflection signals obtained at room temperature and at 70 °C. It can be easily seen that increasing the temperature decreases the resonant frequency. This change is mainly because of the expansion or contraction of the base material, which results in a change of acoustic path length and also IDT finger spacing.

Temperature coefficient of the delay

The effect of temperature on the SAW propagation characteristics is typically characterized in terms of the TCD (TCD is the temperature coefficient of the delay) given by [10, 11, 12]

$$\alpha_T = \frac{1}{\tau} \frac{d\tau}{dT} = \frac{1}{L} \frac{dL}{dT} - \frac{1}{v} \frac{dv}{dT} \quad (6.2)$$

where $\tau = L/v$ is the time delay between the input and output IDTs separated by a distance L , v is the SAW phase velocity, and T is the substrate temperature. The coefficient α_T expressed in units of $\text{ppm}^\circ\text{C}^{-1}$ is independent of the transducer separation L . It is essential that α_T be as small as possible for fabricating devices with good temperature stability.

The first term in the equation gives the change in TCD due to thermal expansion or contraction of the substrate material along the SAW propagation direction. The second term relates to the velocity shift due to the changes in temperature. In the literature -see, for example, Slobodnilor Jakoby & Yoshino [13,14] – the temperature coefficient of the frequency (TCF) is defined as

$$\frac{1}{f} \frac{\partial f}{\partial T} = \frac{v_g}{v} \left(\frac{1}{v} \frac{\partial v}{\partial T} - \frac{1}{L} \frac{\partial L}{\partial T} \right) \quad (6.3)$$

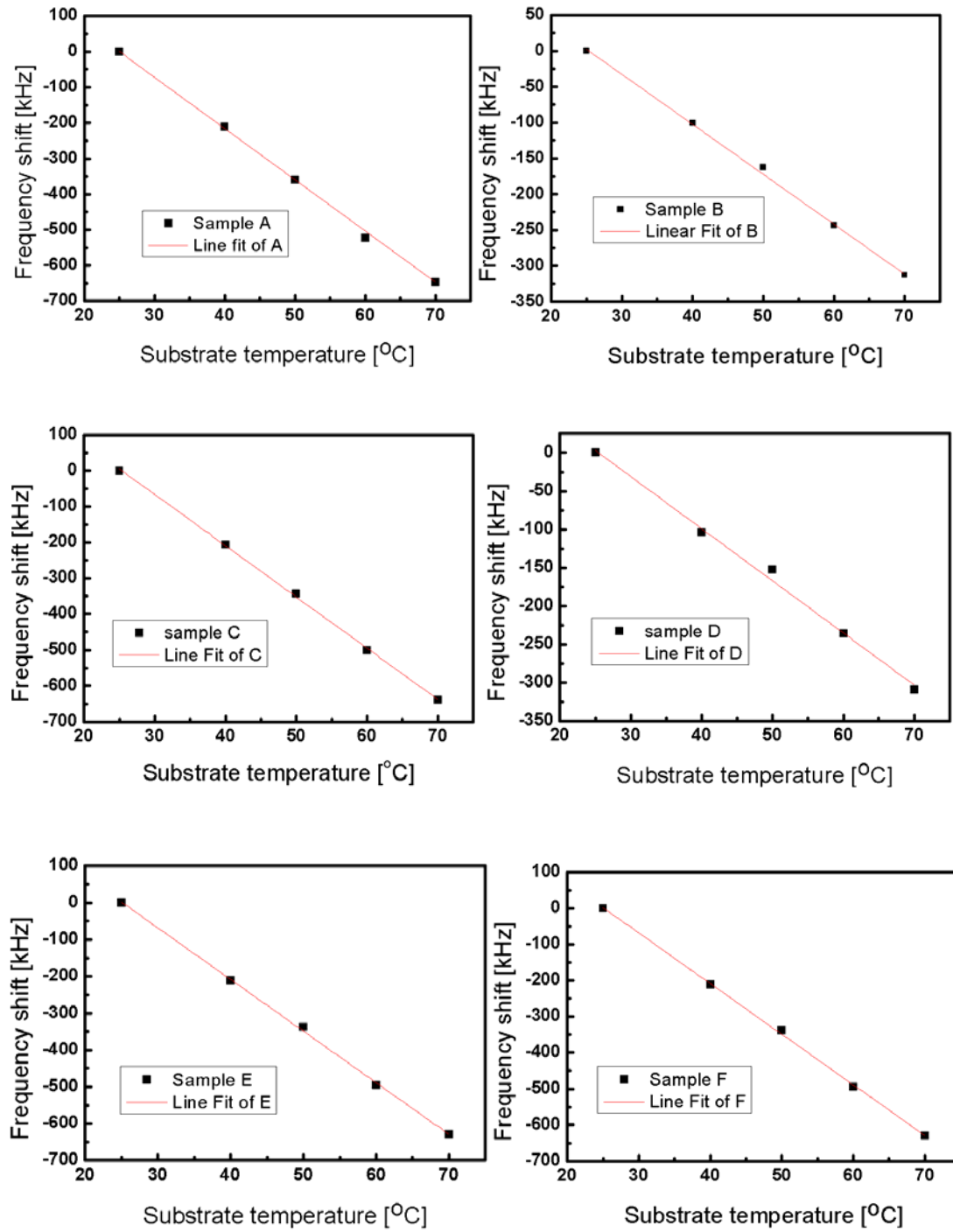


Figure 6.8 Frequency shift vs temperature, sample A-F

where f is the frequency, T is the temperature, L is the distance between the IDTs, v is the phase velocity and v_g is the group velocity of the wave. Assuming the phase velocity does not change with frequency, the equation can be simplified to

$$\text{TCF} = -\text{TCD} \quad (6.4)$$

The TCD for 128° X-cut lithium niobate at the room temperature is given in Ref. [15, 16] as 75 ppm/°C. In the experiments presented here the TCF of the sample A was measured as

$$\begin{aligned} \text{TCF} &= -\frac{\text{Temperature coefficients}}{\text{frequency}} \\ &= -\frac{-9975.56\text{Hz}/^\circ\text{C}}{124.86\text{MHz}} = -79.8\text{ppm}/^\circ\text{C} \end{aligned}$$

which differs by ~ 7% from the value given in the literature.

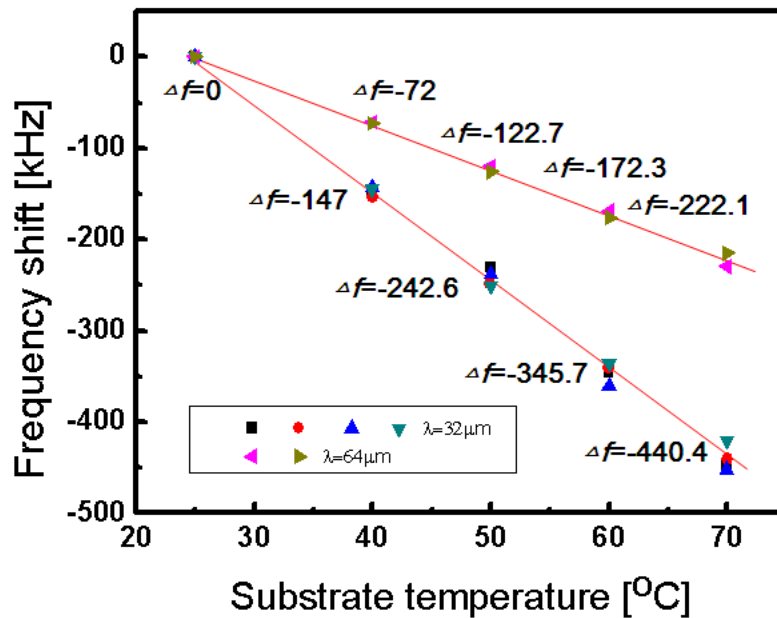


Figure 6.9 Frequency shift vs temperature

The frequency shifts as a function of substrate temperature for samples A-F are shown in Fig. 6.8 and are summarised in Fig.6.9. The data points were fitted linearly, leading to the temperature coefficients shown in Table 6.3. The curve-fitting coefficient (R) for all the samples varies between 0.99904 and 0.99959, indicating an excellent fit.

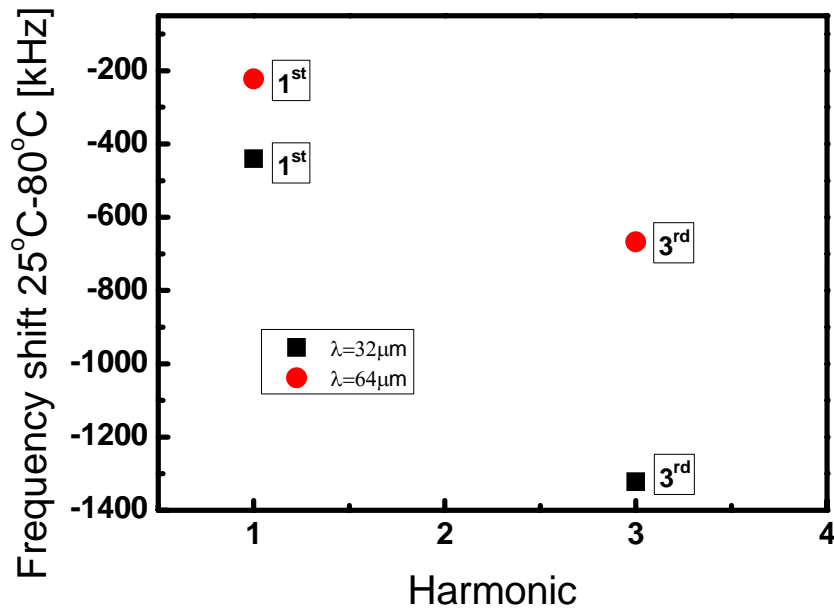


Figure 6.10 Shift between 25°C and 80°C at 1st and 3rd harmonic

Additionally, the frequency shift from 23° to 70° of the third harmonic was measured for Samples E and F. Fig.6.10 shows these with the average shift of the fundamental harmonic. As predicted by theory, the frequency shift increases linearly with absolute frequency.

Table 6.3 Temperature coefficients

Sample	Temperature coefficient [Hz/°C]	TCD [ppm/°C]
A	-9975.56	-79.8
B	-5097.78	-91.6
C	-10037.78	-80.5
D	-4773.33	-77.0
E	-9340.0	-75.1
F	-4773.33	-76.9

For SAW LiNbO₃ devices, the velocity of Rayleigh waves is constant, and is not dependent on the frequency, IDT geometry, metallization ratio or even the wave mode. The resonant frequency of a SAW device is determined by the spatial period of the IDT fingers and the intrinsic acoustic velocities of the LiNbO₃. The third harmonic mode wave was observed in addition to the fundamental Rayleigh wave. Similarly, the transmission amplitude of the Rayleigh wave is higher than that of the 3rd harmonic mode wave.

6.2 SAW signal of ZnO

From an application point of view, SAW devices with high frequencies are preferred, as they are effective in increasing the power density within the thin surface layer [17]. This can be realized using high-order harmonic-mode Rayleigh waves from a bulk SAW device, such as SAW LiNbO₃ devices. The drawback is that the signal amplitude of the high-order harmonic Rayleigh waves is relatively small [18, 19], restricting its application. SAW devices based on piezoelectric thin films (such as ZnO) grown on low-cost substrates have higher-order-mode waves, named Sezawa waves, whose performance is much better than that of the fundamental Rayleigh mode. This can be realized from a layered structure in which the substrate has a higher acoustic velocity than the overlaying film.

As stated before, SAW devices can also be fabricated on c-axis-oriented ZnO thin films deposited on Si (100) substrates. Unlike the constant Rayleigh velocity of SAW devices based on LiNbO₃, the ZnO film thickness has significant effects on the acoustic velocity of the SAW wave. In the following section, the performances of the SAW devices on ZnO films with different thicknesses (from 0.8 μm to 6.6 μm) were investigated.

6.2.1 Characterization of ZnO film and SAW signal of the Rayleigh mode

ZnO films of different thicknesses were prepared to study the effect of ZnO thickness on the reflection signal of SAW devices from the set of structures, namely ZnO/Si. The SAW signals on the layered ZnO/Si devices are also measured by the network analyzer. The velocity of both Rayleigh waves also follows the equation $f_r = v / \lambda$.

For each sample, the frequency responses of the reflected signals are also measured from the network analyzer. Therefore, the wave velocities can be calculated from the measured frequencies.

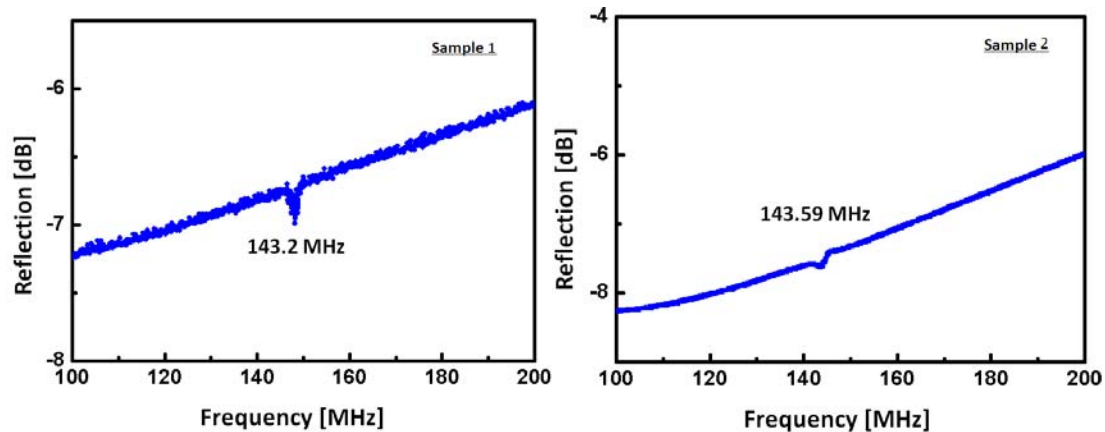
With the ZnO film thickness below 0.8 μm ($hk < 0.157$), no wave mode could be detected, due to the low electromechanical coupling coefficient for a very thin ZnO film using a wavelength of 32 μm [20, 21]. For devices with ZnO film thickness between 0.8 and 2.2 μm , the Rayleigh-mode resonant peak starts to appear, and the resonant frequency gradually decreases with increasing the ZnO film thickness.

Plots of reflection signal against frequency for different ZnO film thickness with 30 finger-pairs and 60 finger-pairs of IDT fabricated on ZnO/Si structure are shown in Fig. 6.11. The parameters of Sample 1-6 are listed in Table 6.4.

Table 6.4 The parameters of the SAW devices

Sample	Wavelength λ	Finger pairs N	Deposition time	ZnO film thickness
1	32 μm	30	1.5hr	$\sim 0.8\mu\text{m}$
2	32 μm	60	1.5hr	$\sim 0.8\mu\text{m}$
3	32 μm	30	3.5hr	$\sim 1.8\mu\text{m}$
4	32 μm	60	3.5hr	$\sim 1.8\mu\text{m}$
5	32 μm	30	5hr	$\sim 2.5\mu\text{m}$
6	32 μm	60	5hr	$\sim 2.5\mu\text{m}$

The figures show that the Rayleigh waves are at approximately the same frequencies when they are fabricated on films of equal thickness. However, there are some slight variations in the frequency values, which might result from the non-uniformity of the ZnO films deposited. This is because the devices for the 30 finger pairs and 60 finger pairs are a certain distance apart when they were patterned on the 4-inch wafer. In conclusion, the resonant frequencies are dependent on the thickness of ZnO films rather than the number of finger pairs [22, 23].



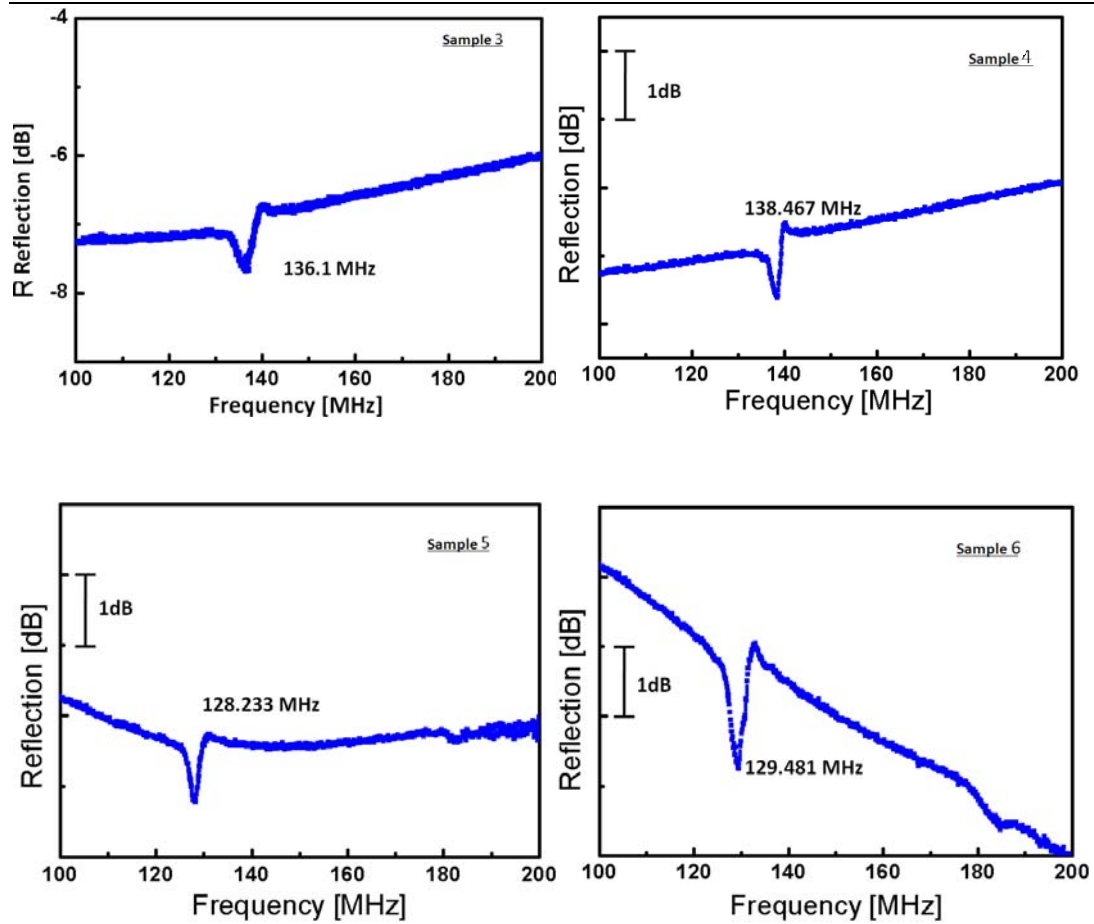


Figure 6.11 The reflection singles on the devices 1-6

Table 6.5 The performances of the SAW devices

Sample	Frequency f_0	Velocity	Reflection amplitude	Film/wavel ength ratio	Wave mode
1	142.2MHz	4550m/s	0.17dB	2.5%	Rayleigh
2	143.59MHz	4595m/s	0.19dB	2.5%	Rayleigh
3	136.1MHz	4355m/s	0.44dB	5.6%	Rayleigh
4	13847MHz	4431ms	0.84dB	5.6%	Rayleigh
5	128.23MHz	4103m/s	1.01dB	7.8%	Rayleigh
6	129.48MHz	4143m/s	2.38dB	7.8%	Rayleigh

From the above results, we can see that the resonant frequency gradually decreases with increasing ZnO film thickness. The variation in the phase velocity of the Rayleigh

mode with the film thickness can be explained by the different penetration depth of the Rayleigh wave into the substrate.

For a thin ZnO film, the SAW can penetrate much deeper into the substrate [24]. In this case, most of the SAW energy is localized in the substrate, thus the phase velocity of the SAW approaches the Rayleigh velocity of the substrate material (Si in our case). The velocity of the SAW propagating in the Si substrate (4680m/s) is higher than that in ZnO (2700m/s) [25]. With the increase in the ZnO layer thickness (i.e., increase in hk value), more acoustic energy localizes within the piezoelectric ZnO layer, so the SAW wave velocity gradually decreases and consequently reaches the same value as that of the ZnO film.

6.2.2 Characterization of ZnO film and SAW signal of the Rayleigh mode and high-order mode

It was found that a Rayleigh wave is only present in a ZnO SAW when the ZnO thickness is less than 4 μm . With film thicknesses larger than 4 μm , a high-order resonant peak, which is the Sezawa-mode wave, appears in addition to the Rayleigh-mode wave, as shown in Fig.6.12. The Sezawa mode exhibits a higher phase velocity than the Rayleigh-mode wave. The amplitude of the Sezawa wave is much larger than that of Rayleigh wave, and it increases with increase in thickness of the ZnO film. This can be attributed to the improved film quality (including grain size and crystal quality) and piezoelectric and electromechanical coupling properties that are associated with an increase in the film thickness. As with the Rayleigh mode, the phase velocity of the Sezawa mode decreases with the increasing thickness of the ZnO film. The parameters of Sample 7-12 are listed in Table 6.6.

Table 6.6 The design parameters of the devices 7-12

Sample	Wavelength λ	Finger pairs N	Deposition time	ZnO film thickness	Normalised thickness hk
7	32 μm	30	8.5hr	4.0 μm	0.79
8	32 μm	60	8.5hr	4.0 μm	0.79
9	32 μm	30	11hr	5.5 μm	1.08
10	32 μm	60	11hr	5.5 μm	1.08
11	32 μm	30	13hr	6.6 μm	1.32
12	32 μm	60	13hr	6.6 μm	1.32

Based on the theoretical analysis by G. W. Farnell and E. L. Adler (as shown in Fig. 6.13) [26], higher-frequency Sezawa-mode waves are induced at a certain thickness of a layered structure – approximately $hk=1$ for the first Sezawa mode and $hk=3$ for the second Sezawa mode. Rayleigh-mode waves are observed with most of our SAW devices with ZnO thickness $h > 0.8 \mu\text{m}$. The first series of Sezawa-mode waves are observed for SAW devices with a ZnO film thickness of 4~6.6 μm (corresponding to $hk=0.8\sim 1.3$), consistent with the theoretical analysis. The appearance of the Sezawa-mode wave in a device with $hk=0.8$ indicates high crystal quality and high performance of the SAW devices fabricated. With the increase in ZnO thickness, the Sezawa mode tends to have a frequency dominated by the velocity of the ZnO layer. This is similar to the Rayleigh-mode wave, which starts with the Rayleigh velocity of the substrate material of Si, and approaches that of the Rayleigh velocity of the ZnO as the kh value increases, as shown in Figure 6.13 [27].

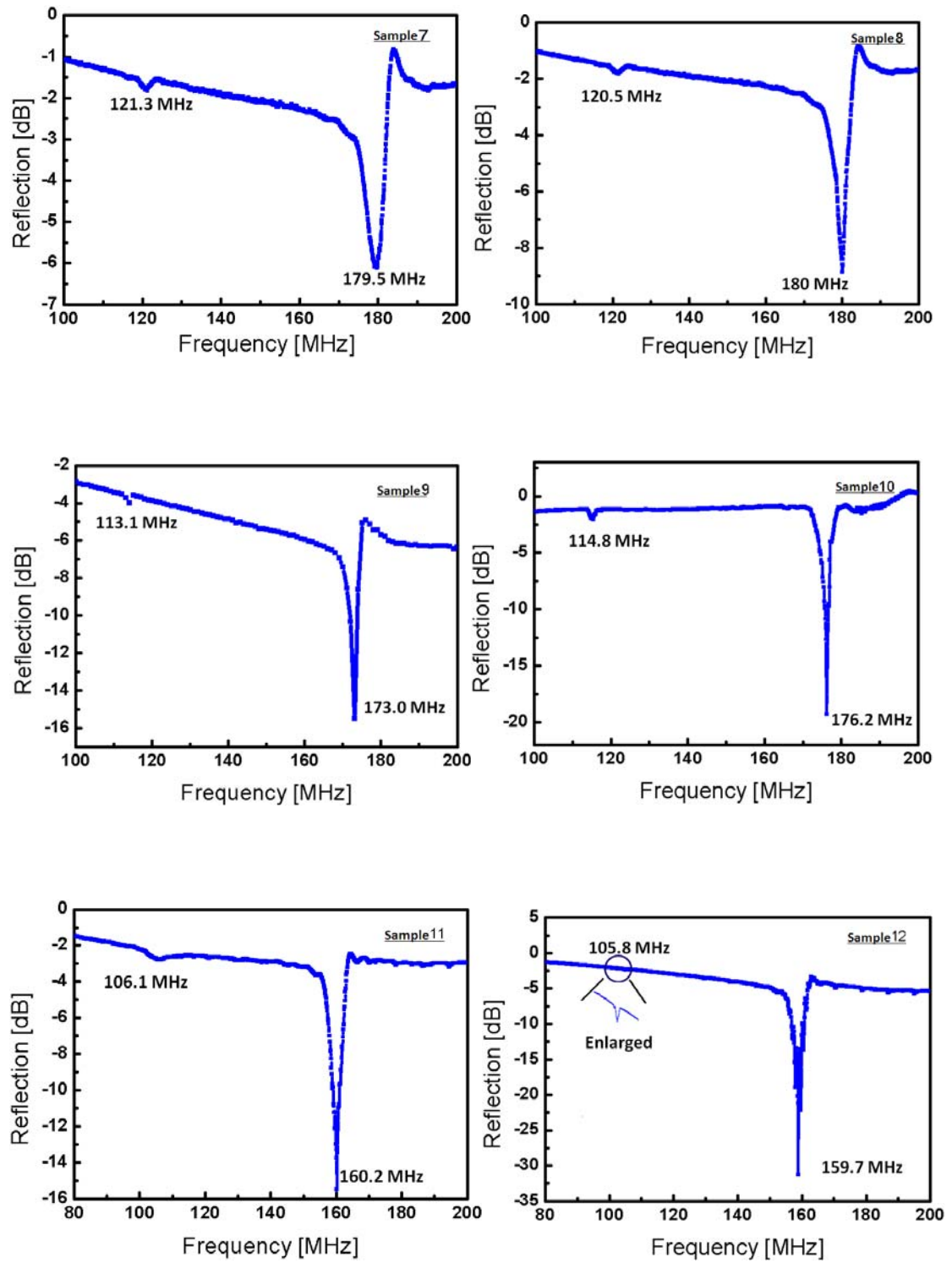


Figure 6.12 The reflection signal of the devices 7-12

Table 6.7 The performance and measurements of the devices

Sample	Frequency f_o	Velocity	Reflection amplitude	Film/wavel ength ratio	Wave mode
7	121.3MHz	3881.6m/s	0.25dB	12.5%	Rayleigh
	179.5MHz	5744m/s	4.32dB	12.5%	Sezawa
8	120.5MHz	3856m/s	0.25dB	12.5%	Rayleigh
	180MHz	5760m/s	8.04dB	12.5%	Sezawa
9	113.1MHz	3619.2m/s	0.47dB	17.2%	Rayleigh
	173MHz	5536m/s	9.91dB	17.2%	Sezawa
10	114.8MHz	3673.6m/s	0.58dB	17.2%	Rayleigh
	176.2MHz	5638.4m/s	17.92dB	17.2%	Sezawa
11	106.1MHz	3395.2m/s	0.18dB	20.6%	Rayleigh
	160.2MHz	5126.4m/s	12.53dB	20.6%	Sezawa
12	105.8MHz	3385.6m/s	0.26dB	20.6%	Rayleigh
	159.7MHz	5110.4m/s	27.8dB	20.6%	Sezawa

Theoretical prediction [26] showed the phase velocity is close to that of the Rayleigh velocity of the substrate material at $hk \sim 0$. As the hk value increases, the phase velocity decreases monotonically until it approaches the Rayleigh velocity of the surface material at $hk \gg 1$ (see Fig. 6.14) [27]. In Fig. 6.13, it can be seen that our results are absolutely consistent with the predicted values.

The results clearly show that the Sezawa-mode waves have a high resonant frequency and high signal amplitude. The Sezawa mode possesses a higher electromechanical coupling coefficient ($K^2 \sim 4\%$ [27]) compared to the Rayleigh mode ($K^2 \sim 0.49\%$ [28]), which is consistent with our results. Additionally, the operating frequency f_t of the Sezawa mode is higher than that of Rayleigh mode.

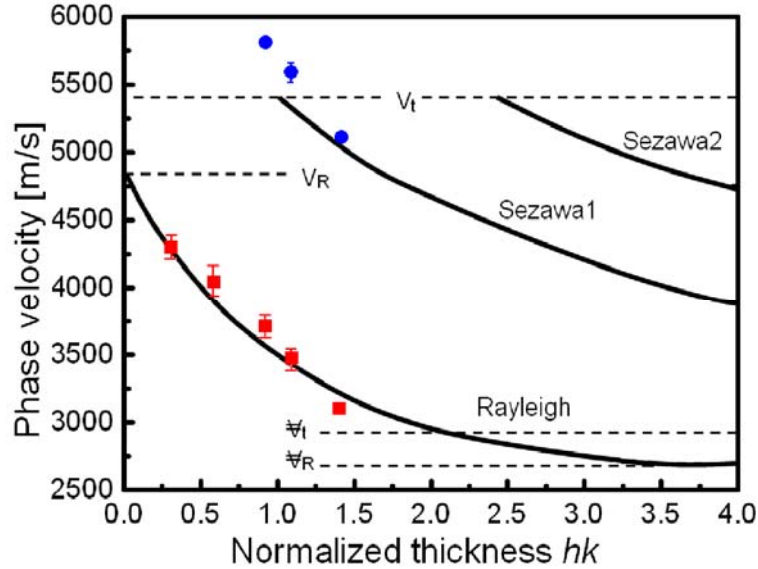


Figure 6.13 Phase velocities for the Rayleigh and Sezawa modes on different thicknesses of ZnO film. V_t , v_t the shear velocities of the Si and ZnO; V_R , v_R the Rayleigh velocities of the Si and ZnO

In brief, the SAW velocity for a thin ZnO film is close to that of the Si substrate. It decreases with an increase in ZnO thickness, and approaches that of the ZnO as the surface layer thickness increases. In addition to the Rayleigh wave, a Sezawa-mode wave with a higher resonant frequency was also observed for devices with a thick ZnO film (thickness larger than $2.8 \mu\text{m}$). The signal amplitude of the Sezawa wave is much stronger than that of Rayleigh mode wave.

6.2.3 The dependence of the velocities of the Rayleigh and Sezawa waves on the ZnO film thickness

From the above results, the velocity of the wave is greatly dependent on the ZnO film thickness. But ZnO SAWs, which had been deposited for the same sputtering time, exhibited slightly different resonant frequencies. For example, in devices with the same ZnO film thickness, the resonant frequencies can vary as much as $\pm 4\text{MHz}$. This is because the sputtering of the ZnO film is not uniformly thick, even on the

same wafer. The centre of the wafer has the thickest film thickness, and the thickness decreases in regions away from the centre. Even a small change in the ZnO film thickness can result in a variation of the wave velocity, leading to a change in the resonant frequency.

To investigate the variation of the ZnO film thickness on the resonant frequency, Matlab (polyfit) is used to find the coefficients of a polynomial that fits a set of data in a least-squares sense. Here, Matlab (polyfit) is used to optimally fit the nonlinear relationship between the ZnO film thickness and the resonant frequency. – See Appendix.

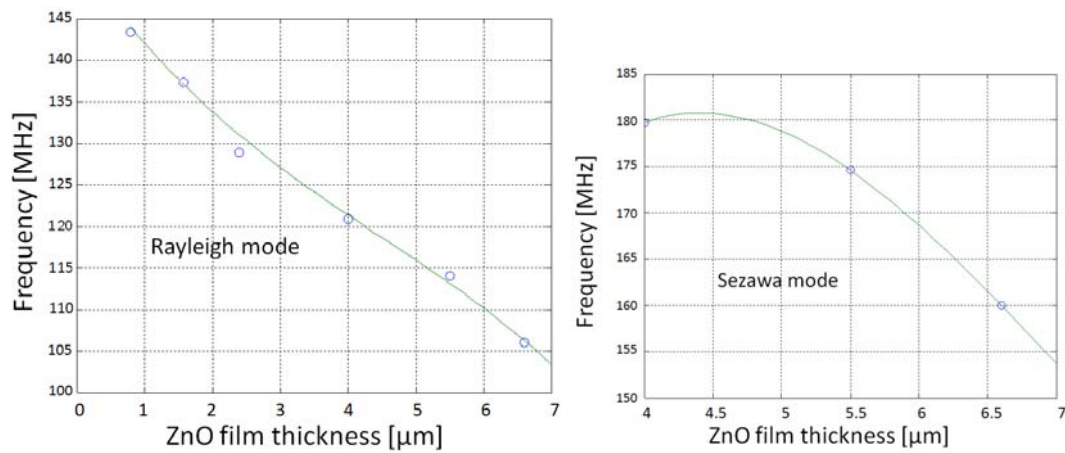


Figure 6.14 Matlab curve fitting of the Rayleigh wave (left) and Sezawa wave (right)

Curve-fitting is preferable when small or imperfect data are needed to be plotted in a profile of smooth curve for presentation purposes. Matlab (polyfit) can change some discrete data points into a continuous curve. In fact, it is not necessary for the fitting curve to go through all data points.

From the tangent of the fitting curve at each point, the extent to which the phase velocity will change per unit ZnO film can be obtained.

$v = f \times \lambda \Rightarrow \Delta v = \Delta f \times \lambda$, v, f are the phase velocity and resonant frequency respectively; λ , wavelength, is $32\mu\text{m}$ in this case, and h is the ZnO thickness.

$$\left. \frac{df}{dh} \right|_{x_0} = y'(x) \Big|_{x_0} \quad (6.5)$$

Taking the $5.5 \mu\text{m}$ ZnO on a silicon substrate as an example: $y'(x) \Big|_{x_0=5.5}$ is -9.131 and -5.5478 for the Sezawa and Rayleigh curves respectively. The value of $y'(x) \Big|_{x_0=5.5}$ is negative because the resonant frequency decreases with increasing ZnO thickness. For the Sezawa wave, the resonant frequency is 174.6 MHz for a $5.5 \mu\text{m}$ thick ZnO layer on a silicon substrate, and $\Delta x \Big|_{x=5.5} = 0.1 \Rightarrow \Delta f \Big|_{x=5.5} = -0.913$, indicating that if the ZnO thickness increases by $0.1\mu\text{m}$, i.e. for a $5.6\mu\text{m}$ thick ZnO layer, the resonant frequency will drop from 174.6 MHz to 173.7 MHz , and a reduction of $|\Delta f| = 0.913 \text{ MHz}$ occurs.

From $\Delta v = \Delta f \times \lambda$, a frequency shift of 0.913 MHz is equivalent to a phase velocity change of 29.2 m/s . Similarly, for the Rayleigh wave, the increased $0.1 \mu\text{m}$ ZnO thickness leads to a resonant frequency drop of 0.5478 MHz and a velocity drop of 17.8 m/s .

For the $5.5 \mu\text{m}$ ZnO thick samples, an increase of $0.1 \mu\text{m}$ in the ZnO thickness (i.e. to $5.6\mu\text{m}$) will result in a phase velocity drop of 29.2 m/s and 17.8 m/s for the Sezawa and Rayleigh waves, corresponding to negative frequency shifts of 0.913 MHz and 0.5478 MHz , respectively. This can explain why the frequency of devices made on the same fabrication batch varies a lot. Even on a small sample, the thickness is not uniform.

6.2.4 SAW on ZnO island

The primary goal of the research is to develop SAW-based microfluidics. Although ZnO is biosafe, it reacts vigorously with acids and bases [29], and will dissolve or

recrystallize if the ZnO is exposed to water or humid conditions [30]. Therefore, ZnO SAW devices with no surface protection are not stable enough for long-term applications. Surface coating is considered as an effective way to protect the ZnO thin films from degradation. Here we propose a novel ZnO SAW structure that can prevent direct contact between the ZnO active layer and potential biofluids (samples and reagents).

As discussed above, since the acoustic wave in a thin ZnO-film-based SAW device is strongly affected by the wave propagating in the Si substrate, it can easily be seen that the two functions of the generation and propagation of the surface acoustic wave can be separated by using different substrates. Here we propose a new SAW structure, as shown in Fig.6.15. The SAW device is fabricated on thin-film ZnO islands, with the surrounding ZnO material being removed. As a result, the SAW devices on the ZnO islands can be used to generate the acoustic waves which propagate solely in the Si (or glass) substrate, which can be applied for acoustic mixing, pumping, or even sensing while microchannel and other components are fabricated on the Si/glass substrate directly.

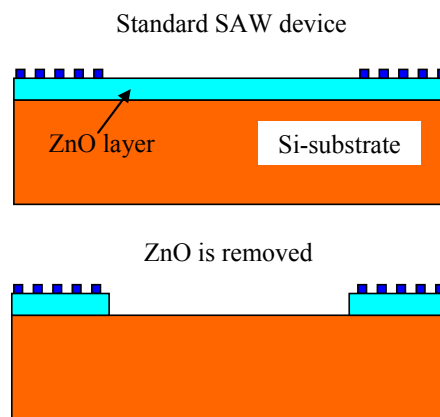
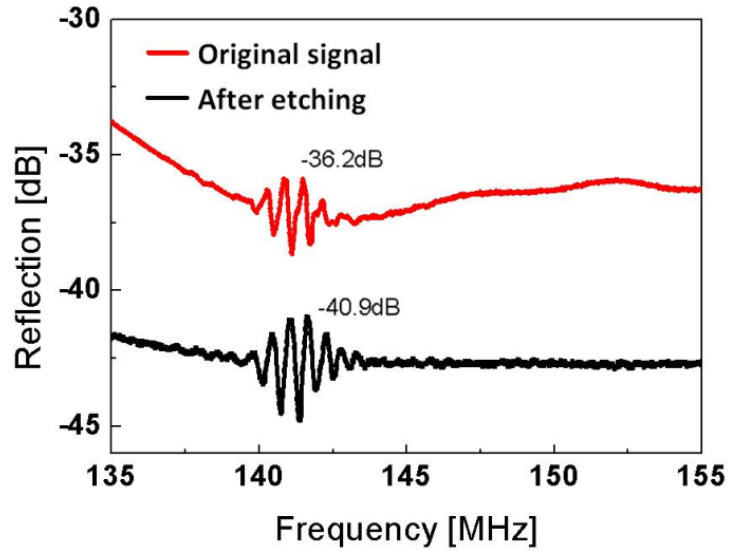
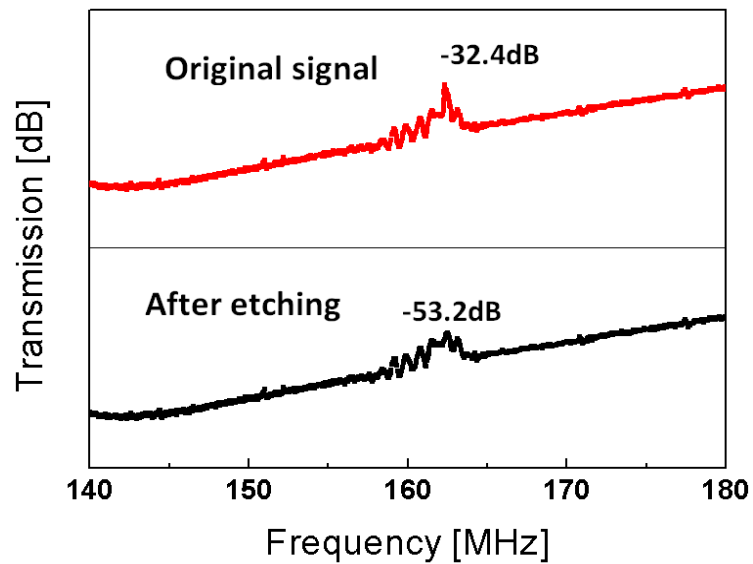


Figure 6.15 schematic drawing of the proposed new SAW structure with ZnO on the wave path being removed



(a)



(b)

Figure 6.16 (a) Comparison of transmission spectra of the Rayleigh wave from the SAW on a 1.2 μm ZnO (a), and of the Sezawa wave from the SAW on a 6.6 μm ZnO (b) with and without ZnO layer in the wave path

Figure 6.16 provides a comparison of Rayleigh- (a) and Sezawa- (b) mode transmission spectra of SAW devices with and without a ZnO propagation path. The SAWs were made on the ZnO-film-coated Si substrates first; then the ZnO film between the two opposite IDTs was etched by using Al etchant to expose the Si

substrate (mainly HCl). It was found that the transmission spectra depend on the thickness of the piezoelectric active layer. For the SAW device on a 0.8 μ m ZnO film, the absolute value of the transmitted signal of the Rayleigh- and Sezawa-mode waves decreases after removing the ZnO in the wave path, but the amplitude of the Rayleigh wave remains almost unchanged. For the SAW on a 6.6 μ m ZnO layer, the absolute value of the transmission signal of the dominant Sezawa wave decreases after removing the ZnO, and the amplitude of the Sezawa wave decreases significantly as well.

The wavelength is determined by the IDT periodicity and the acoustic speed in the substrate and overlayer, and is not affected by the active layer in its path. For a layer structure, the waves travel with a certain proportion of the wave which penetrates into the thin surface layer. Since the wavelength is 32 μ m, the acoustic energy is mainly trapped within the silicon substrate, with a certain proportion in the thin surface overlayer. 0.8 μ m of ZnO is only 2.5% of the wavelength, and therefore removal of such a thin layer on the wave path does not affect the transmission signal significantly. As the ZnO thickness increases to 6.6 μ m, \sim 20% of the wavelength, removal of such a thick ZnO layer alters the traveling depth of the wave, thereby changing the transmission signal significantly for the Sezawa wave.

From the above results, it is observed that although the Si substrate is not a piezoelectric material, the SAW wave still propagates from the IDT to the other side with the ZnO film underneath the IDTs. After etching the ZnO layer, the Si substrate that is used as the interface between the ZnO layer and the Si becomes the free surface of the SAW.

6.3 Conclusions

- SAW signals with 32 μ m and 64 μ m wavelength on 128^o Y-cut LiNbO₃ substrates have been measured by the network analyzer.

- The third harmonic mode appears with the fundamental Rayleigh wave.
- The amplitude of the fundamental mode is larger than that of the harmonic mode.
- Unlike the LiNbO₃ devices, the resonant frequencies of ZnO/Si devices are dependent on the thickness of ZnO films.
- A high-order resonant peak, which is the Sezawa-mode wave, appears in addition to the Rayleigh-mode wave when ZnO film thicknesses are larger than 4 μm.
- The Sezawa-mode waves have a high resonant frequency and high signal amplitude.
- All the wave modes follow the equation: $v = f_r * \lambda$.

Reference

- ¹ The investigation of Digitimes on the Internet: “The tendency of the industry of mobile phone SAW filters”. 2000/4.
- ² J. W. Gardner, V. K. Varadan and O. O. Awadelkarim. *Microsensors, MEMS and Smart Devices*. (Wiley, New York, 2001).
- ³ V. Laude, L. Robert, W. Daniau, A. Khelif and S. Ballandras. “Surface acoustic wave trapping in a periodic array of mechanical resonators”. *Appl. Phys. Lett.* 89 (2006) 083515.
- ⁴ I.T. Tang, H. J. Chen, W. C. Hwang, Y. C. Wang, M. P. Houg and Y. H. Wang. “Applications of piezoelectric ZnO film deposited on diamond-like carbon coated onto Si substrate under fabricated diamond SAW filter”. *J. Crystal Growth*. 262 (2004) 461.
- ⁵ S. Petroni, G. Tripoli, C. Combi, B. Vignaa, M. De Vittoriob, M.T. Todarob, G. Epifanib, R. Cingolanib and A. Passaseob. “GaN-based surface acoustic wave filters for wireless communica”. *Superlattices and microstructures*. 36 (2004) 825.
- ⁶ C.K. Campebell. “Obtaining the fundamental and harmonic radiation conductances of a reflective SAW interdigital transducer”. *Proc. IEEE Ultrason. Symp.* 1 (1998) 169.
- ⁷ R. Huegli. “Harmonic GHz surface-acoustic-wave filters with unidirectional ltransducers”. *IEEE Transactions on Ultrasonics*. 40 (1993) 3.
- ⁸ V. Vivek, Y. Zeng and E. S. Kim. “Novel acoustic-wave micromixer”. *Proc. MEMS’00, 13th IEEE Int. Workshop Micro Electromechanical System (Miyazaki, Japan) 2000* 668.
- ⁹ S. Shiokawa, Y. Matsui and T. Moriizumi. “Experimental study on liquid streaming by SAW”. *Jpn. J. Appl. Phys.* 28, Suppl. 28 (1989) 126.
- ¹⁰ N. W. Emanetoglu, G. Patounakis, S. Muthukumar and Y. Lu. “Analysis of temperature compensated SAW modes in ZnO/SiO₂/Si multilayer structures”. 2000 *IEEE Ultrasonics Symposium* 325.

- ¹¹ N. Dewan, K. Sreenivas and V. Gupta. “Theoretical studies on TeO₂/ZnO/diamond-layered structure for zero TCD SAW devices”. *Semicond. Sci. Technol.* 23(2008) 085002.
- ¹² Y. H. Kim, D. H. Chang, and Y. S. Yoon. “Study on the optimization of a temperature sensor based on SAW delay line”. *Journal of the Korean. Physical Society.* Vol 45 (No. 5) (2004) 1366.
- ¹³ Andrew J. Jr. Slobodnik. “The temperature coefficients of acoustic surface wave velocity and Dela on lithium niobate, lithium tantalite, quartz and tellurium dioxide.” *Physical Sciences Research Papers* 477, Air Force Cambridge Research Laboratories,1972.
- ¹⁴ Y. Yoshino, M. Takeuchi,K. Inoue, T. Makino, S. Arai and T. Hata. “Control of temperature coefficient of frequency in zinc oxide thin film bulk acoustic wave resonators at various frequency ranges”. *Vacuum.* Vol. 66 (No. 3) (2002) 467.
- ¹⁵ I. E. Kuznetsova, B.D.Zaitsev and S. G. Joshi. “Temperature characteristics of acoustic wave propagating in thin piezoelectric plates”. 2001 IEEE Ultrasonics Symposium 157.
- ¹⁶ S.G. Joshia, B.D. Zaitsevb, I.E. Kuznetsovab, A.A. Teplykhh and A. Pasachhea. “Characteristics of fundamental acoustic wave modes in thin piezoelectric plates”. *Ultrasonics.* Vol. 44 (Supplement 1) (2006) 787.
- ¹⁷ G.Q.Zhang, Hashimoto and Yamaguchi. “Liquid streaming by high-frequency ultrasonic waves”. *Jpn. J. Appl. Phys.* 35 (1996) 3248.
- ¹⁸ N.W.Emanetogus, C.Gorla, Y.Liu, S.Liang and Y.Lu; “Epitaxial ZnO piezoelectric thin films for saw filters”. *Mater. Sci. in Semicond. Processing.* 2 (1999) 247.
- ¹⁹ M.El Hakiki, O.Elmazria, M.B.Assouar, V.Mortet, L.Briezoua, M.Vanecek and P.Alnot. “ZnO/AlN/diamond layered structure for SAW devices combining high velocity and high electromechanical coupling coefficient”. *Diamond & Related Materials;* 14 (2005) 1175.
- ²⁰ T. Wu and W. Wang. “An experimental study on the ZnO/sapphire layered surface

acoustic wave device”. *J. Appl. Phys.* 96 (2004) 5249.

²¹ S. Wu, Y. C. Chen and Y. S. Chang. “Characterization of AlN Films on Y-128° LiNbO₃ by surface acoustic wave measurement”. *Jpn.J.Appl.Phys.* 41 (2002) 4605.

²² Showko Shiokawa, Yoshikazu Maysui and Yoyasaka Moriizumi. “Experimental study on liquid streaming by SAW”. *Jap. J. Appl. Phys.* 28 (1989) 126.

²³ G. Mchale, M.K. Banerjee and M.I. Newton. “Surface acoustic wave resonances in the spreading of viscous fluids”. *Phys. Rev. B.* 59 (1999) pp.8262.

²⁴ A. Talbi, F. Sarry, L. Brizoual, O. Elmazria and P. Alnot. “Sezawa mode SAW pressure sensors based on ZnO/Si structure”. *IEEE Trans. on Ultraonics, Ferroelectr & Freq. Control.* 51 Issue 11 (2004) 1421.

²⁵ V. Panella, G. Carlotti, G. Socino, L. Giovannini, M. Eddrief, K Amimer and C. Sebenne. “Brillouin scattering study of epitaxial InSe films grown on the Si(111)1x1-H surface”. *J. Phys: Condens. Matter.* 9 (1997) 5575.

²⁶ X.Y. Du, Y.Q. Fu, S.C. Tan, J.K. Luo, A.J. Flewitt, W.I. Milne, D.S.Lee, S.Maeng, S.H.Kim, N.M.Park, Y.J.Choi, J.Park and Y.J.Choi. “ZnO film thickness effect on surface acoustic wave modes and acoustic streaming”. *Appl. Phys. Lett.* 93 (2008) 094105.

²⁷ I. Tang, H. Chen, M. Houg and Y. Wang. “A novel integrable surface acoustic wave notch filter”. *Solid State Electronics.* 47 (2003) 2063.

²⁸ L. Brizoual, O. Elmazria, F. Sarry and M. Hakiki, A. Talbi and P. Alnot. “High frequency SAW devices based on third harmonic generation”. *Ultrasonics.* 45 (2006) 100.

²⁹ B. A. Buchine, W. L. Hughes, F. L. Degertekin and Z. L. Wang. “Bulk acoustic resonator based on piezoelectric ZnO belts”. *Nano. Lett.* 6 (2006) 1155.

³⁰Y. Shu and D. F. Xue. “Soft solution synthesis of ZnO films with developed superstructures”. *4th Int. Conf. on Technol. Advance of Thin Film & Surf. Coatings.* Singapore. (2008) 92.

Chapter 7. Streaming by Surface Acoustic Wave

Recently, there has been an increased interest in SAW-based biosensors and microfluidic systems using high-performance piezoelectric materials [1, 2, 3]. SAW-based biochemical sensors normally have high sensitivity and low detection limits, in the order of a few pg/ml. In order to detect the presence of biological material such as cancer cells, proteins or DNA, it is essential to handle small amounts of liquids, such as biofluidic samples and reagents, to immobilize and bind the target molecules on the surface of biosensors. However, handling such liquid droplets in small volumes is one of the most challenging tasks in the development of biotechnology. Various micropumps and micromixers have been developed to control, manipulate and mix the minute amounts of liquid in micro-liter (μl) and picoliter (pl) volumes.

However, effectively mixing in microfluidic devices is challenging, due to their inherent low-Reynolds-number flow conditions [4]. Methods of micromixing are currently dominated by passive mixing in microchannels or microchambers through static structures such as microposts and serpentine structures, or by capillary dragging force. Complete mixing is rather difficult, leading to incomplete reaction and deficient biochemical detection in these microfluidic systems [5]. Thus, improving the diffusion-dominated passive mixing process in microfluids has become a crucial issue for the development of microfluidics and labs-on-chips. Various technologies have been developed for active mixing, such as the cantilevers and membranes [6]. They

are complicated, costly and unreliable for operation due to the moving components involved.

Recently, a new type of micromixer using SAWs has been developed [7, 8, 9, 10, 11], showing great potential in microfluidic applications. The SAW-based micromixer is simple in structure and fabrication, low-cost, and generally an effective and reliable mixing device that does not require moving parts. SAW micromixers take advantage of the unique properties that are dominant at the micron and nanometre scales, such as compactness, high frequency response, high precision and ease of control [12].

SAW-driven microfluidic devices control and manipulate liquids on a non-partitioned, flat surface with precision in both position and quantity, and mix liquids in microliter quantities efficiently. When liquid, either in bulk or droplet form, is present on the surface of a SAW device, the energy and momentum of the acoustic waves will be coupled into the fluid, inducing streaming and motion of the liquid. The excited longitudinal waves propagate into the liquid at an angle called the Rayleigh angle, following Snell's law of diffraction (see Fig.7.1) [13, 14, 15]. The Rayleigh angle, θ , can be defined by

$$\theta = \sin^{-1}\left(\frac{V_L}{V_s}\right) \quad (7.1)$$

where, V_L and V_s are the velocities of the longitudinal wave in the liquid and leaky wave in the solid substrate, respectively. Due to the excessive damping and loss of the longitudinal acoustic wave, the Rayleigh mode SAW device is considered unsuitable for sensing in a liquid environment [16, 17, 18]. However, the energy and the momentum of the longitudinal wave irradiated into the liquid are quite useful for liquid mixing.

Although SAW-based microfluidics have been developed, the details of operation and mechanisms are far from clear. It is necessary to clarify how the wave modes affect

the mixing and streaming efficiency, and to elucidate the mechanism behind the manipulation and pumping of droplets by the acoustic wave.

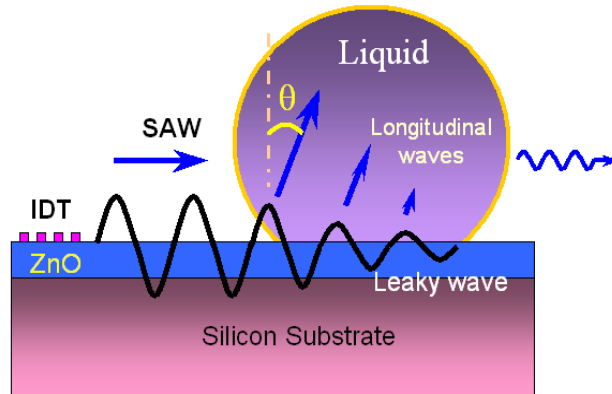


Figure 7.1 Schematic diagram of the interaction between a surface acoustic wave and a liquid droplet

The following section will deal with how the SAW based on both a LiNbO_3 and a ZnO/Si substrate induces acoustic streaming and pumping, focusing on the effects of the wave mode and surface modification.

7.1 Streaming within a droplet on LiNbO_3

As mentioned in Chapter 5, SAW devices with wave lengths of 32 and 64 μm were fabricated on 128° Y-cut LiNbO_3 substrates with Al interdigital transducers. Higher-order harmonic-mode waves appear in addition to the fundamental Rayleigh wave. Both waves will demonstrate the ability to induce acoustic streaming. The fundamental Rayleigh and the high-harmonic wave will be investigated to determine which mode obtains the highest mixing efficiency, and hence the highest streaming velocity. The relationship between the streaming velocity and RF signal voltage will also be investigated.

Higher-order harmonic mode waves, typically the odd-mode harmonic waves, can be generated simultaneously in the SAW devices. They have a much higher frequency;

however, high-order harmonic waves normally have a weaker transmission signal. At the time of writing, there do not appear to be any reports as to whether the higher-order harmonic-mode waves can be utilized in micromixing and micropumping. In this study we fabricated the SAW devices on LiNbO_3 substrates, and will investigate the acoustic streaming using both the fundamental mode and the third-mode harmonic wave in detail.

For the experiments of SAW streaming in a liquid droplet, droplets with an accurate volume of 0.5~10 μl were loaded on the surface of the SAW devices using a Micro-Volume Kit micropipette. For these experiments, the LiNbO_3 surface is not treated, to avoid uncertainty induced by droplet motion. An Agilent N9310A signal generator was used to supply RF signals at the resonant frequency, which was then amplified using an Agilent 6642A power-amplifier to obtain sufficient signal voltage amplitude for microfluidic experiments. The liquid streaming phenomenon was captured by a digital camera (Motic MCCamera) for detailed analysis.

7.1.1 Streaming on LiNbO_3

The SAW-driven streaming within a droplet can be demonstrated by injecting some ink particles into the liquid, while the liquid velocity was determined by measuring the speed of the particles moving through the centre of the droplet. As the RF signal voltage applied to the SAW devices increases to a certain level, internal streaming and flow within a droplet is observed. The acoustic-wave-induced streaming within a droplet has a semicircular pattern, as shown in Fig.7.2. The flow velocity was found to be dependent on the position of the streaming within the droplet; it is fastest in the centre of the droplet. For comparative purposes, the flow velocity in the middle of the streaming pattern is measured and used for discussion.

Figure 7.3 shows the streaming velocity within a droplet on the SAW surface as a function of RF signal voltage for various devices and wave modes. The flow

velocities show a high linearity with the signal voltages applied above 0.5 V for both the wave modes and devices, reaching 18 cm/s with a voltage of 2.25 V for the 1st mode wave of the SAW ($\lambda=32 \mu\text{m}$). This flow velocity is at least one order of

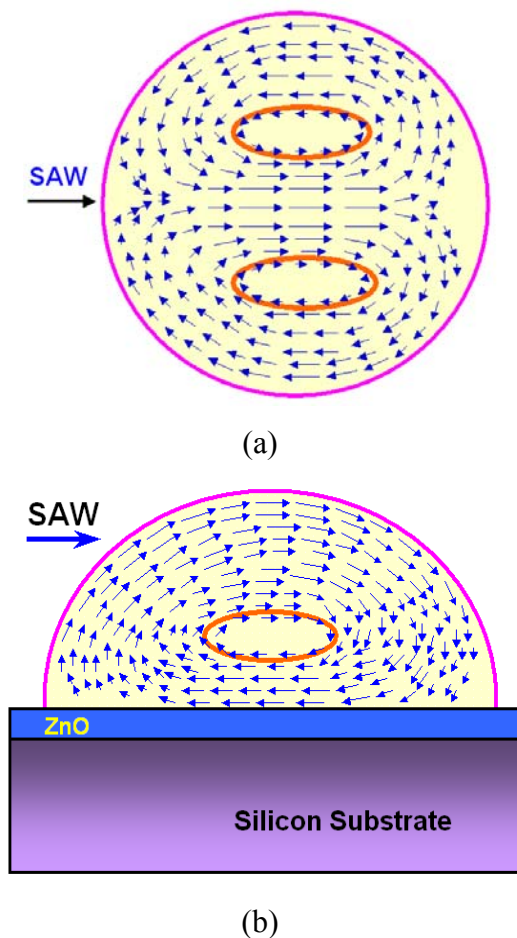


Figure 7.2 Schematic diagrams of acoustic streaming within a droplet. (a) is a top view, and (b) is a side view



Figure 7.3 Example of droplet streaming at approximately 5 V (peak to peak) on untreated LiNbO_3

magnitude higher than those of other micromixers [19]. The flow velocity induced by the SAW device with a wavelength of 32 μm is larger than the one with a wavelength of 64 μm . As mentioned previously, a high-frequency SAW has a high acoustic energy density, owing to the acoustic energy being confined within a thinner layer.

Figure 7.4 also shows the comparative results of flow velocities induced by the 1st and 3rd harmonic mode waves. It is clear that the fundamental wave induces a much higher streaming velocity than the 3rd mode wave. The ratio of the velocities induced by the 1st-mode wave to that of the third-mode wave is about 3-5, roughly the ratio of the corresponding amplitudes of the wave peaks observed in the transmission spectra as discussed in Chapter.6.

Figure 7.5 shows the streaming velocity as a function of signal voltage with finger pairs, N , as a parameter. The flow velocities induced in a SAW with 60 pairs of IDT fingers are higher than that found using 30 pairs of IDT fingers. This is because the amplitudes of the transmitted waves of the devices with the 60 pairs of IDT fingers are larger than that induced by the 30 pairs of fingers, and again the velocity induced by the 1st-mode wave is larger than that induced by the 3rd-mode wave, consistent with the results shown in Fig.7.4.

Acoustic waves from a SAW device can also be used to induce streaming in a continuous liquid with a steady flow pattern when the RF signal with a certain voltage is applied to the SAW device. The flow pattern shows a symmetrical butterfly shape (vortex shape), as illustrated in Fig.7.6(a), and the size of the butterfly pattern becomes larger as the RF signal voltage or power applied increases. The liquid near the IDT can be pumped significantly. Acoustic waves can travel for a long distance in a SAW device without any liquid in its path, and the signal typically becomes larger as the RF signal voltage or power increases. The velocity in the area close to the IDT edge is high, but decreases rapidly away from the IDT electrode.

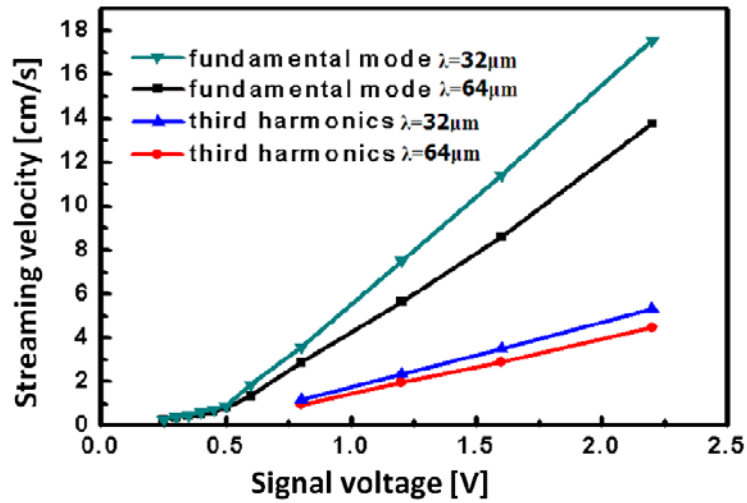


Figure 7.4 Flow velocity induced by an acoustic wave as a function of RF signal voltage applied. All SAWs had 60 finger pairs

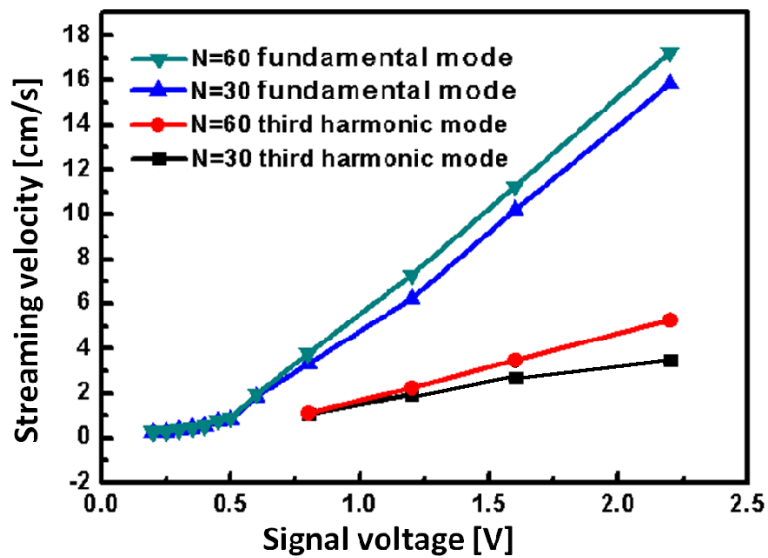


Figure 7.5 Dependence of streaming velocity on applied voltage with figure pair as a parameter, $\lambda=32\mu\text{m}$

The flow velocity induced by the acoustic wave in a liquid tank was found to be similar to that within a droplet, up to 10 cm/s, depending on the RF signal voltage applied and the volume of the liquid used.

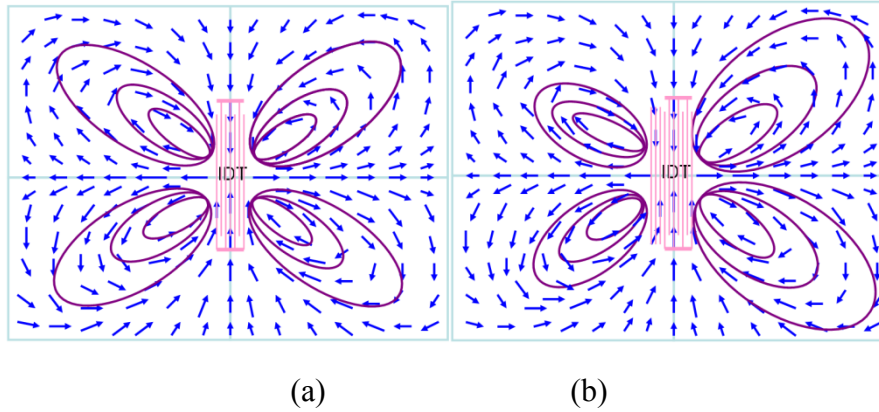


Figure 7.6 Flow pattern of acoustic streaming in liquid tank induced by an acoustic wave in SAW devices with (a) and without (b) a reflector

Acoustic waves generated in a SAW with a standard IDT structure travel in both forward and reverse directions and induce streaming in both directions, leading to the formation of a symmetrical butterfly streaming pattern, as shown in Fig. 7.6(a). However, this is not an optimal condition for microfluidic applications, as a directional pumping or mixing is needed in most cases. Half of the acoustic energy in a standard SAW-based microfluidics is therefore wasted. It would be a desirable situation for microfluidic applications that the SAW device has a unidirectional transmission capability. This can be achieved using some modified IDT structures, such as a split gate and SPUDT (single phase unidirectional traverse) or IDT with reflection electrode [20, 21]. SAW devices with reflectors have been fabricated and their effects on streaming have been studied. Figure 7.7 provides a comparison of the transmission spectra from the SAW devices with and without the reflection electrode. Both the devices have 60 pairs of fingers (N_1), 32 μm wavelength and 4.8 mm delay line. The reflector consists of $N_2=20$ pairs of fingers. The acoustic waves in the reverse direction are reflected by the periodic reflector electrode and have a phase shift of 2π , adding to the forward-traveling waves in phase, thereby leading to an enhanced transmission of forward-traveling acoustic waves. The results show an enhanced amplitude of the transmission signal by 6.5 dB when the reflector was used. The improved transmission signal has a profound effect on the flow velocity and

streaming pattern. The streaming velocity has been increased by 20~30% compared to those without the reflectors. As predicted before, figures 7.6(a) & (b) are a schematic comparison of the observed streaming patterns induced by SAWs with and without a reflector. The butterfly pattern of the flow becomes asymmetric once the reflector is used, leading to a flow that is dominated by the forward direction, owing to the increased coupling of energy in that direction. Typically, an improvement in streaming velocity of 20~30% can be obtained by using the reflector IDT structures. Further improvement can be made by using a semi-circular IDT structure that focuses acoustic waves on a point, and is consequently able to deliver a much higher streaming velocity [22].

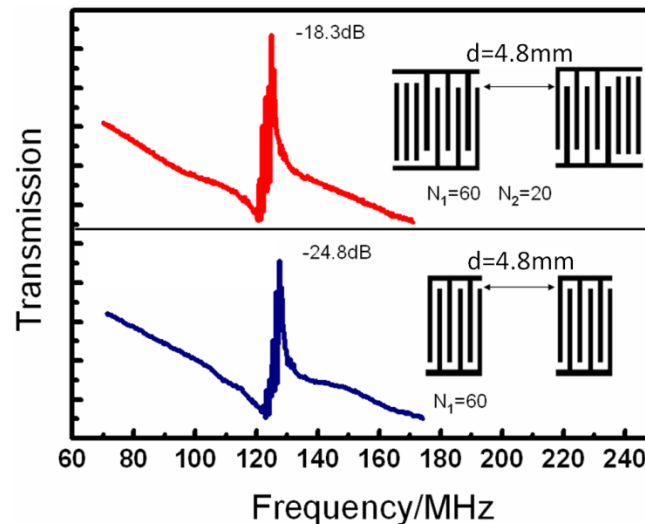


Figure 7.7 Comparison of the transmission signal for SAW devices with different IDT patterns. Both devices had a wavelength of $\lambda=32\mu\text{m}$

7.2 Steaming within a droplet on ZnO/Si

The performance of the LiNbO₃ SAW was fully demonstrated. The LiNbO₃ SAW device has been proved to be effective for mixing and droplet movement. In this section, we will demonstrate acoustic streaming using SAW devices made on ZnO thin films. The work focuses on the effects of ZnO film thickness and SAW wave mode on the liquid streaming and pumping. A novel SAW structure design is proposed and demonstrated based on a ZnO-island structure, which is considered to be promising for microfluidic and lab-on-a-chip applications.

7.2.1 Streaming on ZnO/Si

Based on energy conservation, as in the LiNbO₃ SAW, once the acoustic wave is coupled into the liquid; it transfers the kinetic energy to the liquid. When the input RF signal voltage is above 0.5 V, liquid convection and internal streaming patterns can be clearly observed with the assistance of the added ink particles. The streaming velocity is measured and the process is repeated as was done on the LiNbO₃ SAW.

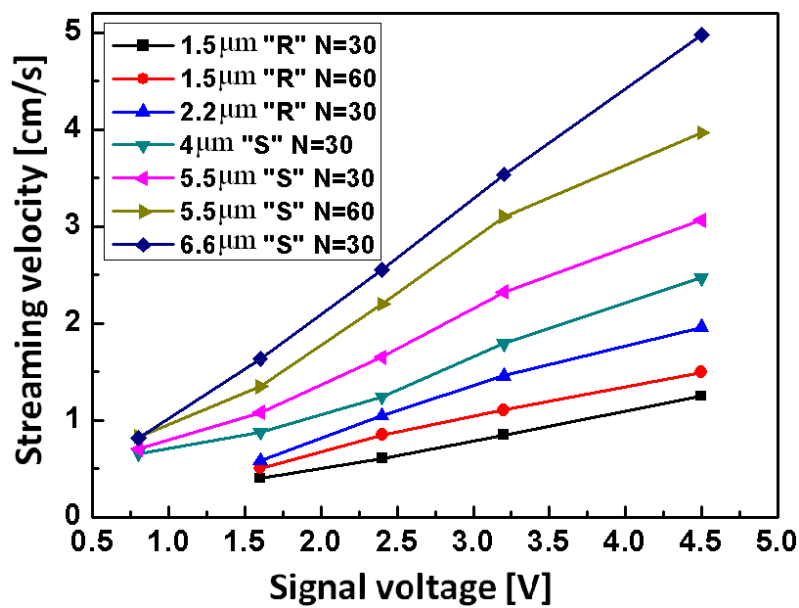


Figure 7.8 Flow (streaming) velocity as a function of signal voltage with IDT finger pair and wave mode as a parameter

It was observed that both the S- and R-mode (“S” and “R” stand for Sezawa and Rayleigh) waves can induce acoustic streaming with different streaming velocities, as shown in Fig.7.8. The streaming velocity induced by the S-wave is much higher than that induced by the R-wave in the same SAW device. Figures 7.9(a) & (b) show the dependence of the acoustic streaming velocity on RF signal voltage as functions of

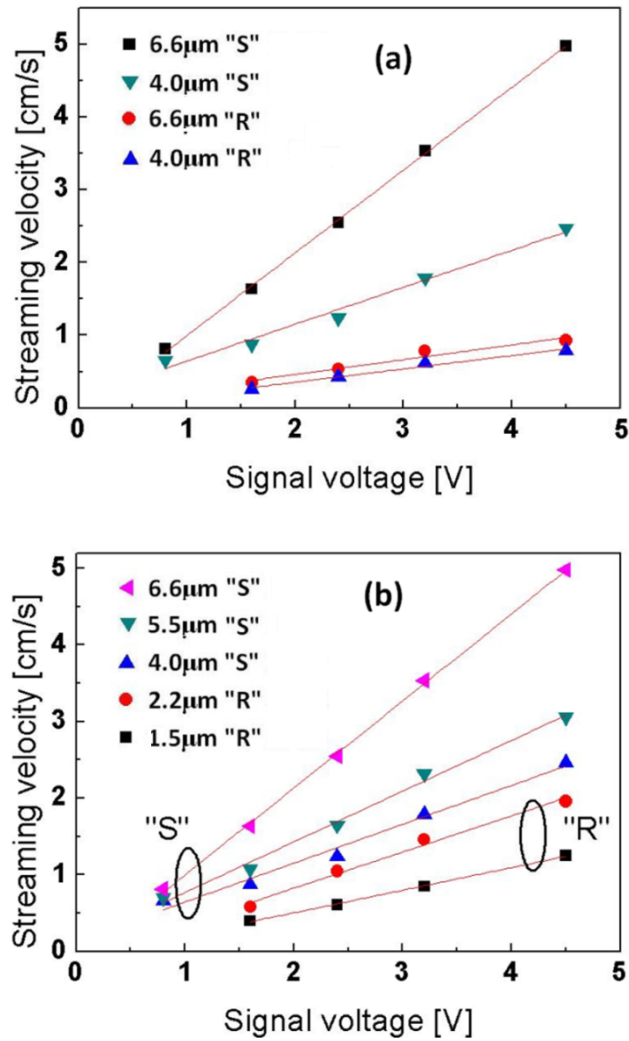


Figure 7.9 Streaming velocity as a function of signal voltage and their linear fitting. Comparison of streaming velocities induced by R- and S-waves (a) and in SAWs with different ZnO thicknesses (b)

IDT finger numbers and wave mode. The streaming velocity increases linearly with signal voltage for all the devices tested, and the velocity also increases with increase in film thickness at a fixed signal voltage. These are attributed to the increased amplitude of the transmitted Sezawa wave when the ZnO film thickness and the RF signal voltage increase. For the same device, the streaming velocity induced by the S-wave is typically 3~10 times that induced by the R-wave, owing to the larger amplitude of the resonant wave. The maximum streaming velocity obtained is 5 cm/s at a signal voltage of 4.5 V for the SAW on a 6.6 μm ZnO film. Although this is lower

than the 18 cm/s obtained from the LiNbO₃ SAW devices [22], it is still much higher than those of the most other micropumps, even if not all, and is more than enough for microfluidic applications. The results clearly show that the Sezawa mode waves have a high resonant frequency and large signal amplitude, which are suitable for high-frequency sensor and microfluidic system applications.

From the streaming experiment, one phenomenon observed is that the streaming is the fastest at the center frequency, while the streaming velocities slow down as the applied frequency of the signal voltage moves away from the resonant frequency as can be seen in Table 7.1.

Table 7.1 Range of frequencies that induce the streaming and performance of devices

Sample	Finger pair	Wave mode	Resonant frequency	Frequency range of streaming
1.5μm ZnO/Si	30	Rayleigh	136.1MHz	[133.6,138.7]MHz
1.5μm ZnO/Si	60	Rayleigh	138.5MHz	[136.6,142.8] MHz
2.2μm ZnO/Si	30	Rayleigh	128.2MHz	[126.0,130.4] MHz
4.0μm ZnO/Si	30	Sezawa	179.5MHz	[175.7,182.2] MHz
5.5μm ZnO/Si	30	Sezawa	173.0MHz	[169.7,176.5] MHz
5.5μm ZnO/Si	60	Sezawa	176.2MHz	[172.2,180.3] MHz
6.6μm ZnO/Si	30	Sezawa	160.2MHz	[157.3,162.9] MHz

This can be explained by the radiation conductance as a function of the applied frequency. According to the crossed-field model [23], the radiation conductance $G_a(f_r)$ of an acoustic wave at a center frequency f_r , can be expressed [24]:

$$G_a(f_r) = 8K^2 f_r C_T N \quad (7.2)$$

where N is the number of the electrode pairs in the IDT (periods), $C_T = C_S N = C_1 W N$ is the total IDT capacitance (F), K^2 is the electromechanical

coupling coefficient, C_s is the capacitance of one finger pair (F), C_1 is the finger overlap capacitance per period and per unit length, and W is the IDT aperture. The value of C_1 can be found from the following expression [25]:

$$C_1 = 2(6.5\eta^2 + 1.08\eta + 2.37)\left(\frac{\varepsilon}{\varepsilon_o} + 1\right) \quad (7.3)$$

using the ZnO dielectric constant $\frac{\varepsilon}{\varepsilon_o} = 8.5$ and the metallization ratio for the

transducer $\eta=0.5 \Rightarrow C_1=117.9$ pF/m.

Eq. (7.2) can be also written as

$$G_a(f_r) = 8K^2 f_r C_s N^2 \quad (\text{mho}) \quad (7.4)$$

The equivalent characteristic admittance of G_o of the SAW transmission line is given as $G_o = K^2 f_r C_s$. This can be substituted into Eq. (7.4) to give the input radiation conductance as

$$G_a(f_r) = 8N^2 G_o \quad (\text{mho}) \quad (7.5)$$

For frequencies near the center frequency the Eq. above can be generalized as

$$G_a(f) \cong G_a(f_r) \left| \frac{\sin x}{x} \right|^2 \cong 8N^2 G_o \left| \frac{\sin x}{x} \right|^2 \quad (7.6)$$

where $x = N\pi(f - f_r)/f_r$ in the sinc function relation $\text{sinc}(x) = \sin(x)/x$. i.e.

$$G_a(f) \cong 8N^2 f_r N^2 C_1 \left| \frac{\sin(N\pi(f - f_r)/f_r)}{N\pi(f - f_r)/f} \right|^2 \quad (7.7)$$

Increasing the number of pairs, N of IDTs, converts more of the input RF signals to the mechanical waves. For example, for the Sezawa mode on the $5.5 \mu\text{m}$ ZnO/Si SAW, the resonant frequency f_r of the SAW is 173.0 MHz, $N=30$, $K^2 \approx 4\%$. The simulation result of the conductance of the Sezawa wave on Matlab is shown below:

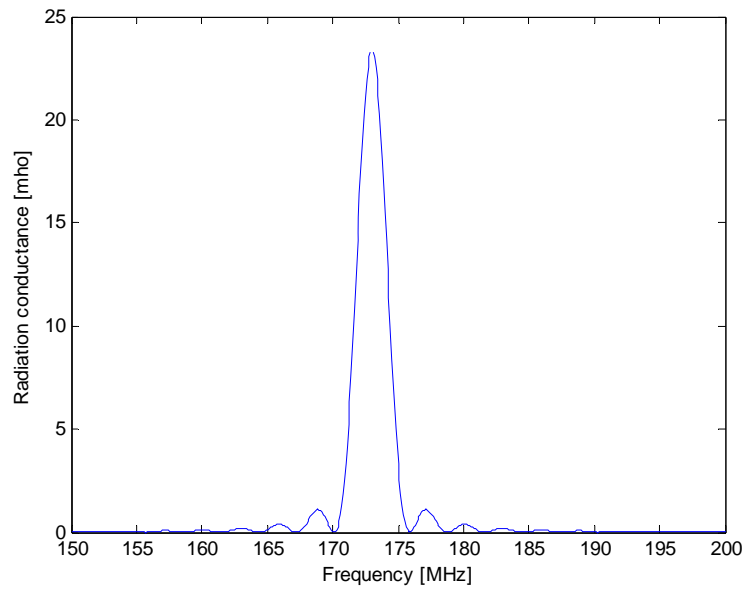


Figure 7.10 The radiation conductance as a function of the frequency

The simulation of the radiation conductance $G_a(f)$ shows that the value $G_a(f)$ is a maximum at the central frequency, and that the value of $G_a(f)$ is close to zero at all non-central frequencies. At the center frequency, the RF signals are converted to the SAW that propagates. At the non-central frequencies, $G_a(f)$ is much smaller than at the central frequency, and almost no SAW can be excited by the IDTs.

That is why the liquid only streams within a small range around the center frequency. At the center frequency 173.0 MHz, $G_a(f)$ is 23.4 mho, and dramatically drops to 7.127×10^{-3} mho at 172 MHz. Further away from the center frequency, the value of the radiation conductance oscillates and decreases to zero.

The Sezawa mode possesses a higher electromechanical coupling coefficient $K^2 \sim 4\%$ [26], compared with that of the Rayleigh mode ($K^2 \sim 0.49\%$ [27]), which is consistent with our results. Additionally, the operating frequency f_r of the Sezawa mode is higher than that of the Rayleigh mode. The results have clearly demonstrated that Sezawa-mode waves are more efficient for microfluidic applications.

In summary, the resonant frequencies and the streaming velocities of the ZnO/Si structures were found to depend significantly on the thickness of the ZnO film. The signal amplitude of the Sezawa wave is much stronger than that of the Rayleigh-mode wave. Both the Rayleigh- and Sezawa-mode waves can be used to induce liquid streaming. The streaming by the Sezawa wave is much stronger than that induced by the Rayleigh wave, due to its higher resonant frequency and larger electromechanical coupling coefficient.

Streaming on the ZnO island

Figure 7.11 shows the streaming velocities within a water droplet, driven by the acoustic waves generated by SAW devices on “ZnO islands” with different thicknesses. The ZnO island structure is shown in Fig. 6.15 in Chapter 6. As with those obtained from the normal SAWs as shown in Fig.7.8 [28], the streaming velocity increases with the RF signal voltage linearly, and the value is larger for a thicker ZnO SAW. However, it should be pointed out that the streaming velocities decrease by ~60% after removing the ZnO layer. Nevertheless, the results have clearly demonstrated the feasibility using this novel structure to construct lab-on-a-chip or microfluidics with active piezoelectric material isolated from other components. Although details for this structure are yet to be investigated, the results have demonstrated the potential usefulness for future applications.

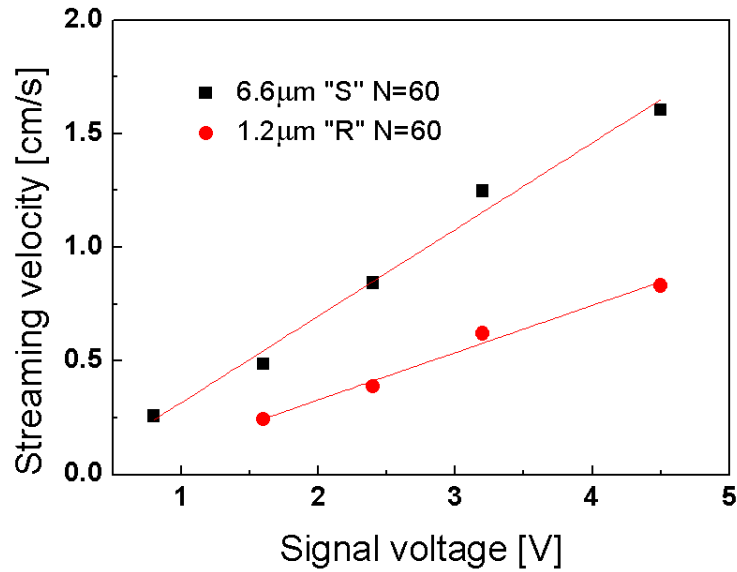


Figure 7.11 Streaming velocity induced by acoustic waves from the SAW devices on the ZnO islands with different thicknesses. The dependence of streaming velocity in this structure is very similar to that obtained from a normal ZnO SAW device

7.3 Conclusions

- For LiNbO₃ devices, both first and third harmonic waves demonstrated the ability to induce streaming using the acoustic wave.
- The fundamental wave exhibits a high mixing capability for streaming within a droplet.
- The streaming velocities of the ZnO/Si structures were found to significantly depend on the thickness of the ZnO film.
- Both the Rayleigh and Sezawa mode waves can be used to induce liquid streaming. The streaming by the Sezawa wave is much stronger than that induced by the Rayleigh wave due to its higher resonant frequency and larger electromechanical coupling co-efficient.

Reference

- ¹ M.J. Vellekoop. “Acoustic-wave devices and their technology”. *Ultrasonics*, 36 (1998) 7.
- ² S. Shiokawa; J. Kondoh. “Surface Acoustic Wave Sensors”. *Jpn, J. Appl. Phys.* 43 (2004) 2799.
- ³ E. Gizeli. “Design considerations for the acoustic waveguide biosensor Smart”. *Mater. & Struct.* 6 (1997) 700.
- ⁴ K.Sritharan, C.J.Strobl, M,F.Schneider, and A.Wixforth. “Acoustic mixing at low Reynold’s numbers”. *Appl. Phys. Lett.* 88 (2005) 054102.
- ⁵ N. T. Nguyen and Z. Wu. “Micromixers – A Review”. *J. Micromech. Microeng.* 15 (2005) R1.
- ⁶ U. Drechsler, N. Bürer, M. Despont, U. Dürig, B. Gotsmann, F. Robin and P. Vettiger. “Cantilevers with nano-heaters for thermomechanical storage application”. *Microelectron. Eng.* 67-68 (2003) 397.
- ⁷ M.K.Tan, J.R. Friend and L. Y. Yeo. “Surface acoustic wave driven microchannel flow”. *Proc. of 16th Australasian Fluid Mechanics Conf. Queensland, Australia, Dec.* (2007) pp.790.
- ⁸ W. K. Tseng, J. L. Lin, W. C. Sung, S. H. Chen and G. B. Lee. “Active micro-mixers using surface acoustic waves on Y-cut 128° LiNbO₃”. *J. Micromech. Microeng.* 16 (2006) 539.
- ⁹ Y. Chen, T. Wu and T. Chou. “Analysis of the frequency response of a dispersive IDT/ZnO/Sapphire SAW filter using effective permittivity and coupling of modes model”. *J.Phys.D:Appl.Phys.* 37 (2004) 120.
- ¹⁰ G. G. Yaralioglu, I. O. Wygant, T. C. Marentis and B. T. Khuri-Yakub. “Ultrasonic mixing in microfluidic channels using integrated transducers”. *Anal. Chem.* 76 (2004) 3694.
- ¹¹ V. Vivek, Y. Zeng, and E. S. Kim. “Novel acoustic-wave micromixer”. *Proc. MEMS’00, 13th IEEE Int. Workshop Micro Electromechanical System (Miyazaki,*

Japan) (2000) 668.

¹² S. Shiokawa, Y. Matsui and T. Moriizumi. “Experimental study on liquid streaming by SAW”. *Jpn. J. Appl. Phys.* 28, Suppl.28 (1989) 126.

¹³ A. Wixforth. “Acoustically driven planar microfluidics”. *Superlattices & Microstruct.* 33 (2003) 389.

¹⁴ S. Shiokawa, Y. Matsui, and T. Morizumi. “Experimental study on liquid streaming by SAW”. *Jpn. J. Appl. Phys.* 28 (1989) 126.

¹⁵ T. Koga and M. Morita. “Dependence of the Molecular Aggregation State of Octadecylsiloxane Monolayers on Preparation Methods”. *Langmuir.* 21 (2005) 905.

¹⁶ H. L. Bertoni and T. Tamir. “Unified theory of Rayleigh-angle phenomena for acoustic beams at liquid-solid interfaces”. *J. Appl. Phys.* 2 (1973) 157.

¹⁷ S. Shiokawa, Y. Matsui and T. Morizumi. “Study on SAW streaming and its application to fluid devices”. *Jpn. J. Appl. Phys.* 29 (1990) 137.

¹⁸ M. I. Newton, M. K. Banerjee, T. K. H. Starke, S. M. Bowan and G. McHale. “Surface acoustic wave–liquid drop interactions”. *Sens. Actuat. A.* 76 (1999) 89.

¹⁹ K. Chono, N. Shimizu, Y. Matsui, J. Kondoh and S. Shiokawa. “Development of novel atomization system based on SAW streaming”. *Jpn. J. Appl. Phys.* 43 (2004) 2987.

²⁰ D. Royer, E. Dieulesaint. “Elastic waves in Solids I” (Springer, New York, 1999).

²¹ D. Royer, E. Dieulesaint. “Elastic waves in Solids II” (Springer, New York, 1999).

²² X.Y. Du, M. Swanwick, Y.Q. Fu, J.K. Luo, A.J. Flewitt, D.S. Lee, S. Maeng and W.I. Milne, submitted to *J. Micromech. Microeng.*

²³ D. Powell, K. Kalantar and W. Wlodarki. “Numerical calculation of SAW sensitivity: application to ZnO/LiTaO₃ transducers”. *Sens. Actuat. A* 115 (2004) 456.

²⁴ C.K. Campell. *SAW for Mobile and Wireless Communications*, Academic Press, San Diego, 1998.

²⁵ I. Tang, H. Chen, M. Houngh and Y. Wang. “A novel integrable surface acoustic wave notch filter”. *Solid State Electronics.* 47 (2003) 2063.

²⁶ L. Le Brizoual, O. Elmazria, F. Sarry and M. El Hakiki. “High frequency SAW

devices based on third harmonic generation”. *Ultrasonics*. 45 (2006) 100.

²⁷ G. Bu, D. Ciplys, M. Shur, L. J. Schowalter, S. Schujman and R. Gaska. “Electromechanical coupling coefficient for surface acoustic waves in single-crystal bulk aluminum nitride”. *Appl. Phys. Lett.* 84(Issue 23) (2004) 4611.

²⁸ X.Y. Du, Y.Q. Fu, S.C. Tan, J.K. Luo, A.J. Flewitt, W.I. Milne, D.S.Lee, S.Maeng, S.H.Kim, N.M.Park, Y.J.Choi, J.Park and Y.J.Choi. “ZnO film thickness effect on surface acoustic wave modes and acoustic streaming”. *Appl. Phys. Lett.* 93 (2008) 094105.

Chapter 8. Droplet Manipulation by SAW

When the acoustic wave encounters liquid on its path, its kinetic energy and momentum are coupled into the liquid, according to the energy conservation principle. Three situations were observed:

- 1) If the surface is hydrophilic and the acoustic force is low, liquid convection and internal streaming are induced.
- 2) When the acoustic force increases continuously and reaches a threshold, tiny droplets with volumes ranging from a few femtolitres to a few picolitres are ejected from the liquid to form a mist (atomization).
- 3) If the surface is hydrophobic and the acoustic force is large enough, droplet motion is induced.

The energy and the momentum of the longitudinal wave transferred into the liquid are useful for liquid pumping and mixing. It has been reported that on a LiNbO₃ substrate, a liquid droplet interacting with the acoustic wave will absorb the energy and the momentum of the SAW, thus causing the liquid to stream, move, and eject (atomisation) upon gradual increase of the SAW amplitudes [1, 2, 3, 4]. A net pressure gradient, P_{saw} , forms in the direction of the acoustic wave propagation and provides an effective force to drive the liquid, which can be described using Eq.(8.1) [5]:

$$P_{saw} = \rho_o v_s^2 \left(\frac{\Delta\rho}{\rho_o} \right)^2 \quad (8.1)$$

where ρ_o is the liquid density and $\Delta\rho$ is the slight density change due to the acoustic

pressure. Based on the acoustic streaming effect, micropump and micromixer systems [6, 7, 8, 9], droplet-positioning and manipulation systems [10, 11], atomization systems [12], fluidic dispenser arrays [11] and acoustic ejectors [13] have been proposed and developed.

This section will deal with how the SAW based on both the LiNbO₃ and ZnO/Si substrate induces acoustic force and droplet pumping, and will focus on the effects of the wave mode and surface modification on the acoustic force and pumping efficiency.

8.1 Contact angle and surface energy introduction

Contact angle, θ , is a quantitative measure of the wetting of a solid by a liquid. It is determined by the interfacial energies of the liquid/solid, γ_{SL} , solid/vapour, γ_{SV} , and vapour/liquid, γ_{LV} , as described for flat surfaces in Young's equation (Eq. (8.2)). At room temperature, the surface tension of water in contact with air, is $\gamma_{LV} = 7.2 \times 10^{-2}$ N/m.

$$\cos \theta = \frac{\gamma_{SV} - \gamma_{SL}}{\gamma_{LV}} \quad (8.2)$$

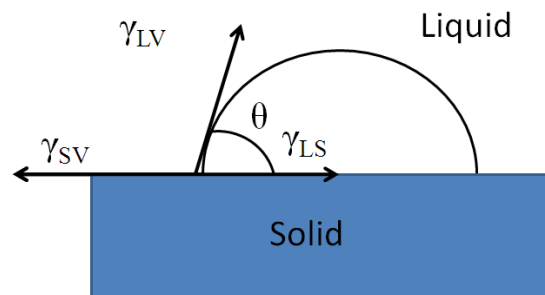


Figure 8.1 Three-phase equilibrium

In Fig. 8.1, low values of θ indicate that the liquid spreads, or wets well, while high values indicate poor wetting. If the angle θ is less than 90° the liquid is said to wet the solid. If it is greater than 90° it is said to be non-wetting. A zero contact angle represents complete wetting when the liquid forms a thin film.

8.2 Acoustic force by SAW devices on LiNbO₃ substrate

The shape of a water droplet on the surface of a substrate is determined by the surface energy or surface tension. It is a ball-like shape when the surface is hydrophobic, with a contact angle typically much larger than 90°, and is a cap-like shape when it is hydrophilic, with a contact angle smaller than 90°[14]. When the acoustic energy is coupled to the liquid droplet, it generates an acoustic pressure on the droplet. Therefore, as long as the SAW is excited with sufficient input RF power, the water droplet can be significantly pushed forward and deformed by the acoustic force in the wave-propagation direction, as shown in Fig. 8.2(b) on a hydrophilic surface. The leading edge contact angle, θ_2 becomes larger, while the trailing edge contact angle, θ_1 decreases. The acoustic force induced by the acoustic wave on the droplet can be estimated from the asymmetric contact angles and the droplet size. The contact angle hysteresis $\Delta\theta = \theta_2 - \theta_1$ is an important parameter when the droplet motion is taken into account. The acoustic force F_a is expressed by Eq.(8.3) [15, 16, 17]

$$F_a = 2R\gamma_{LV} \sin\left(\frac{\theta_1 + \theta_2}{2}\right)(\cos\theta_1 - \cos\theta_2) \quad (8.3)$$

where R is the radius of the droplet, γ_{LV} is the surface tension between the liquid and gas.

The droplet radius can be calculated from droplet volume, V (Eq. (8.4)) and the static contact angle, θ , assuming a spherical droplet shape under static conditions. The droplet is marked by the shaded area in Fig. 8.2(a) and H is the height of the droplet.

$$V = \frac{1}{3}\pi(3R - H) \times H^2 \quad (8.4)$$

$$R = \sqrt[3]{\frac{3V}{\pi(1 - \cos\theta)^2(2 + \cos\theta)}} \quad (8.5)$$

where $H = R(1 - \cos\theta)$. Given $V=10 \mu\text{l}$, it is easy to calculate the droplet radius to be $R \sim 2 \text{ mm}$ for a contact angle of 75° which is the typical contact angle on a bare LiNbO₃ substrate. Initially, the acoustic wave could only induce streaming. As the

signal voltage increases (roughly higher than 25V), the droplet starts to be deformed with a visible asymmetrical shape. Figure 8.2(b) shows the picture of a deformed droplet under the acoustic radiation pressure at a signal voltage of 45 V with an asymmetrical contact angle of $\theta_1=45.5^\circ$ and $\theta_2=97.6^\circ$. Using Eq. (8.3), the acoustic force applied to the droplet can be calculated to be 0.224mN. Two assumptions are made in the force estimation:

- The interfacial energy between water and air, γ_{LV} , is equal to 7.2×10^{-2} N/m [18, 19].
- The droplet is spherical.

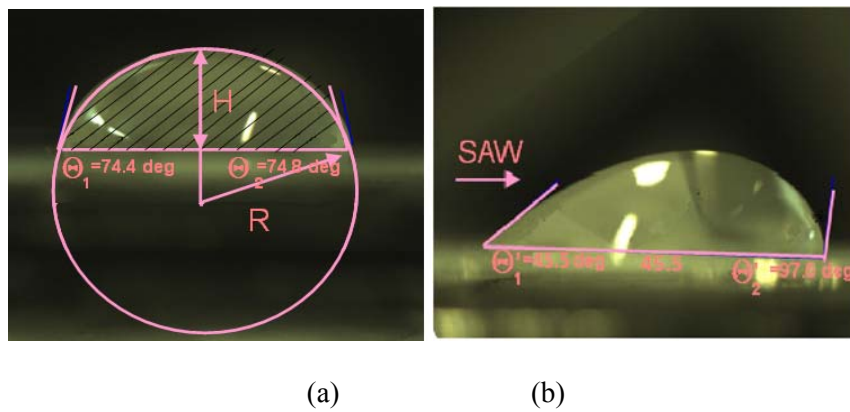


Figure 8.2 Side view of a $10 \mu\text{l}$ droplet on the LiNbO_3 surface (a): the droplet at rest, the contact angle: 75° . (b): the droplet deformed under an acoustic pressure from the left side

The acoustic forces produced by the signal voltage us calculated using Eq.(8.3) and are listed in Table 8.1.

Table 8.1 Trailing and leading edges contact angles as a function of signal voltage

Signal voltage	Trailing edge contact angle θ_1	Leading edge contact angle θ_2	Acoustic force F_s
0	74.4°	74.8°	0
30 V	59.4°	81.2°	0.095mN
35 V	54.7°	88.5°	0.148mN
40 V	50.2°	93.4°	0.189mN
45 V	45.5°	97.6°	0.224mN

Figure 8.3 shows the dependence of acoustic force generated by the Rayleigh wave as a function of RF signal voltage for the device with $N=60$ and $\lambda=32 \mu\text{m}$. The acoustic force increases with voltage applied, and slightly deviates from a linear relationship. This deviation is believed to be caused by the temperature-induced resonant frequency shift at high input powers, as will be discussed later. The 3rd harmonic-mode wave was found to be unable to produce sufficient acoustic force to deform the droplet at signal voltages $<45\text{V}$, which again indicates clearly that the fundamental wave is better than the 3rd harmonic-wave mode for microfluidic application.

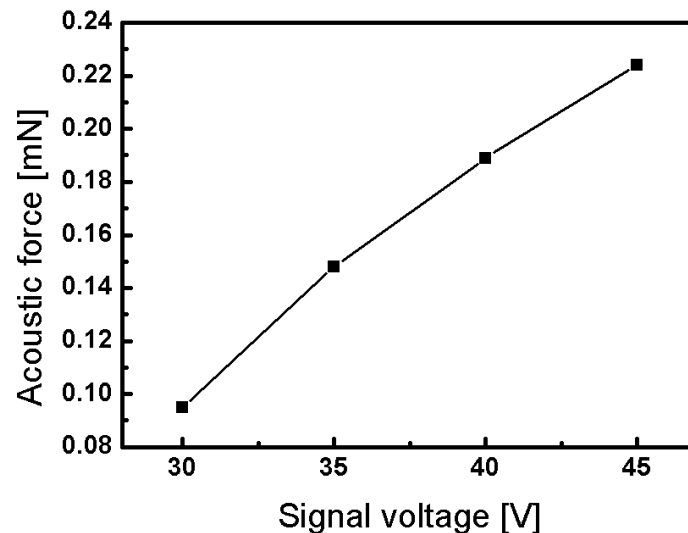


Figure 8.3 The acoustic force acting on $10 \mu\text{l}$ droplet obtained from Device B at a fixed centre frequency of 124MHz, plotted as a function of input voltage

The acoustic pressure acting on the droplet can be roughly estimated by $p=F/A$ (where A is the largest cross section of the droplet). The acoustic pressure applied on a droplet on an open surface is roughly ~ 80 Pa, comparable to some pressures obtained in mechanical micropumps. However, the surface force acting on a water droplet on an untreated LiNbO_3 surface, $\gamma_{LV}(1+\cos\theta)\times 2\pi R\sin\theta$ [20], is roughly ~ 1.08 mN, much larger than the maximum acoustic force generated by the Rayleigh wave; the droplet therefore remains on the surface without being moved forward. To manipulate the droplet on the channel-less flat surface, the surface of the SAW device substrate must be made hydrophobic, in order to reduce the surface energy, hence the surface force.

8.2.1 Hydrophobic Coating Surface treatment

In order to make a droplet-based micropump work effectively and efficiently, a hydrophobic coating is required to minimize the required force to move the droplet and maximize the contact angle. There are many possible ways to create hydrophobic surfaces, including surface coating, physical surface modification, and chemical modification [21]. This project focuses on surface coating technique to increase the surface hydrophobicity and reduce the droplet sliding force.

Polytetrafluoroethylene (PTFE) coating

This surface coating utilizes the hydrophobic polytetrafluoroethylene (PTFE) polymer for both its chemical inertness and bio-compatibility. The project developed a process to spin-coat the PTFE on the substrate while keeping the surface roughness low. PTFE reduces both surface energy and the force needed to move a droplet.

The procedure of the experiment is to place a droplet of D.I. water on a flat surface and measure the contact angle. The contact angle measurements are captured by a Motic MCCamera CCD USB digital camera using Motic Images Plus 2.0 software at 2 mega-pixels resolution. The samples are placed on a multi-adjustable platform and taped on the edge. A calibrated adjustable pipette accurately dispensed D.I. water on

the samples. The images are captured immediately after being dispensed and without intense light sources, to minimize any evaporation effects on the data.

The PTFE used for hydrophobic-coating is in liquid form and was spun on to the LiNbO_3 substrates. The general parameters for all samples were spin-coating at 600 RPMs for 6 seconds and then 4000 RPMs for 30 seconds with a soft bake at 150°C for 2 minutes. The hard bake temperature of 250°C and period of 20 minutes were used on a standard hotplate. The average film thickness for the samples of PTFE on LiNbO_3 was approximately $1.4\ \mu\text{m}$. All thickness measurements were carried out using a Dektak profilometer. The surface roughness for these samples varied from 50 nm to 100 nm root mean square (RMS). However, $1.4\ \mu\text{m}$ PTFE thickness on LiNbO_3 was found to be too thick. Therefore, the liquid PTFE emulsion was thinned 1:1 with DI water and the spin speed was increased to 6000 RPMs. The result was an average thickness of 220 nm and reduced roughness of 20 – 50 nm RMS.

A contact angle between 118° to 128° was observed for all of the PTFE samples, listed in Table 8.2. Figure 8.4 shows an image of a $10\ \mu\text{l}$ droplet on the PTFE coated surface. These figures are higher than those in most previous literature, in which contact angles for PTFE between 104° and 120° have been reported [22, 23, 24, 26].

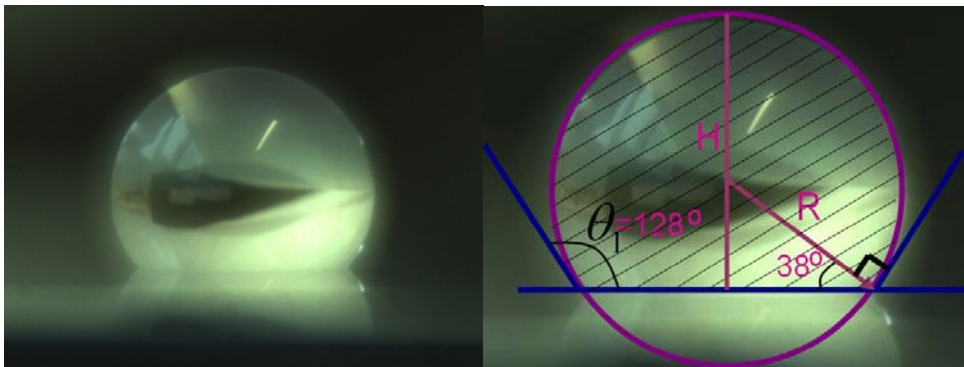


Figure 8.4 Contact angle of $10\ \mu\text{l}$ Droplet and PTFE/ LiNbO_3 hard-baked at 300°C for 20 minutes

Table 8.2 Contact angles for D.I. water droplets of different sizes

D.I. Water volume	Baking temperature	Baking time	Contact angle
10 μ l	300°C	20min	128°
10 μ l	250°C	20min	124°
10 μ l	300°C	1hr	125°
10 μ l	250°C	1hr	126°
20 μ l	300°C	20min	123°
20 μ l	250°C	20min	121°
20 μ l	300°C	1hr	123°
20 μ l	250°C	1hr	118°

The surface treatment of PTFE greatly increases the contact angle. The PTFE-coated surfaces had an average contact angle of approximately 123° for the droplet. The high surface roughness helps to achieve a high contact angle. However, on the other hand, high roughness is not good for droplet pumping.

The results also showed that both the baking time and the baking temperature had little effect on the contact angles of the droplets, although a minimum temperature was required to fully harden the PTFE.

Table 8.3 The parameters of the 10 μ l droplet with and without PTFE coating

	Bare LiNbO ₃ surface	LiNbO ₃ surface with PTFE coating	Equation
Contact angle θ	75°	128°	
Radius R	1.97 $\times 10^{-3}$ m	1.63 $\times 10^{-3}$ m	$V = \pi (3R - H) \times H^2 / 3$
Adhesion work	9.06 $\times 10^{-2}$ N/m	2.76 $\times 10^{-2}$ N/m	$\gamma_{LV}(1 + \cos\theta)$
Surface force F_s	1.08mN	0.226mN	$\gamma_{LV}(1 + \cos\theta) \times 2\pi R \sin\theta$

In Table 8.3, V is the droplet volume; R and H are the radius and height of the droplet, respectively. γ_{LV} represents the surface energy between the air and liquid (N/m) and θ is the contact angle of the droplet (deg). The work of adhesion is constant, and can be

estimated using the equation $\gamma_{LV}(\cos\theta + 1)$ [25]. The force required to actuate the droplet must be greater than the force between the substrate and the droplet. As the circumference along the interface of the droplet is $2\pi R\sin\theta$, the force F_s to overcome the surface energy for droplet moving is $\gamma_{LV}(\cos\theta + 1) \times 2\pi R\sin\theta$.

The results from the PTFE coating show a dramatic increase in contact angle versus an untreated surface, and a reduction in actuation force of a DI water droplet (Table 8.3). The surface force acting on a water droplet on an untreated LiNbO_3 surface is roughly 1.08 mN, whereas after the PTFE surface treatment, the force needed to actuate the droplet decreases greatly to 0.19 mN, making the droplet movement on the SAW device feasible.

PTFE looks like a good candidate for the SAW micropumps, because of the high contact angle and relatively low surface energy. However, there are several problems that should be overcome to make this happen, including excessive damping of the acoustic wave, poor adhesion and large-contact-angle hysteresis.

Poor adhesion has been found to be a problem with all the trials of PTFE coatings. If the DI water droplet was placed over a defect or on the edge of the PTFE- LiNbO_3 interface, the droplet would spread under the PTFE, thus removing the coating from the surface. Moreover, the PTFE coating can be as thick as ~ 200 nm, and thus can significantly dampen the SAW, leading to a small transmission signal amplitude and force for fluidic applications. Different methods will continue to be investigated for better surface treatment.

Octadecyltrichlorosilane (OTS) coating

As discussed above, the PTFE coating has several disadvantages, such as high roughness and poor adhesion. What is worse, the thick PTFE coating dampens most of the SAW energy. As a result, it is impossible to use it in pumping applications. To

solve this problem, a surface treatment that reduces the force required to actuate a droplet needs to be hydrophobic, homogeneous, smooth and not acoustically absorbent. Octadecyltrichlorosilane (OTS) is a suitable coating for this application. OTS was chosen for this experiment because the octadecyl chain ($C_{18}H_{37}$) is compact, and can form a hydrophobic self-assembled monolayer (SAM) with a large contact angle with water [26] and without negative effects on the acoustic properties of the surface.

The process of the OTS SAM layer formation includes drying the sample and immersing it in a toluene solution of OTS (concentration, 0.01mmol/L) at room temperature for 6 hours and then baking it for 1 hour at 125°C. However, in this process, it was found that the aluminum electrodes were corroded by the solution [27], as shown in Fig. 8.5. To solve this problem, the electrodes were covered with photoresist (AZ5214E) to avoid the aluminum electrode's corrosion by the OTS solution during the SAM layer formation. Once the SAM formation was complete, the photoresist was removed by immersing the samples in acetone for about one minute. The OTS SAM layer is not affected by acetone.

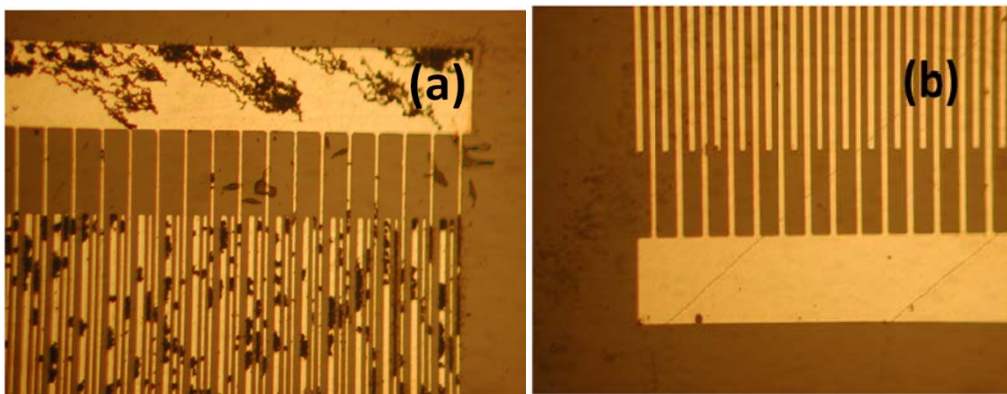


Figure 8.5 (a) the IDT after 6 hours in the 0.01mmol/L OTS toluene solution (b) the IDT after 6 hours in 0.01mmol/L OTS toluene solution with AZ5214E coating [27]

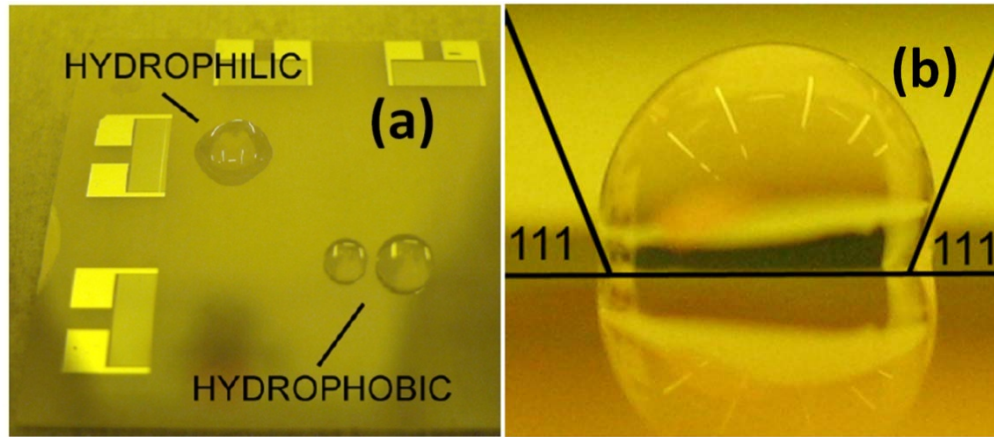


Figure 8.6 (a) Photograph showing difference in hydrophobicity of LiNbO₃ SAW device (b) Contact angle of OTS LiNbO₃ SAW coated devices

The OTS coating layer was found to increase the water contact angle on the SAW devices dramatically [28, 29, 30, 31], from $\sim 75^\circ$ on an untreated LiNbO₃ surface to up to $\sim 111^\circ$ after treatment as shown in Fig.8.6. This, in turn, reduces the droplet sliding force significantly. The contact angle, droplet shape and surface force on both the bare surfaces and OTS treated LiNbO₃ surfaces are listed in Table 8.4.

Table 8.4 Parameters of 10 μ l droplet before and after the OTS surface treatment

	Bare LiNbO ₃ surface	LiNbO ₃ surface with OTS coating	Equation
Contact angle θ	75°	111°	
Radius R	1.97x10 ⁻³ m	1.44x10 ⁻³ m	$V=\pi(3R-H)xH^2/3$
Height H	1.46x10 ⁻³ m	1.99x10 ⁻³ m	$H=R(1-\cos\theta)$
Adhesion work	9.06x10 ⁻² N/m	4.62x10 ⁻² N/m	$\gamma_{LV}(1+\cos\theta)$
Surface force F_s	1.08mN	0.379mN	$\gamma_{LV}(1+\cos\theta)x2\pi R\sin\theta$

The contact angle on the OTS is not as large as that of the PTFE coating, and consequently the force required to actuate the droplet on the OTS will be larger than that on the PTFE coated surface. Nevertheless, the OTS surface treatment has some remarkable advantages. For example, the OTS-treated surface of the SAW devices is very stable. It remains hydrophobic with the same contact angle even after weeks, implying excellent stability for the OTS layer. The OTS coating also exhibits

excellent uniformity and good adhesion to the substrate. The average thickness of the OTS coating is less than 10nm, and the acoustic damping by this coating is negligible.

Overall, OTS is a better choice for the SAW micropumps because of its high contact angle and relatively low surface energy. Most importantly, OTS is almost completely inert and bio-compatible, which is suitable for application in SAW-micropumps and mixing devices. OTS therefore will be used as the hydrophobic surface coating for SAW devices on LiNbO₃ as well as ZnO piezoelectric substrates hereafter.

8.2.2 Surface energy and the contact angle

On an untreated LiNbO₃ surface, the contact angle of a droplet is 75°. According to the equations derived above, the forces required to actuate droplets of different volumes are calculated for both untreated and OTS-treated LiNbO₃ substrates, as listed in Table 8.5 & 8.6.

Table 8.5 Parameters of droplets and surface force on the untreated LiNbO₃

Contact angle	Volume	Radius	Height	Contact area	Surface force
75°	10μl	1.9746x10 ⁻³ m	1.4612x10 ⁻³ m	0.1224cm ²	1.08mN
75°	5μl	1.5672x10 ⁻³ m	1.1617x10 ⁻³ m	0.0771cm ²	0.85mN
75°	2μl	1.1548x10 ⁻³ m	0.8558x10 ⁻³ m	0.0752cm ²	0.63mN
75°	1μl	0.9165x10 ⁻³ m	0.6795x10 ⁻³ m	0.0264cm ²	0.49mN
75°	0.5μl	0.7275x10 ⁻³ m	0.5391x10 ⁻³ m	0.0166cm ²	0.39mN

Table 8.6 Parameters of droplets and surface force on the OTS-treated LiNbO₃

Contact angle	Volume	Radius	Height	Contact area	Surface force
111°	10μl	1.4414x10 ⁻³ m	1.958x10 ⁻³ m	0.0652cm ²	0.39mN
111°	5μl	1.144x10 ⁻³ m	1.554x10 ⁻³ m	0.0411cm ²	0.309mN
111°	2μl	0.8476x10 ⁻³ m	1.151 x10 ⁻³ m	0.0226cm ²	0.229mN
111°	1μl	0.6807x10 ⁻³ m	0.9246x10 ⁻³ m	0.0145cm ²	0.184mN
111°	0.5μl	0.5403x10 ⁻³ m	0.7337x10 ⁻³ m	0.0092cm ²	0.146mN

The droplet shape on the OTS-treated surface is significantly different. The radius of the spherical droplet decreases while the height of the droplet increases after the surface treatment, indicating the change in the shape of the droplet, from cup-like to a ball-like. The contact area is also reduced, which is attributed to the decrease in surface force.

The surface force can be calculated by measuring the contact angle at a given volume of the droplet. It is interesting to investigate the relationship between the contact angle and the surface force. Moreover, for a fixed volume of the droplet, it would also be interesting to know at which contact angle the droplet can be moved by the SAW.

The relationship between the surface force (F) and the contact angle is

$$F = \gamma_{LV}(1 + \cos \theta) \times 2\pi R \sin \theta \quad \Rightarrow$$

From Eq. (8.3) & and Eq. (8.4),

$$F = K \times (1 + \cos \theta) \times \sin \theta \times \sqrt{\frac{1}{2 + \cos \theta} \times \frac{1}{(1 - \cos \theta)^2}} \quad (8.6)$$

where $K = 2\pi\gamma(\sqrt[3]{3V/\pi})$

K is a constant while the volume of the droplet remains the same. The relationship between F and the contact angle θ can be expressed as

$$F \sim (1 + \cos \theta) \times \sin \theta \times \sqrt[3]{\frac{1}{2 + \cos \theta} \times \frac{1}{(1 - \cos \theta)^2}} \quad (0^\circ < \theta < 180^\circ).$$

The relative surface force reduces significantly at contact angles below 40° , and decreases more gradually by increasing the contact angle. From Eq.(8.6), the constant K only depends on the volume of the droplet, and the unit of K is the same as the surface force (N). In the experiments, the volume of $1 \mu\text{l}$, $2 \mu\text{l}$, $5 \mu\text{l}$ and $10 \mu\text{l}$ were used. In Fig. 8.7, the surface force F_s as a function of the contact angle for the given droplet volume, is shown in Figure 8.7.

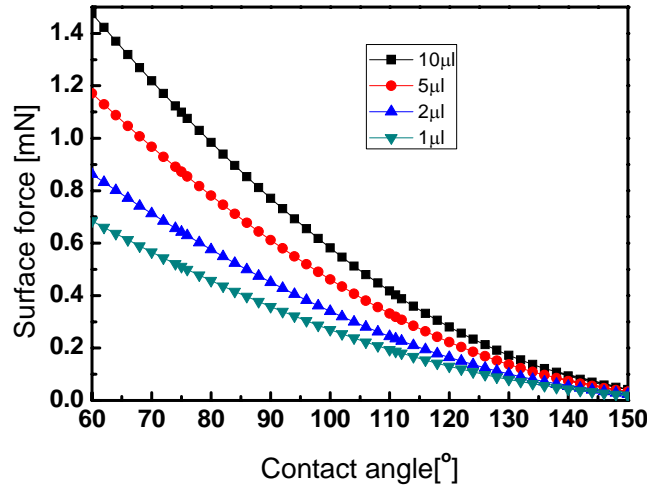


Figure 8.7 The enlarged figure of relative surface force as a function of the contact angle from 60° to 150°

8.2.3 Droplet manipulation by SAW on LiNbO_3 substrate

The goal of this research is to develop lab-on-a-chip with integrated micromixing, pumping and sensors. The device has satisfactorily demonstrated mixing droplets effectively. Droplet mixing occurs at lower voltages on untreated substrate surfaces. In this section the pumping ability of the SAW devices is investigated. As the RF voltage applied to the IDTs is increased, the acoustic wave amplitude increases. They induce a larger acoustic force which is required to be exerted on the droplet, thereby increasing the energy dissipated into the droplet. If this energy can make the droplet overcome the surface energy holding the droplet in place, the droplet will move away

from the activated IDT.

Figure 8.8 shows the droplet velocity as a function of signal voltage on an OTS-treated LiNbO₃ SAW device. The droplets were driven by the fundamental wave, $\lambda=32\ \mu\text{m}$ and $N=60$. The lines were created by linear fitting. It was found that the droplet can be propelled along the wave propagation direction by acoustic waves on the OTS-treated surfaces. Figure 8.8 shows the dependence of the droplet's velocity on the signal voltage applied to an OTS-treated LiNbO₃ SAW device with varying droplet sizes. The droplet velocity increases linearly with the signal voltage for all droplets, and reaches $\sim 1.4\ \text{cm/s}$ at a signal voltage of 40 V for a droplet of 1 μl . At a fixed signal voltage, small droplets move faster than larger ones. A droplet of 10 μl could not be moved when the signal voltage was below 35 V, and started to tremble at signal voltages above 40 V. It is interesting to compare Figs.8.3 and 8.8. In Fig. 8.3, the acoustic force generated at a signal voltage of 45 V is only sufficient to deform the droplet on an untreated surface, but insufficient to move the droplet. However, in Fig.8.8, once the surface is hydrophobic and surface tension is reduced, the acoustic force generated at a signal voltage of 40 V is large enough to move a droplet up to a size of 10 μl .

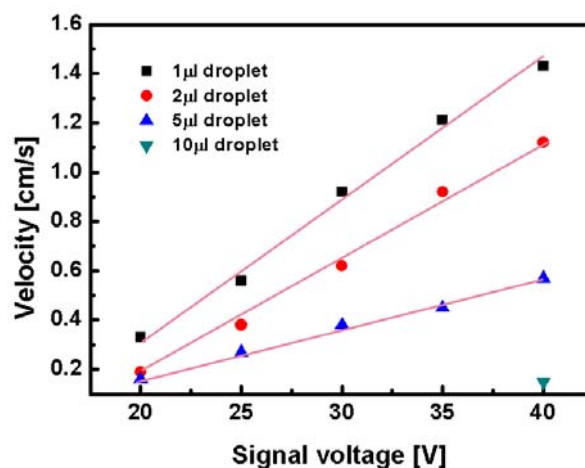


Figure 8.8 The droplet velocity as a function of signal voltage

Fig.8.9 shows a droplet of 1 μl before and after applying an RF signal with $V=40\text{V}$ for 0.5 sec. The droplet was moved by 4.5 mm in less than one second, and was stopped by the IDT electrode.

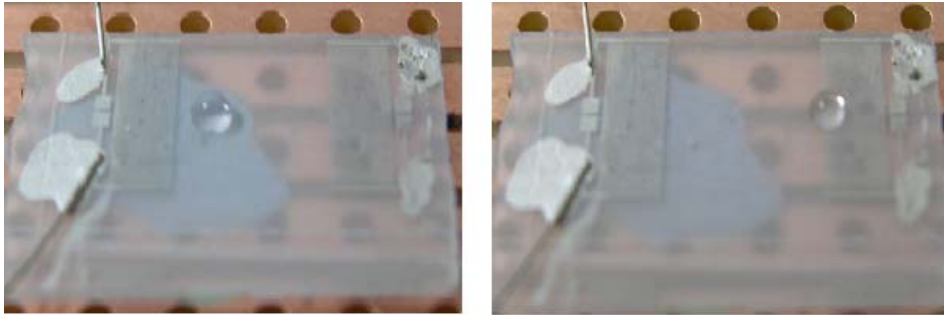


Figure 8.9 The 1 μl droplet movement induced by the SAW

8.2.4 Acoustic heat and RF pulsed voltage input

Acoustic heat

Acoustic heating is a common phenomenon in SAW devices [32, 33] and is caused by two mechanisms. The first one is the coupling of acoustic energy dissipated into the substrate material and from the wave propagating on the substrate surface. The other one is caused by lattice vibration. The propagating SAW generated by the mechanical vibrations in the piezoelectric film causes an internal strain. Although the displacement of the substrate surface is only a few nanometers in amplitude, the high-frequency vibration still causes heat generation, especially when there are usually many defects in the substrate material and surface. Acoustic heating will significantly affect the performance of acoustic streaming and pumping in some aspects. Firstly, raising the temperature shifts the resonant frequency of a SAW device, which is normally taken as a constant in SAW microfluidics. Secondly, it introduces errors in sensing using the SAW devices. Thirdly, it may compromise the integrity of the bio-substances being tested. In order to clarify these effects, the surface temperature of the SAWs was investigated in this section.

To understand the acoustic heating effect on the droplet, the temperature of the SAW

device during high RF voltage operation was measured. A thermocouple was placed directly near the IDT electrodes with no liquid droplet. The RF signal amplitude (at the resonant frequency) was varied from 10 V to 40 V and the temperature was recorded as shown in Fig. 8.10. It was found that the surface temperature increases slowly up to $\sim 80^{\circ}\text{C}$ if the RF signal with a voltage of 40 V is applied for 60 sec or more, but remains below 40°C if the RF input voltage is applied for less than 10sec. For RF signal amplitudes below 20 V, the temperature rise was not significant. The time taken by the temperature to become saturated is roughly 40~60 sec. In most of cases, pulsed RF voltage is used to pump liquid samples as temperature increase is undesirable. To investigate the time taken for the temperature to rise, a continuous RF voltage has been used.

For the measurement shown in Figs. 8.9, the temperature is estimated to be $\sim 30^{\circ}\text{C}$, sufficiently high to cause the shift of the intrinsic resonant frequency of the SAW devices by a few kilohertz. Therefore, as a matter of fact, the applied RF signal at a fixed frequency could shift slightly away from the intrinsic resonant frequency of the SAW devices.

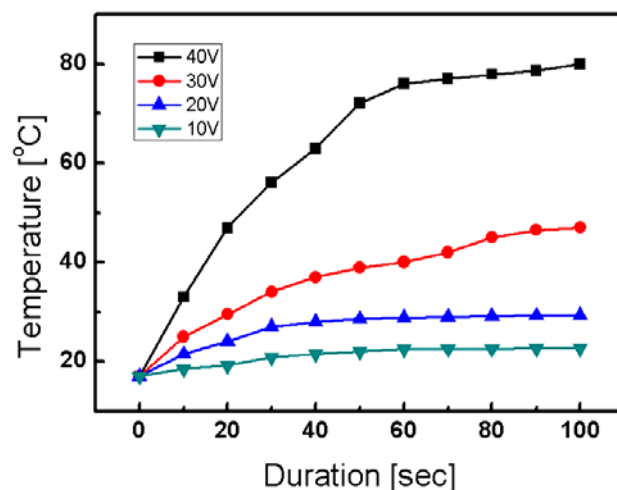


Figure 8.10 Temperature rise induced by acoustic heating on a LiNbO_3 SAW with a single-electrode IDT

Pulse microdroplet manipulation

Acoustic heating can be significantly reduced by using a pulsed RF signal. The surface temperature of the device was found to remain constant at room temperature as the pulse width increased up to 200 ms, and gradually increased up to 35°C when the pulse width was increased up to 600 ms. However, the maximum allowable pulse width is much lower than that of continuous RF signal pumping. This can be attributed to the surface heat dissipation during the off period of the signal.

Droplet motion distance can easily be controlled by pulsed RF signals. Figure 8.11 shows the dependence of the droplet moving distance with pulse number. In these experiments, a 1 μ l droplet was used. The droplet started to move when the applied RF input voltage was above 30 V. For a fixed signal voltage, the moving distance increased almost linearly with the pulse number. During the on-period of the voltage pulse, the droplet moved, while during the off period, the droplet remained stationary. A pulse width of 100 ms was used to avoid a temperature rise. From this droplet the moving distance produced by a single pulse can be estimated to be 86 μ m/pulse.

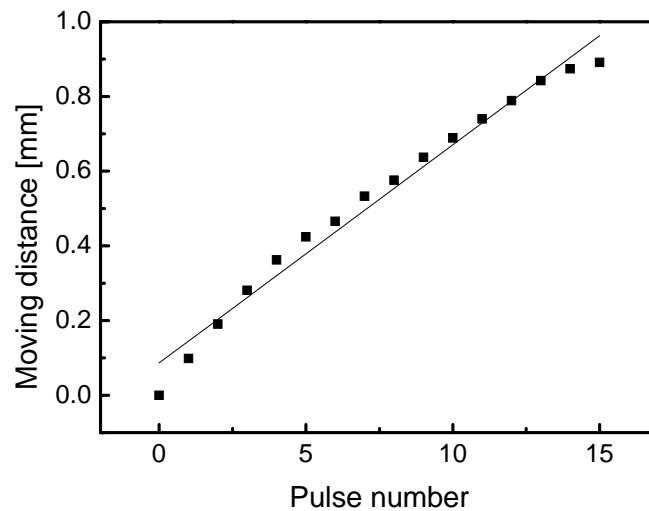


Figure 8.11 Moving distance of 1 μ l droplet from IDT in SAW propagation direction with width of 100ms RF pulses and signal amplitude of 30V

8.3 Droplet manipulation by SAW on ZnO/Si substrate

The LiNbO₃ SAW device has been proven to be effective for mixing and droplet movement. In this section, we will demonstrate acoustic pumping using the SAW devices made on ZnO thin films. The work focuses on the effects of ZnO film thickness and SAW wave mode on the liquid pumping.

8.3.1 Acoustic force by ZnO/Si SAW device

As in the LiNbO₃ SAW devices, the acoustic wave generates an acoustic pressure on the droplet. If the input power is sufficiently high and the surface is hydrophilic, the water droplet can be pushed forward by the acoustic force in the wave-propagation direction, and eventually becomes deformed from its original shape. The acoustic force, F_a , exerted by the acoustic wave on the droplet can be estimated from the asymmetric contact angles as discussed previously [34, 35, 36].

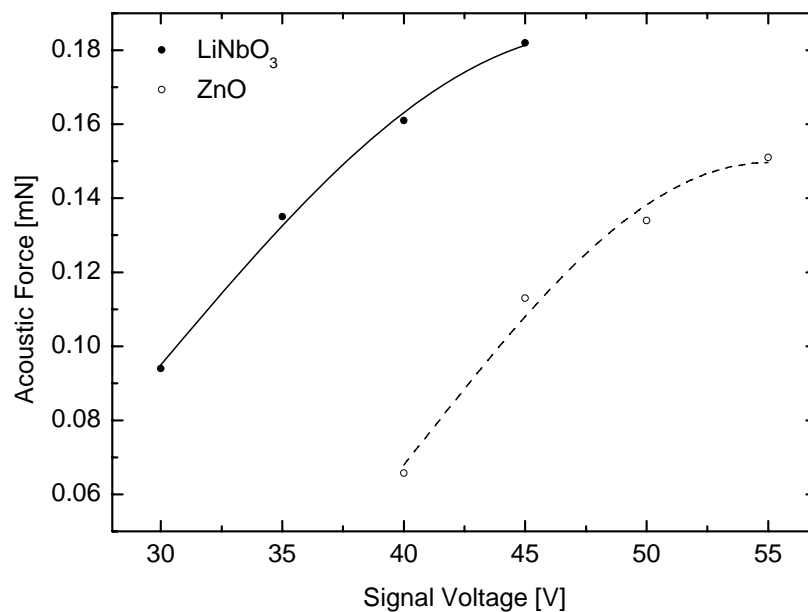


Figure 8.12 Acoustic force as a function of RF signal voltage applied to a 10 μ l droplet. The Rayleigh wave was used for the LiNbO₃ device, while the Sezawa wave was used for the 5.5 μ m ZnO SAW. Both devices had 60 finger pairs

Figure 8.12 shows the dependence of the acoustic force generated by the Sezawa wave as a function of RF signal voltage for the ZnO SAW devices, as well as the acoustic force produced by the Rayleigh wave from a LiNbO₃ SAW with the same device dimension and structure for the purpose of comparison. It should be pointed out that the Rayleigh wave in the ZnO SAW is not strong enough to produce an acoustic pressure that can deform the droplet. This is in contrast with the ZnO Sezawa wave, which is sufficiently strong to produce an acoustic pressure to deform the droplet and move it, as will be discussed later. This contrasts with what we observed in LiNbO₃ SAW microfluidics, where only the fundamental Rayleigh wave has sufficient force to deform and move the droplet, whereas the higher-order harmonic wave is not strong enough for these applications. This clearly indicates that for bulk and thin-film based SAW devices, the suitable surface acoustic wave modes for microfluidic application are different.

It was also observed that at a relatively low signal voltage of ~30V, the Rayleigh wave in the LiNbO₃ SAW is able to deform droplets of size 10 μ l, whereas for the ZnO SAW devices, the voltage required to perform the same function is above 40 V. The acoustic force increases with the voltage applied for both types of device, but deviates from the linear relationship at a high signal voltage, due to the temperature-induced resonant frequency shift at high input powers [37, 38]. The acoustic force produced by the Sezawa wave in the ZnO SAW device is typically less than 50 % of that of the Rayleigh wave in the LiNbO₃ devices. This is mainly attributed to the imperfect crystal quality and lower electromechanical coupling coefficient of the ZnO films. The upper limit of the signal voltage for the LiNbO₃ SAW device is 45 V, above which the LiNbO₃ device cracks along the IDTs and fails to operate, mainly because of the localized heating effect at the electrode. However, this is not the case for the ZnO SAW devices with an applied voltage up to 70 V, probably owing to the high thermal conductivity of the Si substrate and nanocrystalline structure of the ZnO layer, which may more easily accommodate the local heating and stress concentration

effects. At an extremely high signal voltage ($>60\text{V}$), a stream of tiny droplets with sizes in the range from a few femtolitres to a few picolitres are generated and ejected in the ZnO SAW devices. The direction of the mist is determined by the Rayleigh angle, $\theta = \sin^{-1}(V_L/V_s)$, where V_L/V_s is the ratio of the acoustic velocities in liquids and solids [39, 40]. The acoustic velocity in the liquid, V_L , is approximately 1500 m/s and that in the substrate, V_s , is ~ 3673 m/s. The Rayleigh angle calculated for water is about 23° , which is the same as that observed from the experiment.

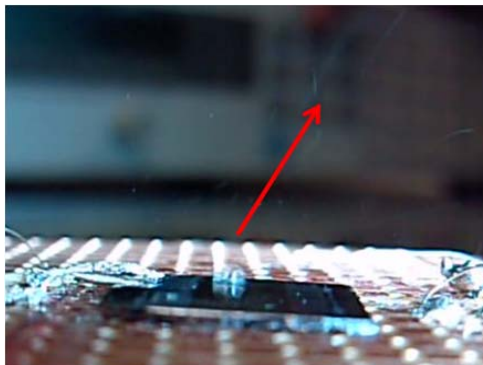


Figure 8.13 The droplet ejecting with 60V input after 2 sec

8.3.2 Droplet manipulation on ZnO SAW device

With a large input signal voltage, the water droplet on a hydrophilic surface becomes deformed from its original shape without moving forward. The large SAW pressure excites and stirs the top of the droplet, causing it to vibrate, and gradually to spread out on the surface in the wave propagation direction, as shown in Fig.8.14(b), but the liquid droplet still remains at the original position, due to the large surface energy of the ZnO films. With a further increase in the signal voltage to values above 50 V for a duration of more than 10 sec, the droplet boils (bubbles form) and evaporates as shown in Fig. 8.14(c). This is because high acoustic energy is coupled into the liquid, which significantly raises the temperature.

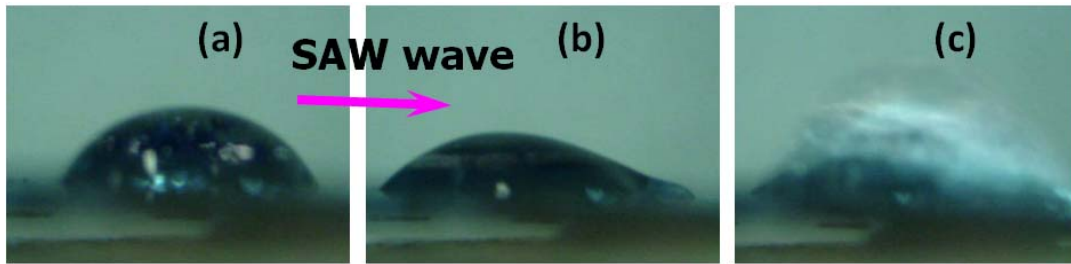


Figure 8.14 Liquid droplet behaviour on a ZnO SAW, (a) an original droplet without applying an acoustic wave; (b) spreading of a droplet by a wave and (c) bubble formation or evaporation of a droplet after applying an acoustic wave with a certain signal voltage

To manipulate the droplet on a channel-less surface freely, the surface of the ZnO SAW devices must be modified to be hydrophobic to reduce the surface energy. After the ZnO surface was modified by the OTS following the same details as discussed above for LiNbO₃ substrates, the contact angle of the water droplet on a ZnO/Si substrate increases from $\sim 70^\circ$ to $\sim 110^\circ$, resulting in a reduction of the acoustic force by almost an order of magnitude, from well in excess of 1.5 mN to the order of $\sim 400 \mu\text{N}$ which corresponds to the force required to eject the droplet from the surface. To move the droplet forward, the force required is much smaller than this. It has already been shown in Fig. 8.12 that the acoustic force that can be generated using the SAW devices in this study is $\sim 100 \mu\text{N}$ for a $10 \mu\text{l}$ droplet which should be sufficient for droplet movement. Figure 8.15 shows photos of a $1 \mu\text{l}$ droplet before and after OTS surface treatment.

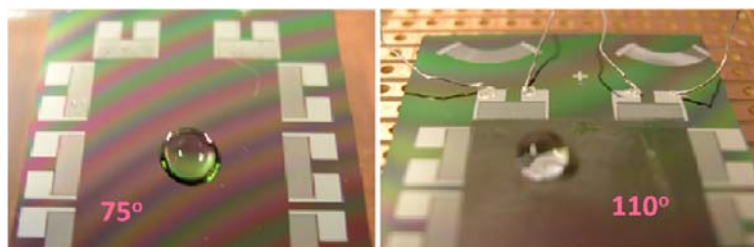


Figure 8.15 Photo of a droplet on the bare ZnO surface and the OTS treated ZnO surface

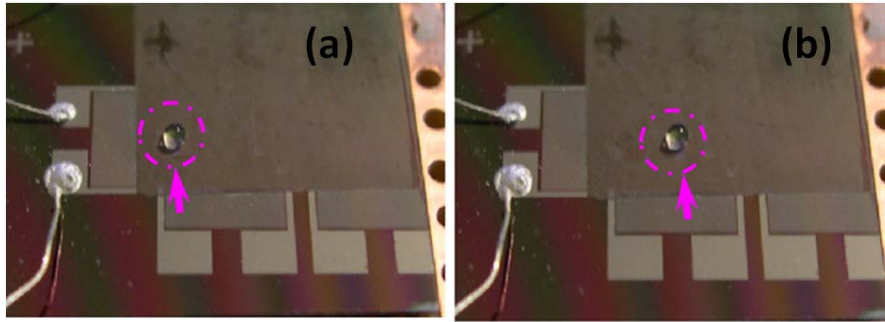


Figure 8.16 Photos of a $1\mu\text{l}$ droplet movement on an OTS-treated ZnO SAW device before (a) and after (b) being driven by an RF signal at the Sezawa wave frequency 178.7MHz , $N=60$, $\lambda=32\mu\text{m}$

Figure 8.16 shows the droplet movement by the Sezawa mode at 50V. After the RF voltage is applied, the droplet travels along the direction of the SAW propagation. Figure 8.17 shows the dependence of droplet moving speed as a function of RF signal voltage. The droplet moving speed shows an almost a linear relationship with the signal voltage tested. A small droplet driven by the acoustic wave has a higher speed than a large one, as the surface force required is smaller for a smaller droplet. The droplet motion speed for a $1\mu\text{l}$ droplet is $\sim 0.7\text{ cm/s}$, about half the speed of that produced by the Rayleigh wave in a LiNbO_3 SAW. However, this speed is higher than those of most micropumps and quite sufficient for microfluidic applications.

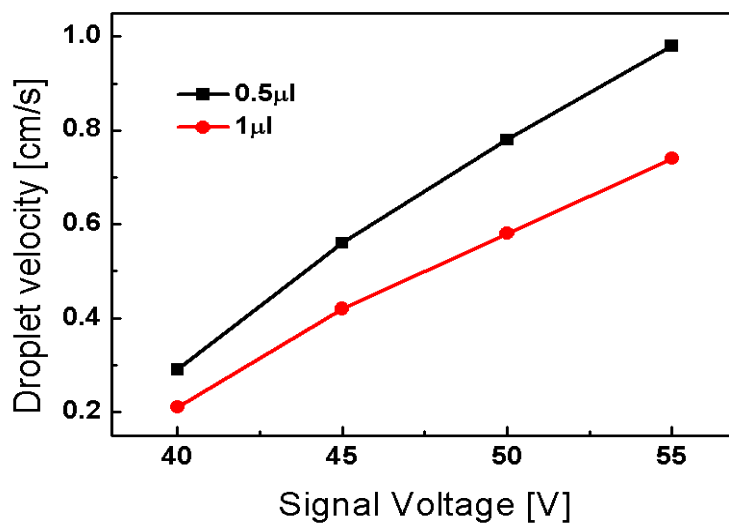


Figure 8.17 Sezawa-wave-driven droplet velocity as a function of applied voltage on the SAW for a $5.5\mu\text{m}$ ZnO SAW device

The exact mechanism to move a droplet by surface acoustic force is not clear yet; it is possibly the combination of the following two mechanisms. Under such a strong acoustic force, the droplet deforms with an increased leading angle. The restoration force of the droplet on a hydrophobic surface makes the trailing angle return to its original value which reduces the contact area, while the conservation of the work of adhesion of the droplet makes the leading angle decrease by expanding the droplet area a little in front, hence moving the droplet forward a little. By applying a “continuous” RF wave, the moving process continues in such a fast way, that the droplet is moved forward continuously. This moving process is similar to electrowetting, but in a reverse order, i.e. the droplet moves in the increased contact angle direction under the acoustic force. The other possible mechanism is that under an RF wave, the deformed droplet vibrates, and may expand a little in the forward direction owing to acoustic force, hence moving the droplet forward.

8.3.3 Surface heating and pulsed RF input on ZnO/Si substrates

Figure 8.18 shows the temperature variation on the ZnO film surface (5 mm away from the IDT), measured as a function of duration and voltage of an RF signal. It is apparent that the surface temperature of the ZnO SAWs increases with an increase in the voltage and duration of the RF signal. The maximum temperature reaches $\sim 140^{\circ}\text{C}$ for the highest signal voltage of 60 V. Hence the previous observation of bubble formation and evaporation of the water droplets during ZnO SAW microfluidic studies can be attributed to the acoustic heating effect. It should be pointed out that the temperature was measured without any water droplet on the device surface, and the temperature readings could be lower when the water droplet is present (at least lower than the boiling point).

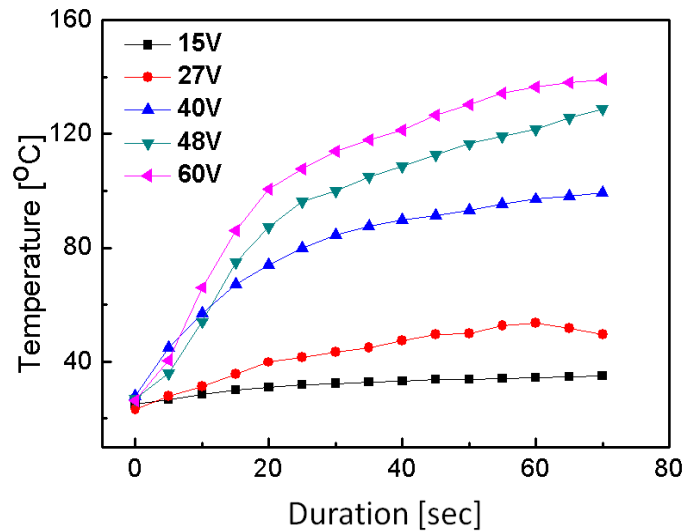


Figure 8.18 Temperature change as a function of time with RF signal voltage as a parameter. The temperature rises rapidly during the initial 20sec, and then increases slowly thereafter

The acoustic heating can be significantly reduced by using a pulsed RF signal. The surface temperature of the device was found to remain constant at room temperature with a pulse width up to 200 msec, owing to heat dissipation during the off period of the pulsed RF signal. A slight increase in temperature up to ~ 40 °C was observed when the pulse width increased to 600 ms. A pulsed RF signal also has the advantage of inducing effective mixing because of the non-regular streaming patterns, as well as precise control of droplet motion, as discussed above.

For practical applications, a pulsed RF signal is normally used to control the droplet motion with precise control of the position and moving distance. A pulsed RF signal is also able to suppress the acoustic heat. Figure 8.19 shows the dependence of the moving distance of a droplet on the number of pulses. The RF signal voltage is 40 V, the pulse width is 100 ms, and the droplet's volume is $0.5 \mu\text{l}$. The distance moved increases linearly with the number of pulses applied. The droplet moves forward when the pulse signal is on, and rests when the pulse signal is off. The average distance moved per pulse (35 V) is $\sim 72 \mu\text{m}/\text{pulse}$. It should be pointed out that the distance moved per pulse by the acoustic wave is also strongly dependent on the

signal voltage and the droplet size.

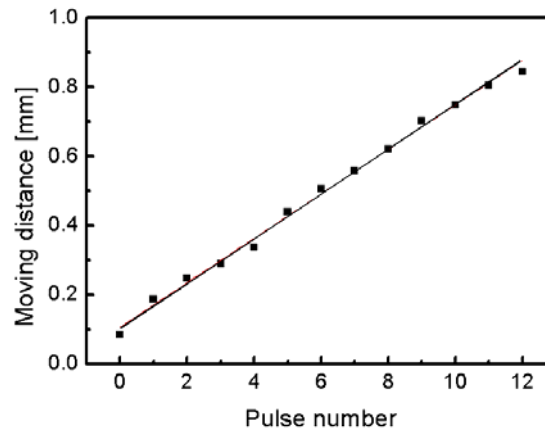


Figure 8.19 Droplet moving distance as a function of pulse number at a RF signal of 35 V. The line is a linear fit, showing a moving distance of $\sim 72\mu\text{m}$ per pulse on $5.5\mu\text{m}$ ZnO SAW with a pulse width of 100msec

Figure 8.12 showed the acoustic force difference between SAWs from LiNbO₃ and ZnO at a similar voltage, ~ 35 V, and the force at 30 V produced by LiNbO₃ is much larger than that by the ZnO SAW at 35 V, indicating that the LiNbO₃ has a much higher pumping efficiency than the ZnO.

8.4 Conclusions

- To manipulate droplets on a channel-less SAW device, the surface of the SAW device has to be modified. An OTS SAM is an efficient coating on both LiNbO₃ and ZnO SAW devices, producing a contact angle larger than 111° . A moving speed of 1.4 cm/s was obtained for a 1 μl droplet on an OTS-treated LiNbO₃ surface driven by an acoustic wave.
- Continuous acoustic waves raise the LiNbO₃ surface temperature of the SAW devices up to $\sim 80^\circ\text{C}$, a situation not suitable for microfluidic applications. The temperature rise can be minimized by using a pulsed RF signal; the surface remained at room temperature when pulse width $\leq 200\text{ms}$ was used.
- Pulsed RF signals can be used to manipulate the droplet in a digital fashion, but the voltage required to move the droplet is higher than that for the continuous wave.

- ZnO thin-film-based SAW micropumps have also been demonstrated. Results showed that SAW droplet manipulation on the ZnO device has a strong dependence on the SAW amplitude, wave mode, droplet size and surface chemical condition of the substrate.
- On the untreated ZnO surface, liquids cannot move. After OTS surface treatment, the droplet can overcome the surface energy and can be moved freely by the acoustic wave.
- Liquid droplets with a size of 0.5~1 μl were successfully pumped along the hydrophobic ZnO surface at a velocity up to $\sim 1\text{cm/s}$. This is a function of SAW power applied. A pulsed RF signal was also used to demonstrate the precision of the manipulation of the liquid droplets.
- Both LiNbO_3 and ZnO SAW devices have demonstrated their ability to manipulate droplets. The LiNbO_3 exhibits a higher pumping efficiency.

Reference

- ¹ S. Shiokawa, Y. Matsui and T. Morizumi. "Experimental study on liquid streaming by SAW". *Jpn. J. Appl. Phys.* 28 (1989) 126.
- ² J.C. Rife, M.I. Bell, J.S. Horwitz, M.N. Kabler, R.C.Y. Auyeung and W. J. Kim. "Miniature valveless ultrasonic pumps and mixers". *Sens. Actuat. A.* 86 (2000) 135.
- ³ A. Wixforth. "Acoustically driven programmable microfluidics for biological and chemical applications". *J. Assoc. Lab. Automat.* 11(6) (2006) 399.
- ⁴ S. Alzuaga, S. Ballandras, F. Bastien, W. Daniau, B. Gauthier-Manuel, J. F. Manceau, B. Cretin, P. Vairac, V. Laude, A. Khelif and R. Duhamel. "A large scale X-Y positioning and localisation system of liquid droplet using SAW on LiNbO₃". *IEEE Ultrasonic Symp.* 2 (2003) 1790.
- ⁵ M. Rotter, A.V. Kalameitsev, A.O. Govorov, W. Ruile and A. Wixforth. "Charge conveyance and nonlinear acoustoelectric phenomena for intense surface acoustic waves on a semiconductor quantum well". *Phys. Rev. Lett.* 82 (1999) 2171.
- ⁶ W.K. Tseng, J.L. Lin, W.C. Sung, S. H. Chen and G. B. Lee. "Active micro-mixers using surface acoustic waves on Y-cut 128° LiNbO₃". *J. Micromech. Microeng.* 16 (2006) 539.
- ⁷ A. Toegl, R. Kirchner, C. Gauer and A. Wixforth. "Enhancing results of microarray hybridizations through microagitation". *J. Biomolecular Techniques.* 14 (2003) 197.
- ⁸ K. Sritharan, C.J. Strobl, M.F. Schneider and A. Wixforth. "Acoustic mixing at low Reynold's numbers". *Appl. Phys. Lett.* 88 (2006) 054102.
- ⁹ W.K. Tseng and J. L. Lin. "Active micro-mixers using surface acoustic waves on Y-cut 128 degrees LiNbO₃". *J. Micromech. and Microeng.* 16 (2006) 539.
- ¹⁰ A. Sano, Y. Matsui and S. Shiokawa. "10 GHz range low-loss ladder type surface acoustic wave filter". *Jap. J. Appl. Phys.* 37 (1998) 2979.
- ¹¹ C.J. Strobl, Z.V. Guttenberg and A. Wixforth. "Nano- and pico-dispensing of fluids on planar substrates using SAW". *IEEE Trans. Ultrasonics, Ferroelectric. Freq. Contr.* 51 (2004) 1432.

-
- ¹² K. Chono, N. Shimizu, Y. Matsu, J. Kondoh and S. Shiokawa. “Development of Novel atomization system based on SAW streaming”. *Jap. J. Appl. Phys.* 43 (2004) 2987.
- ¹³ J.W. Kwon, H. Yu, Q. Zou and E.S. Kim. “Directional droplet ejection by nozzleless acoustic ejectors built on ZnO and PZT”. *J. Micromech. Microeng.* 16 (2006) 2697.
- ¹⁴ G. M. Bruinsma, H. C. van der Mei and H. J. Busscher. “Bacterial adhesion to surface hydrophilic and hydrophobic contact lenses”. *Biomater.* 22 (2001) 3217.
- ¹⁵ G. D. Yarnold. “The motion of a mercury index in a capillary tube”. *Proc. Phys. Soc. (London)* 50 (1938) 540.
- ¹⁶ D. Beyssen, L. Le Brizoual, O. Elmazria and P. Alnot. “Microfluidic device based on surface acoustic wave”. *Sens. & Actuat. B: Chemical.* 118 (2006) 380.
- ¹⁷ C. G. L. Furmidge. “Studies at phase interfaces. I. The sliding of liquid drops on solid surfaces and a theory for spray retention”. *J. Colloid Sci.* 17 (1962) 309.
- ¹⁸ I.V.Sadkovskaya and A.I.Eykhval’d. “Influence of capillary effects on precision of pressure measurement by liquid-level manometer ”. *Measurement Techniques.* 48 (2005) 237.
- ¹⁹ K. Fukagata, N. Kasagi, P. Ua-arayaporn and T. Himeno. “Numerical simulation of gas-liquid two-phase flow and convective heat transfer in a micro tube”. *J. Heat Fluid Flow.* 28 (2007) 72.
- ²⁰ A. Kawai and K. Suzuki. “Effect of low-surface-tension liquid on pattern collapse analyzed by observing dynamical meniscus”. *Jpn. J. Appl. Phys.* 45 (2006) 5429.
- ²¹ T. Ogawa¹, B. Ding, Y. Sone and S. Shiratori. “Super-hydrophobic surfaces of layer-by-layer structured film-coated electrospun nanofibrous membranes”. *Nanotechnology* 18 (2007) 165607.
- ²² P. Dubois, G. Marchand, Y. Fouillet, J. Berthier, T. Douki, F. Hassine, S. Gmouh, and M. Vaultier. “Ionic liquid droplet as e-microreactor,” *Anal. Chem.*, 78, (2006) pp. 4909.
- ²³ D. Chatterjee, B. Hetayothin, A. R. Wheeler, D. J. King and R. L.

Garrell. "Droplet-based microfluidics with nonaqueous solvents and solutions". *Lab Chip*, 6, (2006) pp. 199 .

²⁴ S. K. Cho, H. Moon and C.-J. Kim. "Creating, transporting, cutting, and merging liquid droplets by electrowetting-based actuation for digital microfluidic circuits". *J. Microelectromech. Syst.*, 12 (2003) 70.

²⁵ S. A. Kawai and K. Suzuki. "Effect of low-surface-tension liquid on pattern collapse analyzed by observing dynamical meniscus". *Jpn. J. Appl. Phys.* 45 No. 6B (2006) pp.5429.

²⁶ A. Renaudin, P. Tabourier, V. Zhang, J. C. Camart and C. Druon. "SAW nanopump for handling droplets in view of biological applications". *Sens. & Actuat. B: Chemical*. 113 (2006) 389.

²⁷ Ashley Butcher. Computer control of microdroplets using surface acoustic waves. 2008 Mphil thesis.

²⁸ U. Srinivasan, M. R. Houston, R. T. Howe and R. Maboudian. "Alkyltrichlorosilane-based self-assembled monolayer films for stiction reduction in silicon micromachines". *J. Microelectromech. Systems*. 7 (1998) 252.

²⁹ R. Maoz, R. Yam, G. Bercovic, and J. Sagiv. "Thin film: organic thin films and surfaces: directions for the nineties". Vol. 20, (Ed: A. Ulman), Academic Press San Diego, CA 1995, p.41.

³⁰ J. H. Fendler and F. C. Meldrum. "The colloid chemical approach to nanostructured materials". *Adv. Mater.* 7 (1995), 607.

³¹ E. Frydman, H. Cohen, R. Maoz and J. Sagiv. "Monolayer damage in XPS measurements as evaluated by independent methods". *Langmuir*. 13 (1997)5089.

³² J.Kondoh, N.Shimizu, Y.Matsui and S. Shiokawa. "Development of thermocycler for small liquid droplets". *IEEE Trans. Ultrasonics, Ferro, Freq. Control*. 52 (2005) 1881.

³³ R.G. Kryshtal, A.P. Kundin, A. V. Medved and V.V. Shemet. "Surface acoustic wave gas sensor of the sorption type sensitive to the thermal properties of gases". *Technical Physics Lett.* 28 (2002) 50.

- ³⁴ D. Beyssen, L. Le Brizoual, O. Emazria and P. Alnot. "Surface acoustic wave macrofluidic device". IEEE Ultrasonics Symp. 2 (2005) 1028.
- ³⁵ C.G. L. Furmidge. "Studies at phase interfaces. I. The sliding of liquid drops on solid surfaces and a theory for spray retention". J. Colloid Sci. 17 (1962) 309.
- ³⁶ G.D. Yarnold. "The motion of a mercury index in a capillary tube". Proc. Phys. Soc. 50 (1938) 540.
- ³⁷ X.Q. Bao, W. Burkhard, V. Varadan and V.K. Varadan. "SAW temperature sensor and remote reading system". IEEE Ultrasonics Symp. Proc. 14-16 (1987) 583.
- ³⁸ K. Tsubouchi and N. Mikoshiba. "Zero-Temperature-Coefficient SAW Devices On Aln epitaxial-films". IEEE Trans. Sonics and Ultrasonics, 32 (1985) 634.
- ³⁹ J. Kondoh, N. Shimizu, Y. Matsui and S. Shiokawa. "Liquid heating effects by SAW streaming on the piezoelectric substrate". IEEE Transactions on Ultrason. Ferroelectrics and Freq. Control. 52 (2005) 1881.
- ⁴⁰ T. Koga, M. Morita, H. Ishida, H. Yakabe, S. Sasaki, O. Sakata, H. Otsuka, and A. Takahara. "Dependence of the molecular aggregation state of octadecylsiloxane monolayers on preparation methods" Langmuir. 21 (2005) 905.

Chapter 9. Conclusions and Future Work

9.1 Conclusions

The SAW-based micromixer and micropump project was successful in continuing the efforts of making a practical lab-on-a-chip device with droplet movement, mixing and sensing. Digital microfluidics have the advantages of being able to precisely transport, mix, and separate.

In the first two chapters, a brief introduction of microfluidics and a review of microfluidics technologies were presented. They particularly focused on the surface acoustic wave based microfluidics, including their applications in particle concentration, droplet generation, etc.

Afterwards, the basic properties of the surface acoustic wave and the stress and strain relationship in piezoelectric solids were highlighted in Chapters 3 and 4. The wave equations on the bulk substrate and layer structure of the SAW were theoretically investigated. For both structures, there is a 90° phase difference between the horizontal and transverse displacements. In addition, the acoustic energy decays at an exponential rate into the depth beneath the surface. However, the Rayleigh waves in the layer-substrate combination have different penetration depths due to different layer thickness. Thus, the SAW velocity of a thin piezoelectric film is close to that of the substrate material. However, it decreases with the increase in piezoelectric layer thickness, and approaches that of the layer material when the surface layer thickness increases. Chapter 5 detailed the mask design, fabrication and process flow of the SAW devices. Surface acoustic wave devices with 32 and 64 μm wavelengths were fabricated on both 128° Y-cut LiNbO_3 and ZnO/Si substrates.

The subsequent chapters 6, 7 and 8 discussed the main experimental results of the Ph. D thesis. On the LiNbO_3 substrate, the third harmonic mode wave was observed in addition to the fundamental Rayleigh wave. The transmission amplitude of the Rayleigh wave is higher than that of the 3rd harmonic mode wave. Both the 1st fundamental and 3rd harmonic waves demonstrated the ability to induce streaming. However, the acoustic pressure (force) and flow velocity of the streaming induced by the Rayleigh wave were much larger than those induced by the 3rd harmonic wave at a fixed input RF power because of the difference in the transmitted signal amplitudes.

The resonant frequencies of ZnO/Si structures were found to be significantly dependent on the thickness of the ZnO film. The SAW velocity of a thin ZnO film is close to that of the Si-substrate. It decreases with increase in ZnO thickness, and approaches the SAW velocity of the ZnO when the surface layer thickness increases. In addition to the Rayleigh wave, a Sezawa mode wave with a higher resonant frequency was also observed for devices with a thick ZnO film (thickness larger than 2.8 μm). The signal amplitude of the Sezawa wave is much stronger than that of Rayleigh mode wave. Both the Rayleigh and Sezawa mode waves can be used to induce liquid streaming. The streaming by the Sezawa wave is much stronger than that induced by the Rayleigh wave due to its higher resonant frequency and larger electromechanical coupling co-efficient.

For both designs, the flow velocity was found to be directly proportional to the input signal voltage, therefore efficient mixing and high pumping speed can be achieved by using a high input signal voltage. To manipulate droplets on the channel-less SAW device, the surface of the SAW device has to be modified to be hydrophobic. An OTS SAM is an efficient coating on LiNbO_3 and ZnO/Si devices, which produces a contact angle larger than 110° . A moving speed of 1.4cm/s on LiNbO_3 has been obtained for a 1 μl droplet on an OTS treated surface driven by an acoustic wave. On the ZnO/Si

substrate, pumping velocities approaching 1 cm/s were measured. A pulsed RF signal has also been used to demonstrate precise manipulation of the liquid droplets. Furthermore a novel SAW device on ZnO island structure has been proposed, fabricated and microfluidic operation verified. This structure avoids direct contact between the piezoelectric material and microfluidic substances, and hence is promising for lab-on-a-chip applications.

In brief, the SAW micropump project was successful in continuing the efforts of making a practical lab-on-a-chip device with droplet movement and mixing. Digital microfluidics has been proven to have the distinct advantages over other types of micropumps because it enables precise transportation, mixing, and separation of the droplets.

9.2 Future work

Future work should focus on the development of a portable biosensor diagnostic device platform. A SAW is utilized on a single chip to implement fluid transport and mixing, as well as detection of target proteins or DNA. The use of a microscale device for bio-detection allows the benefits of the high surface to volume ratio at this length scale to be realized in terms of the high sensitivity and low noise.

For a microsystem biosensor device, the reagent or solution to be analysed needs to be transported to the reaction area, where they react with the biobinder. The biobinder is pre-deposited onto the detection area of the biosensor to detect a specific DNA sequence or protein. Small quantities of reagent or solution for analysis is used to increase the detection sensitivity and reduce the cost. However, fluid diffusion at a volume of nanolitres or picolitres is much slower than on the macroscale. This is certainly not suitable for real-time detection. A micro-mixer using a SAW has the advantage of mixing liquid thoroughly in a very short time- typical of the order of seconds, making real-time detection practical. Although micro-mixers have been

developed for bioMEMS applications as discrete devices [1, 2], they have not been successfully integrated with the sensor element on a single substrate. Once the reaction process is completed, the sensing element is considered to be disposable, removing the hazards of cross contamination. The principle of operation of the integrated system is shown in Fig. 9.1.

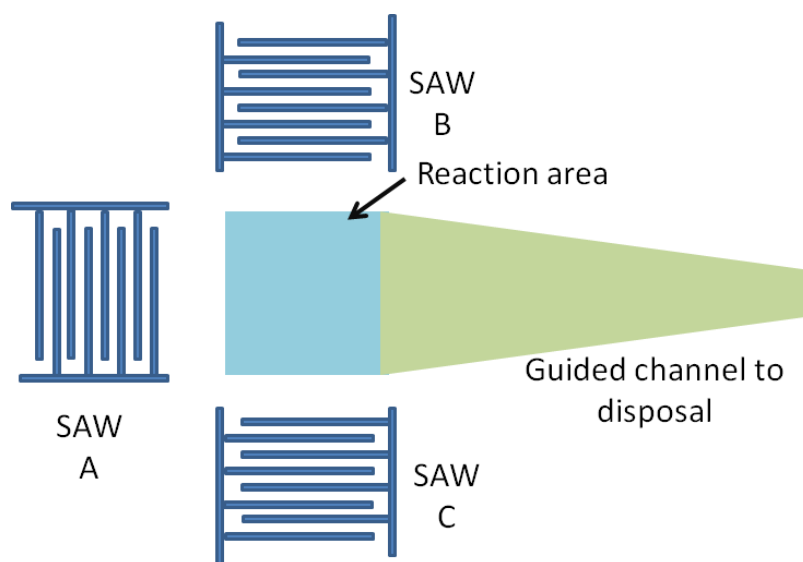


Figure 9.1 Schematic drawing of the integrated system with the guided channel to dispose waste

SAW B and C are designed to transport reagent or solution to the reaction area, where they react with the biobinders. SAW A, B and C can be simultaneously used to perform mixing functionality when the RF power applied is too small to induce liquid transport. The mixing process accelerates the reaction and reduces the binding reaction time, leading to a fast detection. Once the reaction process is completed, SAW A will generate a series of SAWs to drive the unwanted liquid waste away for disposal, leaving the surface of the reaction area in a dry state. SAW B and C now become biosensors to detect bio-substrates.

Reference

- ¹ D. S. Kim, I. H. Lee, T. H. Kwan, and D. W. Cho. "A barrier embedded Kenics. Micromixer". *J. Micromech. MicroEng.* 14 (2004) 1294.
- ² D. Lastochkin, R. Zhou, P. Wang, Y. Ben, and H. Chang. "Electrokinetic micropump and micromixer design based on ac faradaic polarization". *J. Appl. Phys.* 96 (2004) 1730.